LATENT AND THERMAL ENERGY STORAGE ENHANCEMENT OF SILVER NANOWIRES-NITRATE MOLTEN SALT FOR CONCENTRATED SOLAR POWER

BY

JADVY ROSELGE KOUKA

A thesis submitted in partial fulfilment of the requirements for the degree of Magister Scientiae in the Department of Physics and Astronomy, University of the Western Cape.

Supervisor: Prof. Malik Maaza

NANOSCIENCES AFRICAN NETWORK, MRD, ITHEMBA LABS-NRF

UNESCO UNISA-ITLABS-NRF AFRICA CHAIR IN NANOSCIENCES & NANOTECHNOLOGY, UNISA

Co-Supervisor: Dr. Sylvain Halindintwali

Department of Physics & Astronomy, University of the Western Cape

November 2020

DEDICATION

This thesis is dedicated to my parents: Jean Pierre Kouka and Banzouzi Leonie Edwige

KEYWORDS

Phase Change Material (PCM)

Molten salt of ($NaNO_3$ and KNO_3)

Concentrated Solar Power (CSP)

Nanosalt

Silver nanowires

Polyvinylpyrrolidone (PVP), polyol process

Specific heat capacity

Latent heat of fusion

Temporal evolution study

Thermal conductivity behaviour

ABSTRACT

Phase change material (PCM) through latent heat of molten salt, is a convincing way for thermal energy storage in CSP applications due to its high volume density. Molten salt, with (60% $NaNO_3$ and 40% KNO_3) has been used extensively for energy storage however; the low thermal conductivity and specific heat have limited its large implementation in solar applications. For that, molten salt with the additive of silver nanowires (AgNWs) was synthesized and characterized. This research project aims to investigate the thermophysical properties enhancement of nanosalt (Mixture of molten salt and silver nanowires). The results obtained showed that by simply adjusting the temperature, Silver nanowires with high aspect ratio have been synthesized through the enhanced PVP polyol process method. SEM results revealed a network of silver nanowires and TEM results confirmed the presence of silver nanowires with an average diameter of 129 nm and 16 μm in length. On the other hand, DSC and TGA were used to investigate the thermal behaviour of the nanosalt and molten salt. The results revealed the melting point of both salt mixture and nanosalt were around 221 °C with the latent heat of fusion around 109.88 J/g for the salt mixture. Adding silver nanowires at different percentages of 1.0, 2.0, and 3.0 wt% to the salt mixture showed an improvement in latent heat of fusion respectively of 19%, 11%, and 08%. Furthermore, specific heat capacity studies showed an average value of 1.49/g.°C for the salt mixture and that the addition of 1.0 wt%, 2.0 wt%, and 3.0 wt% silver nanowires (AgNWs) to the molten salt displayed the greatest results with an improvement of 11.41%, 10.74% and 9.39% in specific heat capacity respectively. Thermal decomposition investigation revealed the stability up to 600 °C of the salt. SEM examination of both salt mixture and nanosalt revealed that in the case of nanosalt, silver nanowires strongly changed the crystallization system suggesting a harder arrangement. Finally, the temporal evolution study of the sample to predict the behaviour of the thermal conductivity showed that the sample with 1.0 wt% additive of silver nanowires conducted heat more rapidly and the same result was observed with the specific heat capacity and heat of fusion suggesting that 1.0 wt% was more effective and the enhancement in the specific heat capacity was associated to the high specific surface area of nanowires.

DECLARATION

I declare that 'Latent and thermal energy storage enhancement of silver nanowires-nitrate molten salts for concentrated solar power' is my work, that has not been submitted for any degree or examination in any other university, and that all the sources I have used or quoted have been indicated and acknowledged by complete references

Full name: Jadvy Roselge Kouka Date: November 2020

Signed:_____

Acknowledgments

My sincere thanks are first addressed to Professor Malik Maaza, who gave me the honor to undertake this research project. I want to express my gratitude to him and my deep respect. His insights, helpful advice, instructions, and continuous support did contribute to producing this dissertation.

My deepest thanks are also directed to the Physics department and Astronomy at UWC (the University of the Western Cape for the opportunity to conduct this Master project through the Manus/Matsci program and particularly to Dr. Sylvain Halindintwali for his encouragement, insights, support, guidance and also his help at any time that I was in need.

I also express my incredible gratitude and thanks to both heads of department UWC (Physics and Astronomy) and Ithemba Labs (MRD) Prof. Christopher Arendse and Dr. Mlungisi Nkosi respectively for their support and encouragement towards me.

My gratitude also goes to UNESCO UNISA Africa Chair in Nanosciences & Nanotechnology (U2ACN2) for the financial support.

To Latife Sephora Ngoye, I also express my highest gratitude for all the support through the entire work, for always been there since day 1 to encourage and push me during this project.

To my colleagues and friends, Floyd Mabiala, Boitumelo Mabakachaba, Jespere Ondze, Ninon Etsasse, Prince Mbaki, Makhangela Mbambo, Adama Fall, Touria Khamliche, Moussa Bakayoko and everyone at MRD thank you for the incredible time spent together, I couldn't imagine that Ithemba labs could be such a vibrant and rich place where I learned a lot from each of you and thank you for the support and encouragement even when I could feel like dropping everything but you were there to say a word of encouragement.

I also express my gratitude to Dr. Juliet Sackey, for always being helpful when I approach her.

My thanks are also expressed to Ithemba Labs particularly MRD to conduct this research project where I could get any assistance from the Post-doc, an incredible and

tremendous environment, rich of free knowledge and also NRF(National research foundation) for funding and supporting me throughout the entire project.

My final thanks are deeply expressed to my Father, Jean Pierre, for being my model and source of inspiration throughout your education and the hard work you taught me, to Leonie Edwige, my Mother, thanks for the support, motivation, and encouragement you have shown me during good and difficult moments, and to my sisters, Victoire, Lorraine, Merry and Brothers Emmanuel, Jean Bonheur, thanks for your support and always believing in me.

Table of Contents

List of Tables

List of Figures

Abbreviations

Cp: Specific Heat Capacity

SHS:Sensible heat storage

CSP: Concentrated Solar Power

DSC: Differential Scanning Calorimeter

HTF: Heat Transfer Fluid

KNO_3: Potassium Nitrate

$NaNO_3$: Sodium Nitrate

Solar Salt Eutectic Binary Mix (60 wt% $NaNO_3$ & 40 wt% KNO_3)

SEM: Scanning Electron Microscope/Microscopy

TES: Thermal Energy Storage

TGA: Thermo-gravimetric Analysis

PCM: Phase Change Material

LHS: Latent Heat Storage

AgNWs: Silver nanowires

Nanosalt: (60 wt% $NaNO_3$ & 40 wt% KNO_3 + AgNWs)

CHAPTER ONE

INTRODUCTION

1.1 Introduction to renewable energy

Today, about 89% of global electricity consumption is supplied from fossil and nuclear according to the **BP Statistical Review of World Energy 2019 68th edition report**. With the announced depletion of fossil fuel reserves, their significant environmental effects, and the increase in energy consumption in developing countries, especially after the globalization of trade and commerce between states, it is necessary to find a suitable alternative and to plan a transition to other energy sources that provide minimal environmental impact and are available in sufficient quantity to meet the energy demand in future. The use of clean energy appears to be a suitable solution to this problem; it is becoming urgent to accelerate its implementation to reach significant capacity while providing it with adequate systems to ensure the reliability of supplies in quantity and quality.

Renewable energies underwent the first phase of development during the 1973 and 1978 oil shocks (Lauber, 2015), then a period of decline after the 1986 counter-shock, before recovering in 1998 following the signing of the Kyoto protocol, a protocol that notably provides for a 5% reduction in greenhouse gas emission (Zhao and Zhao, 2019). Clean energy comprises: wind power, solar (thermal, concentrated, and photovoltaic); hydraulic power, geothermal, and biomass play a huge and significant role in our energy supply (Sarbu and Sebarchievici, 2018). Solar energy including thermal, concentrated, and photovoltaic is becoming a promising new generation source of renewable energy. Also, many of the renewable energy sources above are variable, irregular, and not consistent for supply. The objective is to create systems that can store a large amount of energy and be used when necessary (Ibrahim, Ilinca, and Perron, 2008). Energy can be stored in different ways, including electrochemical, mechanical, electrical, and thermal (Molina, 2017; Nadeem *et al.*, 2019)**.** Therefore, thermal energy storage has been growing rapidly and receiving considerable attention.

Thermal energy storage (TES) is a way of stocking thermal energy by cooling or heating processes to be used later on for different power generation and other applications (Alva *et al.*, 2017; Sarbu and Sebarchievici, 2018). In combination with concentrated solar power

(CSP), thermal energy storage (TES) is particularly becoming important to store thermal energy, where solar heat can be stored when sunlight is not available. For that, new materials with enhanced thermo-physical properties are selected and characterized to be used in CSP systems. Thermal energy storage (TES) is essential to make CSP reliable and competitive with fossil fuel-based electricity generators (CSP Alliance, 2014). CSP electricity should meet the demand required at night as well at peak times.

1.2 **Concentrated solar power (CSP)**

A substantial amount of energy is supplied from the sun, by 2020, the worldwide installed capacity for solar thermal for concentrated solar power (CSP) plants will triple from 4 to 12GW (Pitz-Paal *et al.*, 2013). Also known as thermal solar power, concentrated solar power (CSP) utilizes the focused sunlight on a solar absorber to generate the heat which is transferred by nanofluids or a heat transfer fluid. The solar heat is then converted into very heat steam to power conventional steam turbines for electricity generation whenever needed as seen in figure 1 below (Islam, Bhuiyan and Ullah, 2017). Different types of CSP technologies will be discussed below.

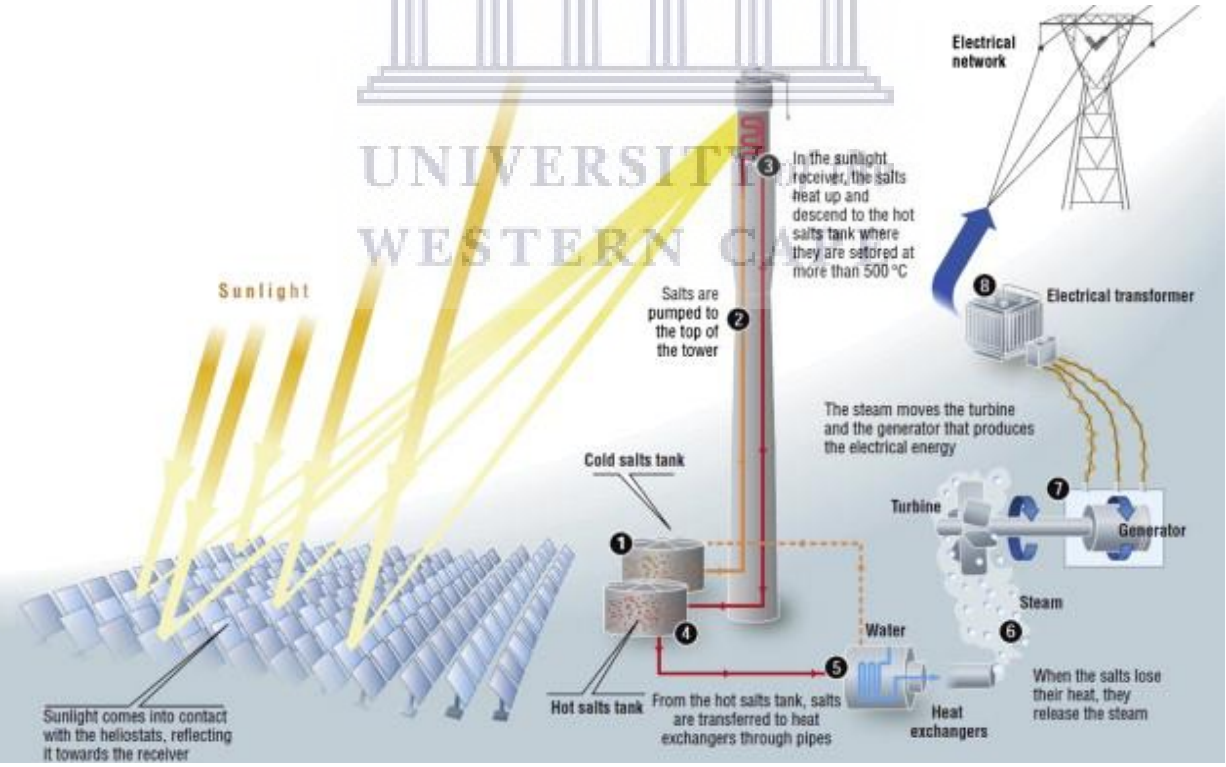

Figure1.1. Schematic diagram of a steam cycle power plant with a tower technology and thermal energy storage adapted from (Roeb *et al.*, 2013).

1.3 Brief description of CSP technologies

a) Parabolic trough

A parabolic trough is the most advanced deployed technology compared to other CSP systems (Lovegrove and Csiro, 2012). In this system, parabolic reflectors are used to concentrate sun rays on a receiver found in the optical focal line of the collector. Solar collectors are used to tracking permanently the daily movement of the sun's position on one axis. This system is composed of mirrors, receivers, and turbine technologies. The coated absorber tube which forms the receiver is integrated into an evacuated glass envelope. The absorbed solar radiation heats to almost 400°C the fluid which flows through the absorber tube. In this system, steam is produced using a heat exchanger to generate power in the turbines. The capacity of the power plant at the maximum point is 25 MW to 200 MW. By combining storage facilities, the plants will always run at a steady flow rate. The parabolic trough is good in terms of productivity and lower output costs(Implementation, 2007).

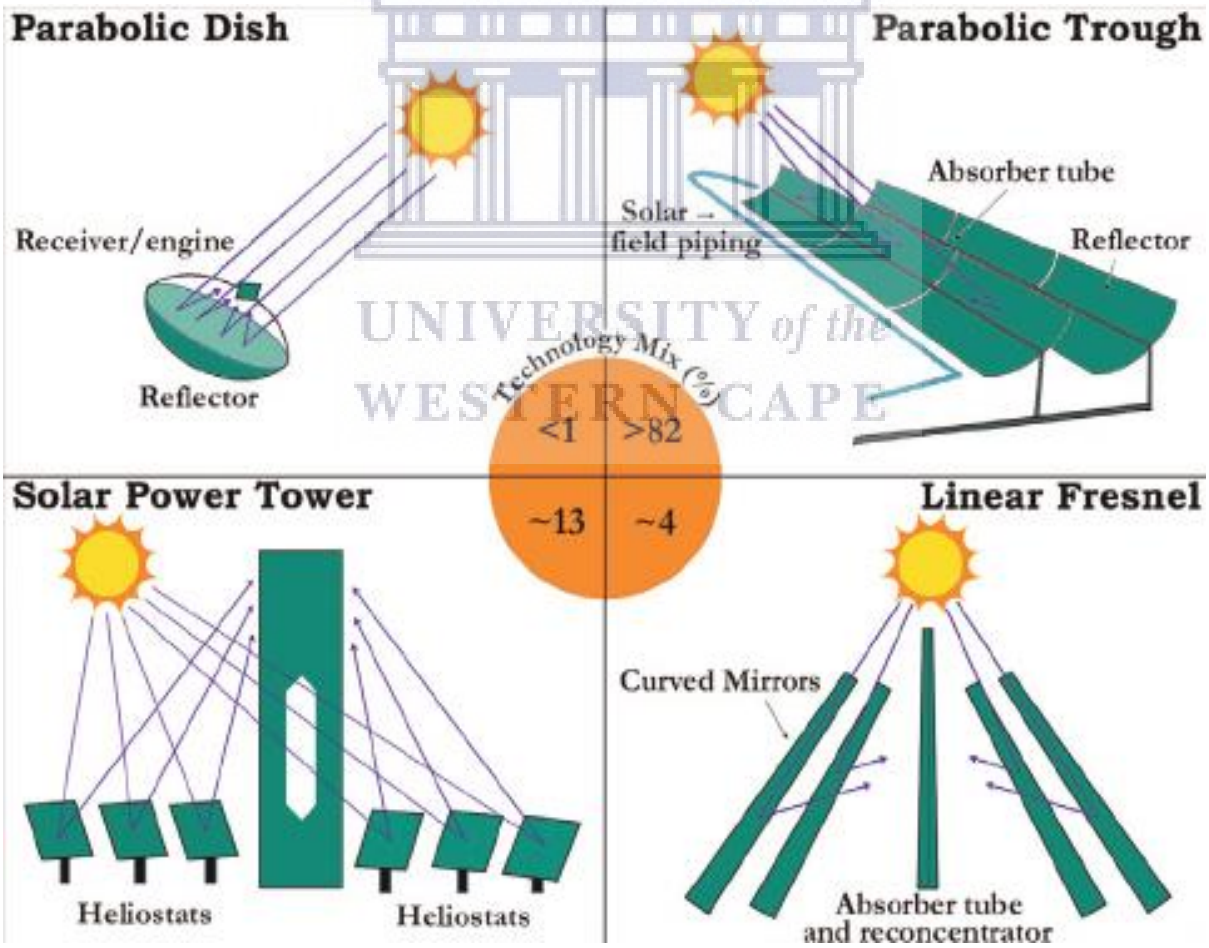

Figure 1.2.Different CSP technologies with their installed percentages adapted from (Xu *et al.*, 2016)

b) Solar tower technology

The solar tower has been a subject of study over the past 30 years in these countries, the United State of America (USA) and Spain (Omambia *et al.*, 2015). Solar central tower systems are composed of a single receiver which is enclosed by several mirrors (heliostats). The top of the tower concentrates the radiation on a receiver by using a sun's tracking system that manages the entire fleet of heliostats. The receiver is filled with a heat transfer fluid, which may be synthetic oils, water, pressurized hot air, or molten salts to capture long term thermal energy(Islam, Bhuiyan and Ullah, 2017). In contrast to other CSP systems, a high temperature is needed for the solar tower to concentrate heat. Heliostats include a tacking system of two-axis (the receiver), the steam generation system, and the storage system are the main components of the solar tower system. The number of heliostats can differ based on the thermal period of the actual receiver and the configuration of the heliostat(Implementation, 2007; Krothapalli, 2016).

c) Parabolic dish collector

A parabolic dish collector directs and focuses the sun incident solar energy into a small receiving area using mirrors. The sun rays are concentrated on a single spot that gets directed to a Stirling engine. The engine utilizes a heat exchanger to expand and transfer a fluid placed in the focus of the parabolic dish according to the **International Energy Agency (IEA) 2010 technology roadmap**.

d) Linear Fresnel reflector technology

The linear-Fresnel technology uses Fresnel's principle of lenses to reconstruct a parabolic trough reflector using plane or slightly curved mirrors. Each of these mirrors is adjustable along an axis, forming a long "line" parallel. This makes it possible to use a fixed linear receiver facilitating the direct generation of steam, eliminating the costs associated with the use of heat transfer fluid. Typical concentration factors are similar to those obtained with parabolic trough technology, molten salt is also used as thermal storage to make the system useful at night and during cloudy days(Islam, Bhuiyan and Ullah, 2017).

1.4 Motivation

Latent heat storage (LHS) has been investigated to enable large storage of energy in concentrated solar power (CSP). Its implementation in the energy production market is still limited and the most utilized TES is achieved through sensible heat storage. However,

the studies carried out displayed a potential for certain applications. Latent heat storage depends upon the average capacity to store energy after undergoing a phase transformation from solid to liquid or vice versa. In latent heat storage (LHS), phase-change materials (PCMs) are employed. PCMs have been used widely for low and medium temperature applications (Ghaib, 2017). Thermal solar systems have been highly popular as they are fairly cheap, simple to produce. (Prakash, Garg and Datta, 1985) incorporated the LHS module into the solar thermal unit. Throughout the daylight hours, the surplus heat is retained through the HTF (heat transfer fluid) in the LHS system. During periods with minimal to no radiation, the LHS module was used as the source of heat. The storage system was not reliable because the heat transfer was low between the heat storage medium and the heat transfer fluid. For that,(Xiao and Zhang, 2014) used paraffin expanded-graphite capsules as heat storage material. Through the capsules, a reliable LHS subsystem was obtained. Several other applications including buildings have been reported and all showed the potential of the use of LHS. Moreover, the latent heat of a substance is larger than the specific heat of the same substance; latent heat storage enables the storage of the same amount of heat in a smaller volume. This is a significant advantage of latent heat storage systems. Combining all the aforementioned, latent heat of molten salt could be used for solar energy storage and heat transfer fluid (HTF) at a high temperature to maintain thermal efficiency. Presently, several different types of HTFs are used in commercial CSP plants, including air, water/steam, thermal oils, organics, and molten salts(Xu *et al.*, 2016). Synthetic oils including Terminal® VP-1 or Downthern® have been used in parabolic trough CSP plants for heat transfer fluid(Heller, 2013). These oils have many disadvantages preventing them from not operating at high temperatures and limiting their use to around 400 ℃. Due to degradation, high cost, and inflammability, these oils are not efficient; other materials have to be investigated. Molten salts seem to be a key on an active direct concept for thermal energy storage and heat transfer fluid. Also called solar salt, molten salts of sodium nitrate and potassium nitrate with 60% and 40% respectively of their masses (Pfleger *et al.*, 2015) are currently used in CSP applications and other cooling and heating technologies. The performance of CSP plants with TES technology depends on how TES is incorporated into the power generation system and also on other parameters that can be summarized as nominal temperature and specific enthalpy reduction in the level (discharge and transformation side), maximum load, operational strategy, and integration into the plant (Kuravi *et al.*, 2013).

1.5 Objectives and Aims

This research project aims to investigate the phase transition (solid-liquid and liquid-solid) of the molten salt (NaNO3 and KNO3), nanosalt, and their thermophysical properties enhancement for energy storage. This will be achieved following the objectives listed below.

1. To enhance some Thermophysical properties (heat specific, thermal conductivity, melting point), silver nanowires will be added to the current mixture of molten salt ($NaNO_3$ and KNO_3). Both molten salt and silver nanowires are called nanosalt.
2. Silver nanowires will be synthesized using the Polyol technique in which an inorganic salt ($AgNO_3$) used as a precursor is reduced by a polyol (ethylene glycol) at an elevated temperature,
3. X-ray diffraction (XRD) will be used to investigate the crystalline material and the unit cell dimensions
4. Scanning electron microscopy (SEM) will be used for the morphology, EDS for the composition, Transmission electron microscopy (TEM) for the structure crystallization, and UV-Vis spectroscopy for the absorption.
5. In the final compound (nanosalt), Differential Scanning Calorimetry (DSC) and Thermal gravimetric analysis (TGA) will be used to investigate the heat specific, thermal conductivity (Temporal evolution of temperature), and the melting point.

1.6 References

Alva, G. *et al.* (2017) 'Thermal energy storage materials and systems for solar energy applications', *Renewable and Sustainable Energy Reviews*. Elsevier, 68(February 2016), pp. 693–706. DOI: 10.1016/j.rser.2016.10.021.

CSP Alliance (2014) 'The economic and reliability benefits of CSP with thermal energy storage: recent studies and research needs', *CSP Alliance Report*, pp. 1–126. DOI: 10.1017/CBO9781107415324.004.

Ghaib, K. (2017) 'Latent Heat Storage: Storage Materials, Heat Transfer, and Applications', *ChemBioEng Reviews*, 4(4), pp. 215–224. DOI: 10.1002/cben.201700007.

Heller, L. (2013) 'Literature review on heat transfer fluids and thermal energy storage systems in CSP plants', *Literature review on heat transfer fluids and thermal energy storage systems in CSP plants*.

Ibrahim, H., Ilinca, A. and Perron, J. (2008) 'Energy storage systems-Characteristics and comparisons', *Renewable and Sustainable Energy Reviews*, 12(5), pp. 1221–1250. DOI: 10.1016/j.rser.2007.01.023.

Implementation, T. O. (2007) *From Research To Implementation From Research To Implementation European Commission*. Available at: http://europa.eu.

Islam, R., Bhuiyan, A. B. M. N. and Ullah, M. W. (2017) 'An Overview of Concentrated Solar Power (CSP)Technologies and its Opportunities in Bangladesh', *ECCE 2017 - International Conference on Electrical, Computer and Communication Engineering*, (February 2017), pp. 844–849. DOI: 10.1109/ECACE.2017.7913020.

Krothapalli, A. (2016) *Handbook of Climate Change Mitigation and Adaptation*, *Handbook of Climate Change Mitigation and Adaptation*. DOI: 10.1007/978-1-4614-6431-0.

Kuravi, S. *et al.* (2013) 'Thermal energy storage technologies, and systems for concentrating solar power plants', *Progress in Energy and Combustion Science*. Elsevier Ltd, 39(4), pp. 285–319. DOI: 10.1016/j.pecs.2013.02.001.

Lauber, V. (2015) *Political Economy of Renewable Energy*. Second Edi, *International Encyclopedia of the Social & Behavioral Sciences: Second Edition*. Second Edi. Elsevier. DOI: 10.1016/B978-0-08-097086-8.91084-5.

Lovegrove, K. and Csiro, W. S. (2012) 'Introduction to concentrating solar power (CSP) technology', *Concentrating Solar Power Technology: Principles, Developments, and Applications*, pp. 3–15. DOI: 10.1016/B978-1-84569-769-3.50001-7.

Molina, M. G. (2017) 'Energy Storage and Power Electronics Technologies: A Strong Combination to Empower the Transformation to the Smart Grid', *Proceedings of the IEEE*, 105(11), pp. 2191–2219. DOI: 10.1109/JPROC.2017.2702627.

Nadeem, F. *et al.* (2019) 'Comparative review of energy storage systems, their roles, and impacts on future power systems', *IEEE Access*. IEEE, 7(c), pp. 4555–4585. DOI: 10.1109/ACCESS.2018.2888497.

Omambia, A. N. *et al.* (2015) 'Climate Change Impacts, Vulnerability, and Adaptation in East Africa (EA) and South America (SA) The East African (EA) Picture Brief Introduction of EA Region', (Decher 1994), pp. 1–40. DOI: 10.1007/978-1-4614-6431-0.

Pfleger, N. *et al.* (2015) 'Thermal energy storage - overview and specific insight into nitrate salts for sensible and latent heat storage', *Beilstein Journal of Nanotechnology*, 6(1), pp. 1487–1497. DOI: 10.3762/bjnano.6.154.

Pitz-Paal, K. *et al.* (2013) 'Solar thermal power plants - Utilising concentrated sunlight for generating energy', *BINE-Themeninfo*, II/2013, p. 20. DOI: 10.1140/epjst/e2009-01153-0.

Prakash, J., Garg, H. P. and Datta, G. (1985) 'A solar water heater with a built-in latent heat storage', *Energy Conversion and Management*, 25(1), pp. 51–56. DOI: 10.1016/0196-8904(85)90069-X.

Roeb, M. *et al.* (2013) *Solar Thermal Water Splitting*, *Renewable Hydrogen Technologies: Production, Purification, Storage, Applications and Safety*. Elsevier. DOI: 10.1016/B978-0-444-56352-1.00004-0.

Sarbu, I. and Sebarchievici, C. (2018) 'A comprehensive review of thermal energy storage', *Sustainability (Switzerland)*, 10(1). DOI: 10.3390/su10010191.

Xiao, X. and Zhang, P. (2014) 'Experimental investigation on heat storage/retrieval characteristics of a latent heat storage system', *Heat Transfer Engineering*, 35(11–12), pp. 1084–1097. DOI: 10.1080/01457632.2013.863127.

Xu, X. *et al.* (2016) 'Prospects and problems of concentrating solar power technologies for

power generation in the desert regions', *Renewable, and Sustainable Energy Reviews*. Elsevier, 53, pp. 1106–1131. DOI: 10.1016/j.rser.2015.09.015.

Zhao, H., and Zhao, H. (2019) *Energy Crisis: "Natural Disaster" and "Man-Made Calamity"*, *The Economics and Politics of China's Energy Security Transition*. DOI: 10.1016/B978-0-12-815152-5.00004-X.

CHAPTER TWO

LITERATURE REVIEW

For chapter two, a current study of thermal energy storage, storage materials, previous work on latent heat storage material and, specific heat, thermal conductivity enhancement techniques, are discussed.

2.1 THERMAL ENERGY STORAGE

Thermal energy storage (TES) is widely achieved by different techniques, relying upon a particular technology, TES enables surplus thermal energy to be kept and utilized later on. The use of TES technology shows how important it is becoming for electricity to be stored when integrated into concentrating solar power (CSP) plants where solar heat is stored for the generation of electricity when sunlight goes down (Pfleger *et al.*, 2015). In that regards, (Zalba *et al.*, 2003; Fernandes *et al.*, 2012) describe in the literature different characteristics of the thermal energy storage medium which are:

(i) The storage material with great energy density

(ii) Reliable heat transfer fluid with the storage medium.

(iii) A stable mechanical and chemical transformation during different charging and discharging cycles in the storage material.

(iv) Low heat losses.

(v) Appropriate nominal temperature.

(vi) Low cost

2.2 Classification of Thermal Energy Storage

Sensible heat, latent heat, and chemical heat storage are the three (3) classes of Thermal energy storage

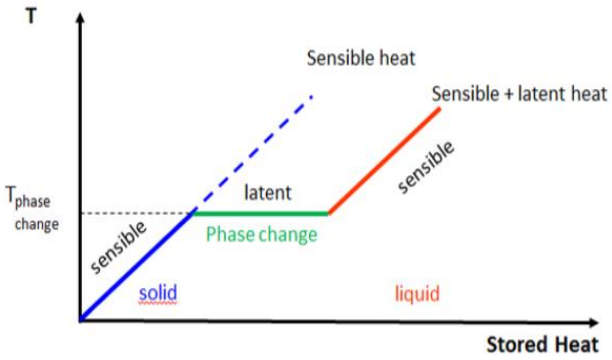

Figure 2.1: Latent and sensible heat diagram of solid-liquid phase change adapted from **(Chieruzzi and Adio, 2016)**

a) Sensible Heat Storage

A change in temperature of the storage medium enables the storage of thermal energy in sensible heat **(Liu *et al.*, 2016)**. Depending on the storage medium (m), the specific heat capacity (Cp), and the temperature change, the quantity of energy stored is determined by those three (3) elements. The temperature change dt is given by equation (2.1) (Cárdenas and León, 2013).

$$Q=\int_{t_i}^{tf} mC_P\, dt=mc_p\left(t_f - t_i\right) \quad (2.1)$$

Where Q is the quantity of heat stored in Joules, t_f and t_i represent respectively the final and initial Temperatures in ℃, the quantity m in kg and C_P in nK/kg. Sensible heat storage (SHS) can be categorized on different storage material considered as the liquid medium which includes oil, molten salt, water or in the solid form including (Rocks, and metals**)** (Sarbu and Sebarchievici, 2018). **Table 2.1** gives an overview of the most used SHS material with their properties (Ayyappan, Mayilsamy, and Sreenarayanan, 2016; Sarbu and Sebarchievici, 2018). The best cheaper SHS liquid ready for use seems to be water displaying a high specific heat. However, oils, molten salts, and liquid metals are used above 100℃ (Sarbu and Sebarchievici, 2018). Also, the temperature does not affect the change of phase during the storage transformation in (SHS). Sensible heat storage in a material depends strongly on its heat capacity, ρC_p, which determines the energy density and the thermal diffusivity k/ ρC_p, which controls the rate at which that heat can be released and extracted (Fernandes *et al.*, 2012; Kuravi *et al.*, 2013). **Table 2.2** Reveals different characteristics of the most commonly used solid-state thermal storage material, such as sand-rock minerals, concrete, fire bricks, and ferroalloy materials. These materials have an operating temperature varying from 200 to 1200℃ and have excellent thermal conductivities: 1.0 w/ (m.k) - 7.0 w/ (m.k) for sand-rock minerals, concrete, and fire bricks; 37.0 w/ (m.k) - 40.0 w/ (m.k) for ferroalloy materials. All materials in table 2 are low- cost, ranging from 0.05US$/kg to 5.00US$/kg. The low heat specific from 0.26 to 1.3 kJ/ (kJ. ℃) is the only problem that can make the storage unit unrealistically large (Ayyappan, Mayilsamy, and Sreenarayanan, 2016).

Table 2.1. List of selected solid-liquid materials for sensible heat storage (Ayyappan, Mayilsamy, and Sreenarayanan, 2016)

Medium	Fluid Type	Temperature Range (DC)	Density (kg/m^3)	Specific Heat (J/(kg·K))
Sand	-	20	1555	800
Rock	-	20	2560	879
Brick	-	20	1600	840
Concrete	-	20	2240	880
Granite	-	20	2640	820
Aluminium	-	20	2707	896
Cast iron	-	20	7900	837

Water	-	0-100	1000	4190
Calorie HT-43	Oil	12-260	857	2200
Engine oil	Oil	≤160	888	1880
Ethanol	Organic liquid	≤78	790	2400
Propane	Organic liquid	≤97	800	2500
Butane	Organic liquid	≤118	809	2400
Isotunaol	Organic liquid	≤100	808	3000
Isopentanol	Organic liquid	≤148	831	2200
Octane	Organic liquid	≤126	704	2400

Table 2.2. Solid-state sensible heat storage materials (Tian and Zhao, 2013)

Storage Materials	Working Temperature (℃)	Density (kg/m^3)	Thermal Conductivity (w/ (m.k))	Specific Heat (kJ/ (kg.℃)
Sand-rock minerals	200– 300	1700	1.0	1.30
Reinforced concrete	200–400	2200	1.5	0.85
Cast iron	200–400	7200	37.0	0.56
NaCl	200– 500	2160	7.0	0.85
Cast steel	200– 700	7800	40.0	0.60
Silica fire bricks	200– 700	1820	1.5	1.00
Magnesia fire bricks	200– 1200	3000	5.0	1.15

b) Latent Heat Storage

Latent heat storage (LHS) occurs when a material's temperature is raised until it undergoes a phase change, either from solid to liquid or from liquid to gas or during solid-solid transitions (Cárdenas and León, 2013). Latent heat storage is a nearly isothermal process that can provide significantly enhanced storage quantities when compared to SHS of the same temperature range (Kuravi *et al.*, 2013). During phase transformation, a large amount of heat is absorbed or released depending on the change of temperature. Phase change materials PCM absorb or release heat energy through latent heat of fusion during the melting/solidification or gasification/liquefaction processes. In latent heat storage, thermal energy stored can be expressed by the following equation

$$Q=\int_{ti}^{tm} mCpdt + m.L + \int_{tm}^{tf} mCpdt = mC_{sp}(t_m - t_i) + m.L + mC_{lp}(t_f - t_m) \quad (2.2)$$

With m representing the mass in (kg) and L, latent heat of fusion in (KJ/kg), Q amount of heat in (kJ), Csp specific heat capacity in solid-state (kJ/ kg℃), C_{lp} specific heat capacity in the liquid state (kJ/ kg℃), t_m, t_i, and t_f are respectively melting, initial and final temperatures in (℃). Mostly, the liquid-gas phase transition requires higher heat of transformation than in solid-liquid transitions. Implementing liquid-gas as a thermal storage is difficult because it

involves large volumes or a high pressure which makes the system complex and not practical. Therefore, the solid-liquid phase is the only phase change used for thermal storage. Solid-Solid phase changes are usually too slow and have a very low value of latent heat of phase change (Liu *et al.*, 2016; Zhang *et al.*, 2016; Alva *et al.*, 2017). Although phase change materials (PCMs) should have a better potential for energy storage compare to SHS. A good latent heat energy storage system should include these three elements (Sharma *et al.*, 2009):

(i) Good Phase Change Material with a reliable melting point in the desired temperature range,
(ii) A suitable heat exchange surface
(iii) A suitable container compatible with the PCM

c) Thermochemical Heat Storage

Different from latent and sensible heat storages, thermochemical TES refers to a reversible reaction absorbing and releasing heat.

$$\mathbf{A + \Delta Hr \Longleftrightarrow B + C} \qquad (2.3)$$

Thermochemical heat storage is controlled by two chemical reactions for the heat to be stored or released following respectively the endothermic and the exothermic reaction. The heat stored from this reaction refers to the reaction enthalpy. The use of thermal energy enables the break of a chemical reactant (A), into products (B) and (C) during the charging and endothermic reaction. The final products (B and C) are combined to form the previous reactant (A) during the releasing process. The stored heat corresponds to the amount of storage material (m), the endothermic heat of the reaction (ΔHr), and the conversion (α), given by:

$$Q = m\alpha\Delta H_r, \text{ with } \alpha \leq 1 \qquad (2.4)$$

The above reaction releases heat and is an exothermic reaction. Ambient temperature or a working temperature can be used to store the products of the two reactions (Liu *et al.*, 2016; Zhang *et al.*, 2016).

2.3 PHASE CHANGE MATERIAL AND SELECTION

Phase Change Material (PCM) is a capability of a given material with a high heat of fusion to change a physical state within a restricted temperature range allowing the material to store or release a large amount of heat. Extensive work has been done on different Phase Change

Material and their different characteristics. (Zalba *et al.*, 2003; Sharma *et al.*, 2009; Kuravi *et al.*, 2013)**,** (Cáceres *et al.*, 2017) and, other authors have summarised that to be utilized in thermal energy storage, PCMs should possess desirable and selected properties which follow:

a) Thermal properties

- Suitable phase-transition temperature.
- High latent heat of transition.
- Good heat transfer.

High latent heat should be applied, to reduce the physical size of the heat stored on a volumetric basis. During the charging and discharging of the storage process, high thermal conductivity would be helpful.

b) Physical Properties

- Favourable Phase equilibrium
- High density
- Small volume change
- **Low vapour pressure**

Phase stability during freezing melting would help towards setting heat storage and high density is desirable to allow a smaller size of the storage container. Small volume changes on phase transformation and small vapour pressure at operating temperatures to reduce the containment problem.

c) Kinetic properties

- No Super cooling
- Sufficient crystallization rate

Super cooling has been a troublesome aspect of PCM development, particularly for salt hydrates. Super cooling of more than a few degrees will interfere with proper heat extraction from the store, and 5–10℃ super cooling can prevent it entirely.

d) Chemical properties

- Long-term chemical stability
- Compatibility with materials of construction
- No toxicity.

PCM can suffer from degradation by loss of water of hydration, chemical decomposition, or incompatibility with materials of construction. PCMs should be non-toxic, non-flammable, and non-explosive for safety.

e) Economics

- Abundant.
- Available
- Cost-effective

Low cost and large-scale availability of the phase change materials is also very important

2.4 Classification of Phase Change Materials (PCMs)

Phase Change Materials (PCMs) can be classified into different groups including organic, inorganic, and eutectic. The melting and latent heat of fusion define each group of PCMs. Except for the operational melting point, however, most PCMs do not meet the necessary criteria for an appropriate storage media. The poor physical properties can be balanced by proper system design since there is no material with all the necessary features. Metallic fins may, for example, be used for enhancing the thermal conductivity of PCM and the use of a nucleating agent or cold finger to prevent super cooling and incongruent melting can be inhibited by the use of a PCM of suitable thickness. The description of each sub-group influencing the design of the latent thermal storage systems utilizing PCMs for their very specific thermal-and chemical actions is described below (Tyagi and Buddhi, 2007; Sharma *et al.*, 2009; Baetens, Jelle and Gustavsen, 2010)

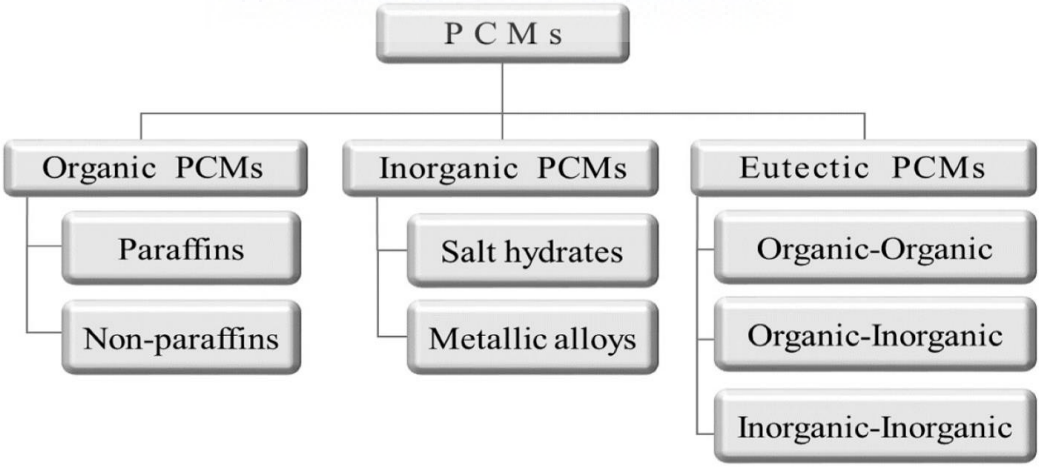

Figure 2.2: Scheme of phase-change materials (PCM) classification adapted from (Yang *et al.*, 2019)

a) **Organic Phase Change Materials**

Paraffins and non-paraffins materials are described as organic compounds. Organic materials involve congruent melting means that melt and freeze constantly without splitting the phase, thus reducing its latent heat of fusion.

- **Paraffins**

Paraffin wax is formed from a mixture consisting mostly of CH3–(CH2)–CH3n alkanes. A big amount of warmth is produced by crystallization of the (CH3)-chain. The heat of fusion and temperature increases both with the length. The temperature of alkane increases with the increasing number of carbon atoms. Because of its availability within the broad temperature, paraffin qualifies as the heat of fusion storage materials. Nonetheless, thanks to costs, only technical grade paraffin is used as PCM in heat energy storage systems. These styles of materials are safe, reliable, predictable, more cost-effective, non-corrosive, and are stabled below 500, Table 2. 3, lists the thermal properties of some technical grade paraffin, which are essential, paraffin mixtures and don't seem to be entirely refined oil. Additionally, to some favorable thermal properties sort of the desirable freezing point, good nucleation properties, they also possess unwanted properties like poor thermal conductivity, flammability. Other paraffin materials are shown in Table 2.4 with their different properties; temperature, heat of fusion, and groups. PCM is classified regarding groups as (a) group I, most promising; (b) group II, promising; and (c) group III, less promising. (Sharma *et al.*, 2009).

Table 2.3: Physical properties of some paraffin (Sharma *et al.*, 2009)

Paraffin	Freezing point/ range (8C)	Heat of fusion (kJ/kg)	Group
6106	42–44	189	I
P116	45–48	210	I
5838	48–50	189	I
6035	58–60	189	I
6403	62–64	189	I
6499	66–68	189	I

Table 2.4: Melting point and latent heat of fusion: paraffin (Sharma *et al.*, 2009)

No. of carbon atoms	Melting point (8C)	Latent heat of fusion (kJ/kg)	Group
14	5.5	228	I
15	10	205	II
16	16.7	237.1	I
17	21.7	213	II
18	28.0	244	I
19	32.0	222	II
20	36.7	246	I
21	40.2	200	II
22	44.0	249	II
23	47.5	232	II

24	50.6	255	II
25	49.4	238	II
26	56.3	256	II
27	58.8	236	II
28	61.6	253	II
29	63.4	240	II
30	65.4	251	II
31	68.0	242	II
32	69.5	170	II
33	73.9	268	II
34	75.9	269	II

- **Non-paraffins**

The greatest number of phase change materials (PCMs) is non-paraffins materials possessing very diverse properties. In comparison to paraffin, each of these compounds will have very similar characteristics. Non-paraffins materials are classified to be the most candidates of phase change storage. Many researchers have conducted extensive work in these materials, and identify numerous fatty acids, ester, alcohols, and glycols materials for energy storage. These materials present different properties which are: high heat of fusion, low thermal conductivity, toxicity, instable (Rout and Sharma, 2013). Fatty acids (CH3(CH2)2nCooH) are Renewable PCMs, which have excellent thermodynamic and kinetic properties, including latent heat of fusion, over-cooling, thermal and chemical stability, small changes in volume, and large melting point **Table 2.5 below, shows some melting point and latent heat of fusion of non-paraffins** (Sharma *et al.*, 2009). Different from paraffin, each fatty acid got different properties; their melting points and heat of fusion grow gradually as the number of carbon atoms in a fatty acid molecule rises (Cárdenas and León, 2013; Yang *et al.*, 2019). Moreover, their main disadvantages are the corrosiveness and the cost, which is 2 to 3 times higher than that of technical paraffin. Quite a several fatty acids with low melting point and latent heat storage are shown in **table 2.6** (Sharma *et al.*, 2009).

Material	Melting point (°C)	Latent heat (kJ/kg)	Group
Formic acid	7.8	247	III
Caprylic acid	16.3	149	–
Glycerin	17.9	198.7	III
D-Lactic acid	26	184	I
Methyl palmitate	29	205	II
Camphenilone	39	205	II
Dodecyl bromide	40	201	II
Caprylone	40	259	II
Phenol	41	120	III
Heptadecanone	41	201	II
1-Cyclohexylooctadecane	41	218	II
4-Heptadacanone	41	197	II
p-Joluidine	43.3	167	–
Cyanamide	44	209	II
Methyl nicotinate	45	230	II
3-Heptadecanone	48	218	II

2-Heptadecanone	48	218	II
Hydrocinnamic acid	48.0	118	–
Cetyl alcohol	49.3	141	–
α-Nepthylamine	50.0	93	–
Camphene	50	238	III
O-Nitroaniline	50.0	93	–
9-Heptadecanone	51	213	II
Thymol	51.5	115	–
Methyl behenate	52	234	II
Diphenylamine	52.9	107	–
p-Dichlorobenzene	53.1	121	–
Oxalate	54.3	178	–
Hypophosphoric acid	55	213	II
O-Xylene dichloride	55.0	121	–
β-Chloroacetic acid	56.0	147	III
Chloroacetic acid	56	130	III
Nitro naphthalene	56.7	103	–
Trimyristin	33–57	201–213	I
Heptaudecanoic acid	60.6	189	II
α-Chloroacetic acid	61.2	130	–
Bee wax	61.8	177	II
Beeswax	61.8	177	II
Glycolic acid	63.0	109	–
Glycolic acid	63	109	–
p-Bromophenol	63.5	86	–
Azobenzene	67.1	121	–
Acrylic acid	68.0	115	–
Dinto toluent (2,4)	70.0	111	–
Phenylacetic acid	76.7	102	–
Thiosinamine	77.0	140	–
Bromcamphor	77	174	–
Durene	79.3	156	–
Benzylamine	78.0	174	–
Methyl bromobenzoate	81	126	–
Alpha naphthol	96	163	–
Glutaric acid	97.5	156	–
p-Xylene dichloride	100	138.7	–
Catechol	104.3	207	III
CONTINUED			
Quinone	115	171	II
Acetanilide	118.9	222	II
Succinic anhydride	119	204	II
Benzoic acid	121.7	142.8	III
Stilbene	124	167	–
Benzamide	127.2	169.4	III

Table 2.6: Melting point and latent heat of fusion of metallics (Sharma *et al.*, 2009)

Material	Formula	Melting point (℃)	Latent heat (kJ/kg)	Group
Acetic acid	CH_3COOH	16.7	184	I
Polyethylene glycol 600	$H(OC_2H_2)_nOH$	20–25	146	I
Capric acid	$CH_3(CH_2)_8COOH$	36	152	–
Elaidic acid	C8H7C9H16COOH	47	218	I
Lauric acid	$CH_3(CH_2)_{10}COOH$	49	178	II
Pentadecanoic acid	$CH_3(CH_2)_{13}COOH$	52.5	178	–
Tristearin	(C17H35COO) C3H5	56	191	I
Myristic acid	$CH_3(CH_2)_{12}COOH$	58	199	I
Palmitic acid	$CH_3(CH_2)_{14}COOH$	55	163	I
Stearic acid	$CH_3(CH_2)_{16}COOH$	69.4	199	I
Acetamide	CH_3CONH_2	81	241	I
Methyl fumarate	$(CHCO_2NH_3)_2$	102	242	I

b) Inorganic phase change materials

Inorganic PCM display a high volumetric latent heat density of around 350 MJ/m^3 is also categorized as salt hydrates and metallic. They have got stable properties proved under a large number of thermal cycles and their thermal conductivity is relatively elevated of around 0.5 W/m(Lizana *et al.*, 2018). Moreover, one of the major issues is their melting process is incongruent and is corrosive to the metal container they are in.

a) Salt hydrates

Salt hydrates are inorganic salts used at a low temperature of around 30 up to 50℃ (Prasad *et al.*, 2019). These are water-containing crystallization materials with a general formula AB.nH2O (Zhang *et al.*, 2016). Two major events could happen during phase transformation which may be anhydrous salt and water or a lower hydrate and water. Supported the melting performance, salt hydrates are categorized as Congruent salt hydrates during which salt dissolves in hydration, water during melting, incongruent salt hydrates don't seem to be soluble in hydration water while melting. After the natural process, the liquid and solid phases have different compositions on semi-congruent salt hydrates because of the transformation of the salt hydrate to salt hydrate having a fewer amount of hydration water. Numerous salt hydrates with the flexibility to satisfy the PCM requirements melt incongruently. During the dehydration cycle, the crystalline salt formed is not dissolved by the released water while changing the phase. Thanks to density difference, the lower hydrate (or anhydrous salt) settles down on the underside of the container. This can be a major technological issue for realistic implementations. One of the strategies accustomed to avoiding isolation and sedimentation of the heavier transition is adding gelling or thickening agents. The incorporation of the polymeric, or cellulosic gelling substance onto the salt avoids salt sedimentation because the thickening agent improves the viscosity of the salt hydrates and aids to keep up the clusters of the salt hydrates along. Another downside of salt hydrate could be a big super cooling effect. Due to its weak nuclear capability, nuclear agents are inserted to avoid this issue. The nucleating agents like borax and carbon and others enable the regulation of the cooling process, but by minimizing thermal conductivity (Xie *et al.*, 2017). **Table 2.7** below shows the melting point and latent heat of fusion of different salt hydrates helps to hold the salt hydrate molecules together

Table 2.7: Melting point and latent heat of fusion of salt hydrates (Sharma *et al.*, 2009)

Material	Melting point (8C)	Latent heat (kJ/kg)	Group
$K_2HPO_46H_2O$	14.0	109	II
$FeBr_36H_2O$	21.0	105	II
$Mn(NO_3)_26H_2O$	25.5	148	II
$FeBr_36H_2O$	27.0	105	II
$CaCl_212H_2O$	29.8	174	I
$LiNO_32H_2O$	30.0	296	I
$LiNO_33H_2O$	30	189	I
$Na_2CO_310H_2O$	32.0	267	II
$Na_2SO_410H_2O$	32.4	241	II
$KFe(SO_4)_212H_2O$	33	173	I
$CaBr_26H_2O$	34	138	II
$LiBr_22H_2O$	34	124	I
$Zn(NO_3)_26H_2O$	36.1	134	III
$FeCl_36H_2O$	37.0	223	I
$Mn(NO_3)_24H_2O$	37.1	115	II
$Na_2HPO_412H_2O$	40.0	279	II
$CoSO_47H_2O$	40.7	170	I
$KF2H_2O$	42	162	III
MgI_28H_2O	42	133	III
CaI_26H_2O	42	162	III
$K_2HPO_47H_2O$	45.0	145	II
$Zn(NO_3)_24H_2O$	45	110	III
$Mg(NO_3)4H_2O$	47.0	142	II
$Ca(NO_3)4H_2O$	47.0	153	I
$Fe(NO_3)_39H_2O$	47	155	I
$Na_2SiO_34H_2O$	48	168	II
$K_2HPO_43H_2O$	48	99	II
$Na_2S_2O_35H_2O$	48.5	210	II
$MgSO_47H_2O$	48.5	202	II
$Ca(NO_3)_23H_2O$	51	104	I
$Zn(NO_3)_22H_2O$	55	68	III
$FeCl_32H_2O$	56	90	I
$Ni(NO_3)_26H_2O$	57.0	169	II
$MnCl_24H_2O$	58.0	151	II
$MgCl_24H_2O$	58.0	178	II
$CH_3COONa3H_2O$	58.0	265	II
$Fe(NO_3)_26H_2O$	60.5	126	–
$NaAl(SO_4)_210H_2O$	61.0	181	I
$NaOHH_2O$	64.3	273	I
$Na_3PO_412H_2O$	65.0	190	–
$LiCH_3COO2H_2O$	70	150	II
$Al(NO_3)_29H_2O$	72	155	I
$Ba(OH)_28H_2O$	78	265	II

$Mg(NO_3)_26H_2O$	89.9	167	II
Kal $(SO_4)_212H_2O$	91	184	II

- **Metallics**

These are a group of materials composed of low melting metals and eutectics metals. Due to their weight restrictions, these types of materials have not been seriously considered for PCM applications. Nonetheless, they are potential candidates due to the high heat of fusion per unit volume when the volume is considered. They have strong thermal conductivities so there is no need for fillers with additional weight penalties. There are exceptionally many engineering problems involved with the application of metallics. A high thermal conductivity makes a major distinction between metallics and other PCMs. Some of the characteristics of these materials are low specific heat, high thermal conductivity, the high heat of volume per unit volume, low heat of fusion(Mohamed *et al.*, 2017). **Table 2.8** below shows the properties of metallics materials

Table 2.8: Melting point and latent heat of fusion of metallics (Sharma *et al.*, 2009)

Material	Melting point (8C)	Latent heat (kJ/kg)	Group
Gallium–gallium antimony eutectic	29.8	–	–
Gallium	30.0	80.3	I
Cerrolow eutectic	58	90.9	–
Bi–Cd–In eutectic	61	25	–
Cerrobend eutectic	70	32.6	I
Bi–Pb–In eutectic	70	29	–
Bi–In eutectic	72	25	–
Bi–Pb–tin eutectic	96	–	–
Bi–Pb eutectic	125	–	–

- **Molten salts**

The most thermal energy storage materials used in CSP applications are molten salts(Zhang, Ma, and Xiao, 2016). Compared to other fluid storage media, nitrates molten salts are inexpensive and their high density and high energy density make them more competitive. Molten salts have a lower pressure than water and can function in liquid states up to 400°C at high temperatures. This enables the plant to run at high temperatures to enhances the ranking cycle performance. A lower melting point near room temperature is required to keep molten salts at a liquid state, and antifreeze is necessary at night, where solar energy is not present. Melting points above 200°C are typically a downside for molten salts. Nowadays, though, it is possible to use a different mixture of salts that reduce the melting point below 100°C and still have a maximum temperature above 500°C. Molten salts, can be used as heat transfer fluid (HTF), but an antifreeze agent is required to tackle the possibility of freezing, otherwise,

mineral oil, is used as HTF. One of the challenges in using molten salts is that they are highly corrosive and oxidizing agents. During the melting process, their volume increases by 6%, and their thermal conductivity is relatively low. **Table 09** below shows some thermophysical properties of molten salts.

Table 2.9: Properties of commonly used molten salts as TES in CSP (Ding *et al.*, 2018)

Molten salts composition (wt. %)	Melting point (°C)	Stability limit (°C)	Viscosity (mPa s)	Density (g cm^{-3})	Heat capacity (kJ kg^{-1} K^{-1})
Solar Salt $NaNO_3/KNO_3$ (60/40)	222	600	3.26 (300°C)	~1.84	~1.5 (560°C)
Hitec $NaNO_3/KNO_3/NaNO_2$ (7/53/40)	142	535	3.16 (300°C)	~1.9	1.56 (300°C)
LiNaK carbonates $Li_2CO_3/Na_2CO_3/K_2CO_3$ (32.1/33.4/34.5)	~400	800-850	4.3 [3] (800°C)	1.85	~1.4-1.5
LiNaK fluorides KF/LiF/NaF (59/29/12)	454	>700	N/A	1.89	1.89 (700°C)
ZnNaK chlorides $ZnCl_2$/NaCl/KCl (68.6/7.5/23.9)	204	850	4 (600800°C)	~2	0.81 (300-600°C)
MgNaK chlorides $MgCl_2$/NaCl/KCl (68.2/14.0/17.8)	380	>800	4 (500800°C)	~1.65	~1.0 (500- 800°C)

c) Eutectic

Eutectic is a mixture consisting of two or more elements, such as inorganic-inorganic, organic-organic, Inorganic-organic. For each of these mixtures, the phase transformations occur in the same way. Eutectics materials form a mixture of the component crystal during crystallization and have a specific melting and freezing point. Besides, eutectics melt and freeze regularly the same and leave a little risk of components being removed (Reddy, Mudgal, and Mallick, 2018)

Table 2.10: List of organic and inorganic eutectics(Sharma *et al.*, 2009)

Material	Composition (wt.%)	Melting point (8C)	Latent heat (kJ/kg)	Group
$CaCl_26H_2O$ + $CaBr_26H_2O$	45 + 55	14.7	140	–
Triethylolethane + water + urea	38.5 + 31.5 + 30	13.4	160	I
C14H28O2 + C10H20O2	34 + 66	24	147.7	–
$CaCl_2$ + $MgCl_26H_2O$	50 + 50	25	95	II
CH_3CONH_2 + NH_2CONH_2	50 + 50	27	163	II
Triethylolethane + urea	62.5 + 37.5	29.8	218	I
$Ca(NO_3)4H_2O$ + $Mg(NO_3)_36H_2O$	47 + 53	30	136	–
$CH_3COONa3H_2O$ + NH_2CONH_2	40 + 60	30	200.5	I

$NH_2CONH_2 + NH_4NO_3$	53 + 47	46	95	II
$Mg(NO_3)_36H_2O + NH_4NO_3$	61.5 + 38.5	52	125.5	I
$Mg(NO_3)_36H_2O + MgCl_26H_2O$	58.7 + 41.3	59	132.2	I
$Mg(NO_3)_36H_2O + MgCl_26H_2O$	50 + 50	59.1	144	–
$Mg(NO_3)_36H_2O + Al(NO_3)_29H_2O$	53 + 47	61	148	–
$CH_3CONH_2 + C_{17}H_{35}COOH$	50 + 50	65	218	–
$Mg(NO_3)_26H_2O + MgBr_26H_2O$	59 + 41	66	168	I
Naphthalene + benzoic acid	67.1 + 32.9	67	123.4	–
$NH_2CONH_2 + NH_4Br$	66.6 + 33.4	76	151	II
CONTINUED				–
CONTINUED				
$LiNO_3 + NH_4NO_3 + NaNO_3$	25 + 65 + 10	80.5	113	
$LiNO_3 + NH_4NO_3 + KNO_3$	26.4 + 58.7 + 14.9	81.5	116	–
$LiNO_3 + NH_4NO_3 + NH_4Cl$	27 + 68 + 5	81.6	108	–

2.5 Previous work on latent heat storage materials and thermal conductivity and Cp enhancement

Many PCMs have been reviewed in the literature for different temperature ranges, being considered as phase change material according to their melting temperature and phase change enthalpy for that, (S.M. Hasnain et al.,1998) summarised different parameters. Phase Change Materials (PCMs) are materials using latent heat for energy storage during the change of state. When the temperature from the source increases, the chemical bonds inside the PCM disintegrate as the material undergoes a phase transformation from solid to liquid or vice versa. The phase change is an endothermic process and for that reason, the PCM absorbs heat. While stocking heat, the material undertakes a melting process when the temperature of phase transformation gets to the limit. Two significant advantages are mainly noted while using latent heat storage firstly, a huge amount of heat can be stored with minor temperature changes so that high storage density is obtained. Secondly, it is possible to control the temperature variations due to the slow completion of the phase transformation. Compared to sensible heat storage, latent heat storage reveals that 5 to 14 times higher storage densities may be achieved (Sidik *et al.*, 2018).

Current studies support the use of latent heat due to their capabilities of stocking a large amount of heat. (Tian and Zhao, 2013) in their review of solar collectors and thermal energy in solar thermal applications showed the importance and the support of using latent heat storage materials. In the same line, (Sharma *et al.*, 2009) support the use of latent heat storage material due to its ability to provide high-energy storage density and its characteristics to store heat at a constant temperature corresponding to the phase-transition temperature of phase change material (PCM). (Cárdenas and León, 2013) said, given its

characteristics, the phase change materials (latent heat storage materials) are chosen over sensible heat materials primarily for applications where volume and weight are restrictions and therefore a high energy density is required or when there is a load whose power input must be at constant temperature. Others like (Wei *et al.*, 2018) showed the advantages of using latent heat of energy storage. For concentrated solar power (CSP) applications, molten salt with especially a mixture of 60 wt% $NaNO_3$ and 40wt% KNO_3 have been used exclusively (Zhang, Ma, and Xiao, 2016). Those multi-component salt mixtures feature much lower melting points compared to single solar Salt and could be attractive materials for direct thermal energy storage for CSP applications (Pfleger *et al.*, 2015). A review has been carried out of the history of thermal energy storage with solid-liquid phase change. It contains over 150 materials used in research as PCMs and about 45 commercially available PCMs (Zalba *et al.*, 2003). The drawback of using molten salts is that they've suffered from low thermal conductivity and specific heat. (Awad, Burns, *et al.*, 2018) investigated the effect of nanoparticles on a mixture of molten salts. They showed that the salt thermal conductivity and specific heat was low compared to nanosalt.

A. Thermal conductivity enhancement

A phase change material PCM can be mixed with different other materials to form a composite with additional or modified properties. Different ways can be used to form a composite as shown in fig. 2.5: by embedding another material into a PCM or by embedding the PCM into a matrix of another material.

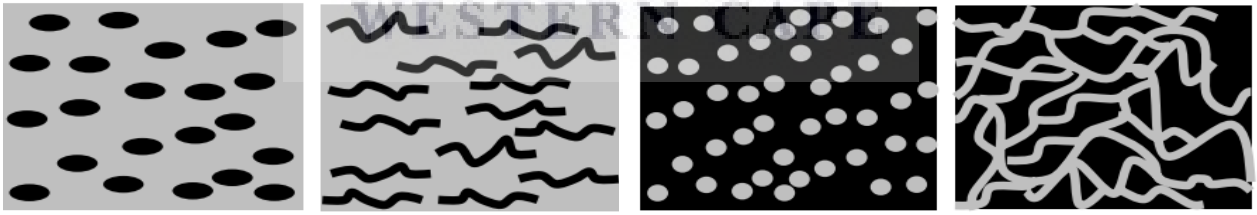

Particles and fibers embedded in a PCM (grey) material

Examples:

- Graphite fibers
- Metallic particles and fibers

PCM (grey) embedded in a matrix with pores or channels

Examples:

- Graphite matrix
- Metallic matrix/foam

Fig. 2.3: Schematic of composite material, and some examples adapted from (Cabeza and Mehling, 2008)

All Phase Change Material (PCM) and including non-metallic liquids suffer from low thermal conductivity. Although PCM holds huge quantities of heat or cold in a limited

volume, it is important to transfer this heat outside the storage zone to be used but, low thermal conductivity may be a concern. During the liquid phase, convection may improve heat transfer dramatically, but this is still not enough. However, during the solid-phase convection does not occur. If rapid heat transfer is desired, the thermal conductivity of PCM may also be improved by the use of materials with greater thermal conductivity. This can be achieved macroscopically, e.g. by inserting metallic pieces, or on a sub-mm scale as described previously on composite materials. Adding particles or anything to the PCM will, therefore, lower or remove convection during the liquid phase; for that, it is important to make better choices(Cabeza and Mehling, 2008). Recent studies have been conducted for thermal conductivity enhancement. (Pereira da Cunha and Eames, 2016) have shown that using sparse metal matrices is another way to improve thermal conductivity.

In the same way, thermal conductivity can be enhanced by using a small percentage by volume of metallic particles such as aluminum, copper, silver, nickel, or graphite. An extensive study on thermal conductivity enhancement has been done by (Gasia, Miró, and Cabeza, 2016). Figure 2.6 shows a summary of different techniques for thermal conductivity enhancement.

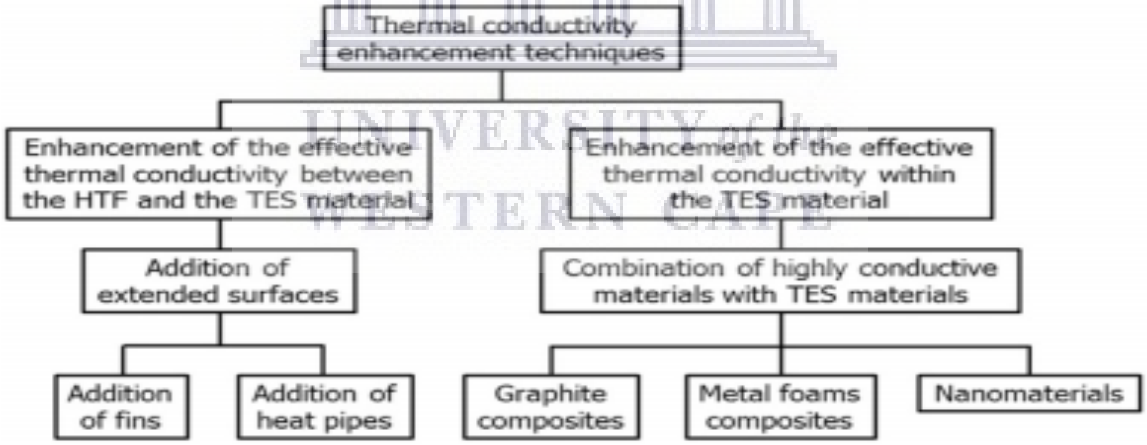

Fig.2.4: Thermal conductivity enhancement techniques for high-temperature purposes adapted from (Gasia, Miró and Cabeza, 2016)

In summary, studies show that the combination of highly conductive materials with TES materials could enhance thermal conductivity. For that, (Bauer et al.,2006) studied the improvement of KNO3/NaNO3 by investigating the impact of adding natural graphite (NG) and compressed expanded graphite (CEG) with the infiltration route and adding commercial EG (CFG 500) with the compression route varying the graphite concentration and orientation.

Results showed an enhancement of the thermal conductivity in the range from 3 to 30 times if compared to the single TES material. In addition to the compression method used to prepare the composite material, the thermal conductivity of the composite depends on their graphite concentration (the higher the graphite concentration, the higher the conductivity), and the higher the temperature is, the lower the conductivity and also on the orientation, when, the thermal conductivity of the infiltrated composites at low graphite concentration exceeded large concentrations. Focusing on metal foams as thermal conductivity enhancers, few studies have been reported at high temperatures (Chen and Carroll, 2002). Worked on TES materials filled with metal foams and the results of introducing metal foams on the convection, conduction, and phase change heat transfer procedures of the composite were studied. They concluded that high thermal conductivity was observed on the metal foams composites and could lead to the uniformity of the temperature distribution to be enhanced. However, metal foam decreases significantly the natural convection, for analogous reasoning than in the graphite composites, urging the researchers to consider the effects of porosity and pore size on both the conduction and convection heat transfer. Focusing on the nanomaterials, which are a mixture of a base material and nanoparticles, where a base material can be in a solid-state or liquid state, extensive work has been done. For that, (Awad, Navarro, *et al.*, 2018). investigated the effect of seeding iron oxide (Fe_2O_3), titanium dioxide (TiO_2), and copper oxide (CuO) nanoparticles onto molten salts ($NaNO_3$ and KNO_3) for sensible, latent heat storage and concluded that nanoparticles have a huge impact on the thermal conductivity and those small concentrations of nanoparticles were preferred for thermal conductivity enhancement.(Lasfargues *et al.*, 2015) studied the mechanical dispersion of (CuO) and (TiO_2) on molten salts and concluded that Cp enhancement was observed with a small number of nanoparticles. (Jegadheeswaran and Pohekar, 2009) reviewed the performance enhancement in latent heat storage and concluded that different techniques could be implemented for thermal conductivity improvement. (Zalba *et al.*, 2003) overviewed the literature on molten salt-based nanofluids as efficient heat transfer and storage material concluded that many parameters must be taken into account for thermal conductivity and specific heat enhancement for base salt using NPS. (Kibria *et al.*, 2015) reviewed current experimental studies on variations in the thermophysical properties of PCM due to the dispersion of nanoparticles and concluded that dispersing NP to improve the thermal conductivity for the PCM has a positive and also negative impact. The types of nanoparticles are as follow(Alva *et al.*, 2017):

- ✓ Carbon-based nanostructure nanofibers, nanoplatelets, graphene flakes, and carbon nanotubes.
- ✓ Metallic (Ag, Al, C/Cu, and Cu)
- ✓ Metal oxide (Al2O3, CuO, NiO, SiO2, ZnO, MgO, and TiO2).
- ✓ Silver nanowires

B. Heat Specific Enhancement

Like with the thermal conductivity enhancement, different methods could be used to improve the specific heat and some studies have shown that the addition of extended surfaces could lead to Cp enhancement. (Agyenim *et al.*, 2010) tested a compact horizontal tube in tube container using erythritol as the PCM, using axial fins to enhance heat transfer. They found for this system melting/solidifying properties that would provide a suitable heat source for driving an absorption cooling system. (Pereira da Cunha and Eames, 2016) Studied the effect of different nanoparticles with different mass concentrations and concluded that the specific heat capacity of the salt-containing nanoparticles at low concentrations (up to 1.0wt %) was higher compared to that of the base salt. Adding more nanoparticles (i.e., 1.5wt% and above), however, leads to a relative reduction in specific heat capacity. Adding nanoparticles for thermal conductivity enhancement, hence improves the specific heat**.** (Dudda and Shin, 2013) studied the effect of nanoparticles on the specific heat capacity of a binary nitrate salt for that, SiO2 (1% by weight) was added to the binary salt (NONO3 and KNO3) and observed the gradual increase of specific heat of nanomaterials with the increase in the number of nanostructures.

2.6 Conclusion

Phase change material is an important way of stocking thermal energy. In the literature, extensive work has been reviewed concerning thermal energy storage from sensible, latent, and chemical. Molten salts have shown a huge interest in studies due to their thermophysical properties. This literature aimed to review different existing PCMs and their selection criteria for the use of latent heat. The reviewed literature suggested that they are advantages to using PCMs through latent heat storage due to the high volume density that can be achieved and therefore, allow the stoking of a large amount of heat. Unfortunately, their low thermal conductivity and specific heat prevent them from large implementation. If enhanced, latent heat storage could lead to better use when there is no sunlight in CSP. Current research supports the use of latent heat storage as discussed above. However, a continuation of current

research with consistent and strengthened methodologies will help justify its use and application in CSP since most of them use sensible heat storage.

2.7 References

Agyenim, F. *et al.* (2010) 'A review of materials, heat transfer and phase change problem formulation for latent heat thermal energy storage systems (LHTESS)', *Renewable and Sustainable Energy Reviews*, 14(2), pp. 615–628. DOI: 10.1016/j.rser.2009.10.015.

Alva, G. *et al.* (2017) 'Thermal energy storage materials and systems for solar energy applications', *Renewable and Sustainable Energy Reviews*. Elsevier, 68(February 2016), pp. 693–706. DOI: 10.1016/j.rser.2016.10.021.

Awad, A., Burns, A., *et al.* (2018) 'Latent and sensible energy storage enhancement of nano-nitrate molten salt', *Solar Energy*. Elsevier, 172(November 2017), pp. 191–197. DOI: 10.1016/j.solener.2018.04.012.

Awad, A., Navarro, H., *et al.* (2018) 'Thermal-physical properties of nanoparticle-seeded nitrate molten salts', *Renewable Energy*, 120, pp. 275–288. DOI: 10.1016/j.renene.2017.12.026.

Ayyappan, S., Mayilsamy, K. and Sreenarayanan, V. V. (2016) 'Performance improvement studies in a solar greenhouse drier using sensible heat storage materials', *Heat and Mass Transfer/Waerme- und Stoffuebertragung*. Springer Berlin Heidelberg, 52(3), pp. 459–467. DOI: 10.1007/s00231-015-1568-5.

Baetens, R., Jelle, B. P. and Gustavsen, A. (2010) 'Phase change materials for building applications: A state-of-the-art review', *Energy and Buildings*, 42(9), pp. 1361–1368. DOI: 10.1016/j.enbuild.2010.03.026.

Cabeza, L. . and Mehling, H. (2008) *Heat and cold storage with PCM. An up to date introduction into basics and applications - Publisher: Springer; ISBN:978-3-540-68557-9, Heat and Mass Transfer*. Available at: http://www.springer.com/us/book/9783540685562.

Cáceres, G. *et al.* (2017) 'Encapsulated nitrates phase change material selection for use as thermal storage and heat transfer materials at high temperature in concentrated solar power plants', *Energies*, 10(9). DOI: 10.3390/en10091318.

Cárdenas, B. and León, N. (2013) 'High-temperature latent heat thermal energy storage: Phase change materials, design considerations and performance enhancement techniques', *Renewable and Sustainable Energy Reviews*. Elsevier, 27, pp. 724–737. DOI: 10.1016/j.rser.2013.07.028.

Chen, S. and Carroll, D. L. (2002) 'For Evaluation Only. Synthesis and Characterization of Truncated Triangular Silver Nanoplates', *Nano LETTERS*, 2(C), pp. 1003–1007.

Chieruzzi, M. and Adio, M. (2016) '16 th CIRIAF National Congress', (April).

Ding, W. *et al.* (2018) 'Electrochemical measurement of corrosive impurities in molten chlorides for thermal energy storage', *Journal of Energy Storage*, 15(January 2019), pp. 408–414. DOI: 10.1016/j.est.2017.12.007.

Dudda, B. and Shin, D. (2013) 'Effect of nanoparticle dispersion on the specific heat capacity of a binary nitrate salt eutectic for concentrated solar power applications', *International Journal of Thermal Sciences*. Elsevier Masson SAS, 69, pp. 37–42. DOI: 10.1016/j.ijthermalsci.2013.02.003.

Fernandes, D. *et al.* (2012) 'Thermal energy storage: "How previous findings determine current research priorities"', *Energy*. Elsevier Ltd, 39(1), pp. 246–257. DOI: 10.1016/j.energy.2012.01.024.

Gasia, J., Miró, L. and Cabeza, L. F. (2016) 'Materials and system requirements of high-temperature thermal energy storage systems: A review. Part 2: Thermal conductivity enhancement techniques', *Renewable, and Sustainable Energy Reviews*. Elsevier, 60, pp. 1584–1601. DOI: 10.1016/j.rser.2016.03.019.

Jegadheeswaran, S. and Pohekar, S. D. (2009) 'Performance enhancement in latent heat thermal storage system : A review', 13, pp. 2225–2244. DOI: 10.1016/j.rser.2009.06.024.

Kibria, M. A. *et al.* (2015) 'A review on thermophysical properties of nanoparticle dispersed phase change materials', *Energy Conversion and Management*. Elsevier Ltd, 95, pp. 69–89. DOI: 10.1016/j.enconman.2015.02.028.

Kuravi, S. *et al.* (2013) 'Thermal energy storage technologies, and systems for concentrating solar power plants', *Progress in Energy and Combustion Science*. Elsevier Ltd, 39(4), pp. 285–319. DOI: 10.1016/j.pecs.2013.02.001.

Lasfargues, M. *et al.* (2015) 'Mechanical dispersion of nanoparticles and its effect on the specific heat capacity of impure binary nitrate salt mixtures', *Nanomaterials*, 5(3), pp. 1136–1146. DOI: 10.3390/nano5031136.

Liu, M. *et al.* (2016) 'Review on concentrating solar power plants and new developments in

high-temperature thermal energy storage technologies', *Renewable and Sustainable Energy Reviews*. Elsevier, 53, pp. 1411–1432. DOI: 10.1016/j.rser.2015.09.026.

Lizana, J. *et al.* (2018) *Identification of best available thermal energy storage compounds for low-to-moderate temperature storage applications in buildings, Materiales de Construccion*. DOI: 10.3989/mc.2018.10517.

Mohamed, S. A. *et al.* (2017) 'A review on the current status and challenges of inorganic phase change materials for thermal energy storage systems', *Renewable and Sustainable Energy Reviews*, 70(December 2016), pp. 1072–1089. DOI: 10.1016/j.rser.2016.12.012.

Pereira da Cunha, J., and Eames, P. (2016) 'Thermal energy storage for low and medium temperature applications using phase change materials - A review', *Applied Energy*. Elsevier Ltd, 177, pp. 227–238. DOI: 10.1016/j.apenergy.2016.05.097.

Pfleger, N. *et al.* (2015) 'Thermal energy storage - overview and specific insight into nitrate salts for sensible and latent heat storage', *Beilstein Journal of Nanotechnology*, 6(1), pp. 1487–1497. DOI: 10.3762/bjnano.6.154.

Prasad, D. M. R. *et al.* (2019) 'A critical review on thermal energy storage materials and systems for solar applications', *AIMS Energy*, 7(4), pp. 507–526. DOI: 10.3934/energy.2019.4.507.

Reddy, K. S., Mudgal, V. and Mallick, T. K. (2018) 'Review of latent heat thermal energy storage for improved material stability and effective load management', *Journal of Energy Storage*. Elsevier Ltd, 15, pp. 205–227. DOI: 10.1016/j.est.2017.11.005.

Rout, C. and Sharma, A. (2013) 'Recent Advancement in Phase Change Materials for Thermal Applications : A Recent Advancement in Phase Change Materials for Thermal Applications : A Review', (November).

Sarbu, I. and Sebarchievici, C. (2018) 'A comprehensive review of thermal energy storage', *Sustainability (Switzerland)*, 10(1). DOI: 10.3390/su10010191.

Sharma, A. *et al.* (2009) 'Review on thermal energy storage with phase change materials and applications', *Renewable and Sustainable Energy Reviews*, 13(2), pp. 318–345. DOI: 10.1016/j.rser.2007.10.005.

Sidik, N. A. C. *et al.* (2018) 'Performance enhancement of cold thermal energy storage

system using nanofluid phase change materials: A review', *International Communications in Heat and Mass Transfer*. Elsevier, 94(April), pp. 85–95. DOI: 10.1016/j.icheatmasstransfer.2018.03.024.

Tian, Y. and Zhao, C. Y. (2013) 'A review of solar collectors and thermal energy storage in solar thermal applications', *Applied Energy*, 104, pp. 538–553. DOI: 10.1016/j.apenergy.2012.11.051.

Tyagi, V. V., and Buddhi, D. (2007) 'PCM thermal storage in buildings: A state of art', *Renewable and Sustainable Energy Reviews*, 11(6), pp. 1146–1166. DOI: 10.1016/j.rser.2005.10.002.

Wei, G. *et al.* (2018) 'Selection principles and thermophysical properties of high-temperature phase change materials for thermal energy storage: A review', *Renewable and Sustainable Energy Reviews*. Elsevier Ltd, 81(March 2017), pp. 1771–1786. DOI: 10.1016/j.rser.2017.05.271.

Xie, N. *et al.* (2017) 'Inorganic salt hydrate for thermal energy storage', *Applied Sciences (Switzerland)*, 7(12). DOI: 10.3390/app7121317.

Yang, G. *et al.* (2019) 'Carbon-filled organic phase-change materials for thermal energy storage: A review', *Molecules*, 24(11). DOI: 10.3390/molecules24112055.

Zalba, B. *et al.* (2003) *Review on thermal energy storage with phase change: Materials, heat transfer analysis and applications, Applied Thermal Engineering*. DOI: 10.1016/S1359-4311(02)00192-8.

Zhang, H. *et al.* (2016) 'Thermal energy storage: Recent developments and practical aspects', *Progress in Energy and Combustion Science*. Elsevier Ltd, 53, pp. 1–40. DOI: 10.1016/j.pecs.2015.10.003.

Zhang, P., Ma, F. and Xiao, X. (2016) 'Thermal energy storage and retrieval characteristics of a molten-salt latent heat thermal energy storage system', *Applied Energy*, 173, pp. 255–271. DOI: 10.1016/j.apenergy.2016.04.012.

Bauer, T., do CoutoAktay, K.S., Christ, M., Öttinger, O., Tamme, R. (2006) PCM-Graphite Composites for High Temperature Thermal Energy Storages, ECOSTOCK 2006, Stockton, New Jersey, 31.5–2.6.2006

S. M. Hasnain, “Review on sustainable thermal energy storage technologies. Part I. Heat storage materials and techniques,” Energy Conversion and Management, vol. 39, no. 11, pp. 1127– 1138, 1998

CHAPTER THREE

MATERIALS AND CHARACTERIZATION TECHNIQUES

This chapter introduces the different materials and techniques of characterization used in this work. This includes: Scanning electron microscopy (SEM), Transmission electron microscopy (TEM), X-Ray diffraction (XRD), Differential scanning Calorimetry (DSC), Thermogravimetric analysis (TGA), and the Ultraviolet-visible spectroscopy (UV-VIS) were used to characterize silver nanowires synthesized by Polyol technique and the mixture of the salt and nanosalt. All the experiments were performed at the University of Western Cape and Ithemba Labs.

3.1 Materials

Silver nitrate (AgNO3, 99.8 %), ethylene glycol (EG, 99.8 %), PVP (Mw: 3600000), anhydrous ethanol (EtOH, 98 %), Sodium nitrate ($NaNO_3$), and (KNO_3) were purchased from Sino Pharm Chemical Reagent Co., Ltd., P. R. China. All chemicals were used with no further purification. The UV–visible extinction spectra were taken by the UV-1601 spectrometer (Shimadzu, Japan). The microstructure of Ag nanowires was characterized by field emission scanning electron microscopy at an acceleration voltage of 15 kV. TEM images and electron diffraction patterns were taken by JEOL-JEM 2010 microscope operated at 200 kV. The X-ray powder diffraction (XRD) patterns were recorded using a Rigaku diffractometer with the CuKa radiation (k = 1.54060 A °) at a scanning rate of 15_/min in 2h ranging from 30_ to 90_. Thermal analysis (TG-DSC) was taken on Simultaneous Thermal Analyzer (STA449C) under the nitrogen atmosphere at the heating rate of 10 K/min.

Figure 3.1: Different materials used in this project

3.2 Characterization techniques

Different techniques have been used to characterize all the samples. In this chapter, an overview of the techniques and sample preparation is discussed. **Table 3.1** gives a brief description of all characterization techniques used in this study.

Table 3.1. Characterization techniques that have been used in this study

Characterization techniques	information obtained
Scanning Electron Microscopy	Morphology and topography of AgNWs
Transmission Electron Microscopy (TEM)	Grain size and morphology
Energy Dispersive X-ray Diffraction (EDS)	Elemental Composition
X-ray Diffraction	Crystallinity, dimensions
Differential Scanning Calorimetry (DSC)	Heat flow of the sample
Thermo Gravimetric analysis (TGA)	Weight loss of the sample
Ultraviolet-Visible Spectroscopy (UV-Vis)	Optical properties

3.3 Scanning Electron Microscopy (SEM) and Energy Dispersive Spectroscopy (EDS)

3.3.1 Sample Preparation

A powder of silver nanowires was used and coated with a carbon layer Using a coating sputter (quorum Q 150 TES) to increase the sample's conductivity, a powder of silver nanowires was used and coated through a carbon layer. SEM and EDS were performed under Carl Zeiss Auriga Field Emission Scanning Electron Microscope (FEG SEM) imaging at 5kev. EDS spectra were recorded with an oxford instruments X-max solid-state silicon drift detector at 20 KeV

3.3.2 Scanning Electron Microscopy (SEM)

Scanning electron microscopy (SEM) is a microscope used to study the microstructure of the bulk material. It is an electron optical instrument that focuses a beam of the electron to generate a three-dimensional image of an object (MAGUBANE, 2018). In the sample, the interaction between electrons and atoms generates different signals that contain information about the surface and the chemical composition of the sample. In combination with the closely related method of energy-dispersive X-ray spectroscopy (EDX, EDS), the structure of specific crystals or characteristics can be determined (TIEDT, L.R., 2002). A raster scan pattern is utilized to analyze the electron beam and, the direction of the beam is correlated with the intensity of the signal being observed to create the image. Mostly, scanning electron microscopy uses a secondary electron detector (Everhart-Thornley detector) to detect secondary electrons escaped by atoms excited by the electron beam. SEM can reach a

resolution of more than 1 manometer(Stokes, 2008). To prevent high voltage discharge and dispersion of electrons in the direction of residual gas atoms, the chamber and column must stay under vacuum(TIEDT, L.R., 2002).

3.3.3 Overview of the principle technique

The primary electron signals in scanning electron microscopy are backscattered electrons (BSEs) and secondary electrons (SEs). The signal's quality and production are affected by the surface and composition of the sample. SEM images result from variations in electron signal intensity collected at each point (pixel) as the electron beam briefly dwells within the scanned area(Stokes, 2008). Accelerated electrons in the SEM have large amounts of kinetic energy but that energy is transferred as a range of signals generated by electron-sample interactions when the incident electrons are decelerated in the solid sample. Such signals involve secondary electrons (which generate SEM images), backscattered electrons (BSEs), diffracted backscattered electrons (EBSDs used to establish crystal structures and mineral orientations), photons (characteristic X-rays used for atomic analysis and continuum X-rays), visible light (cathodoluminescent-CL) and heat (Blakey and Micklethwaite, 1978; Clarke and Eberhardt, 2002; Egerton, 2016). The brightness of a cathode ray tube (CRT) is regulated by using the output of different detectors such as backscattered and secondary electron detectors. Through scanning concurrently in two perpendicular directions, a square or a rectangular region of the samples (known as a raster) can be filled and an image of this region can be created by capturing secondary electrons within each location of the sample. The same raster-scanning signals collected can then be utilized to guide the beam generated in a cathode-ray tube (CRT) precisely in line with the motion of the electron beam on the sample (Egerton, 2016). SEM is a dynamic imaging tool that requires very precise information to be clarified and has a large depth of field, as for an optical microscope. However, to serve as an accurate analytical tool, it should be paired with correct detectors. Depending on the information required, there are different ways of operating the scanning electron microscope. When high field images are needed, a low convergence angle should be applied, to focus various heights on an uneven layer. This can be done by using a small objective aperture or a long working distance(TIEDT, L.R., 2002).

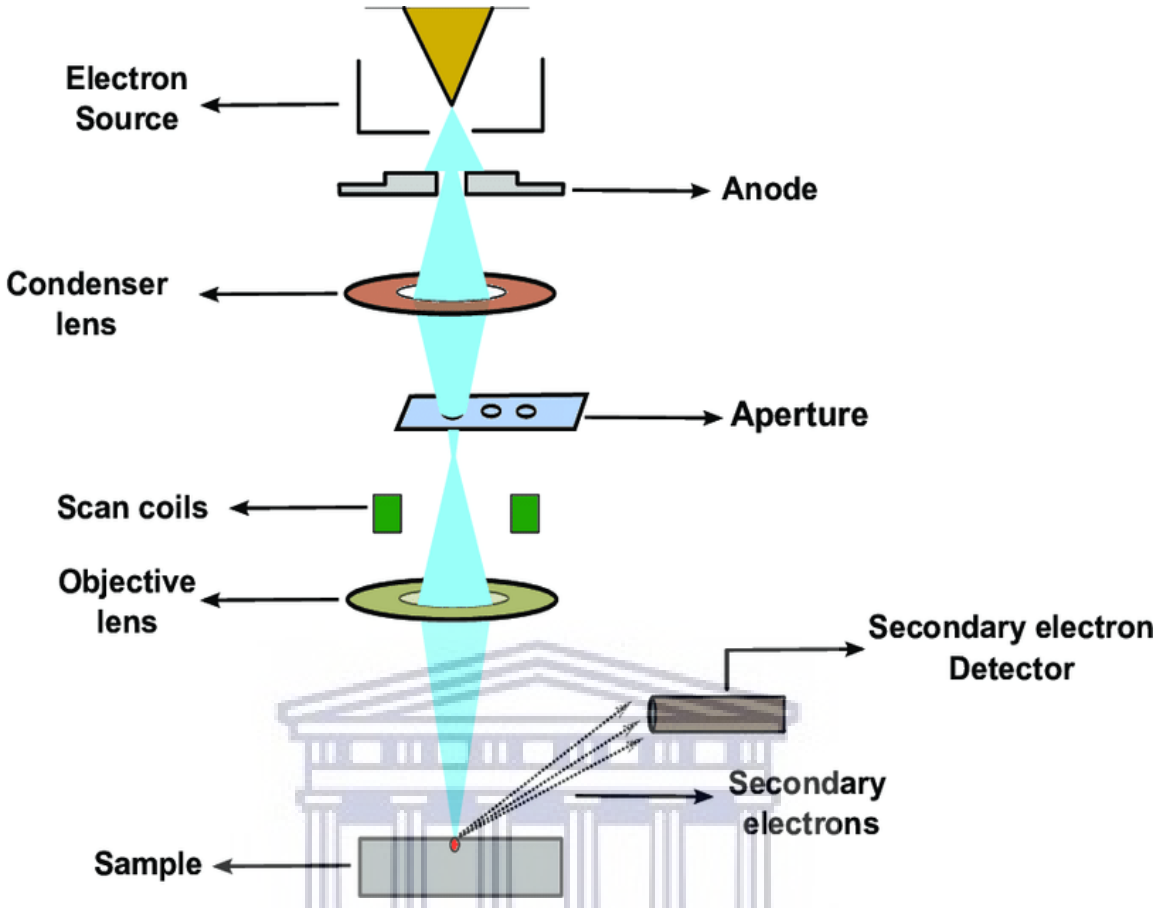

Figure 3.2: Schematic diagram of scanning electron microscopy adapted from (Marturi, 2015)

3.3.4 Environmental scanning electron microscopy

As discussed previously, specimens for conventional SEM should commonly be clean, dry, vacuum compliant, and electrically conductive (TIEDT, L.R., 2002).

The Environmental scanning electron microscopy (ESEM) is a unique system developed where an electron beam can be used to analyze uncoated biological specimens in a high chamber intensity environment of water vapour(Associates, 1996). Samples can then be examined using ESEM without damage and further preparation methods (Muscariello *et al.*, 2005).

3.3.5 ELECTRON GUN

The electron gun's function is to provide a safe supply of electrons. There are many forms of basic electron guns used in EMs that vary in design and emission characteristics. The traditional triode electron gun is the most widely used form of the electron gun, which is formed by three essential elements held in the gun chamber and under vacuum (TIEDT, L.R.,

2002). These electrons are then accelerated to a voltage between 1-40 kV and condensed into a narrow beam that is used for imaging and analysis. The three (3) commonly used types of electrons sources:

1. Tungsten filament
2. Solid-state crystal (Cerium hexaboride or Lanthanum hexaboride)
3. Field emission gun (FEG)

3.3.6 ELECTROMAGNETIC LENSES

A variety of condenser lenses concentrate the electron beam as it moves from the source down the column. The thinner the ray, the smaller the location it would have when hitting the floor, hence the concept 'spot size.

3.3.7 MAGNIFICATION

The magnification of an electron image is known as the ratio between the length of one line of the electron beam on the screen and the width of the scanned region on the sample. An improvement in magnification can be accomplished by minimizing the size of the scanned region of the sample, as the length of the CRT is set. Throughout this approach, magnifications of up to 300,000X can be obtained, assuming that all conditions required for the highest spatial resolution are configured(TIEDT, L.R., 2002). No more information is found above these magnifications of 300,000X. The working distance (WD) and the accelerating voltage on the electron beam will also affect the scanning area(Cheney, no date). However, for many-electron microscopes, only the scanning signal is related to the magnification gauge. Therefore, additional calibration is required if accurate magnification is needed.

3.3.8 Energy Dispersive Spectroscopy (EDS)

Energy-dispersive X-ray spectroscopy also referred to as energy-dispersive X-ray analysis or energy-dispersive X-ray microanalysis, is an analytical method utilized for atomic analysis or chemical composition of the material. Wavelength-dispersive spectrometers(WDS) utilizing the Bragg-reflection such a single crystal are primarily used in x-ray microprobes, although some SEMs are still mounted with this kind of spectrometer that has a higher range, on the order of 5-20 EV, although with a lower solid angle of the array. Energy-dispersive spectrometers have the benefit that all quantum energies between 0.2-20 keV are reported at

the same time as well as the spectrum is viewed directly throughout the multi-channel analysis tool (L. Reimer, 1998). Chemical analysis in the scanning electron scanning is done by calculating the energy and intensity spectrum of the x-ray signal produced by the electron beam. Throughout the years there's been a major increase in performance of sensors from 500 eV to less than 130 eV resolutions, rendering the tool far more appropriate for microanalysis needs. EDS is most frequently employed in conjunction and wavelength-dispersive spectrometers (WDS) and electron microprobe analysis tools (R.F. Egerton, 2016**).**

3.3.9 TYPES OF SIGNAL

The electrons interact with the atoms at or close to the sample surface producing signals which contain information on the sample's surface topography, composition, and other properties such as electrical conductivity. Different types of signals generated by SEM include secondary electrons, back-scattered electrons (BSE), characteristic X-rays, light (cathodoluminescence), Auger electron generation. Secondary electrons have the smallest volume, followed by backscattered electrons and X-rays; this interaction volume ultimately determines both the spatial resolution and depth from which analysis can be achieved.

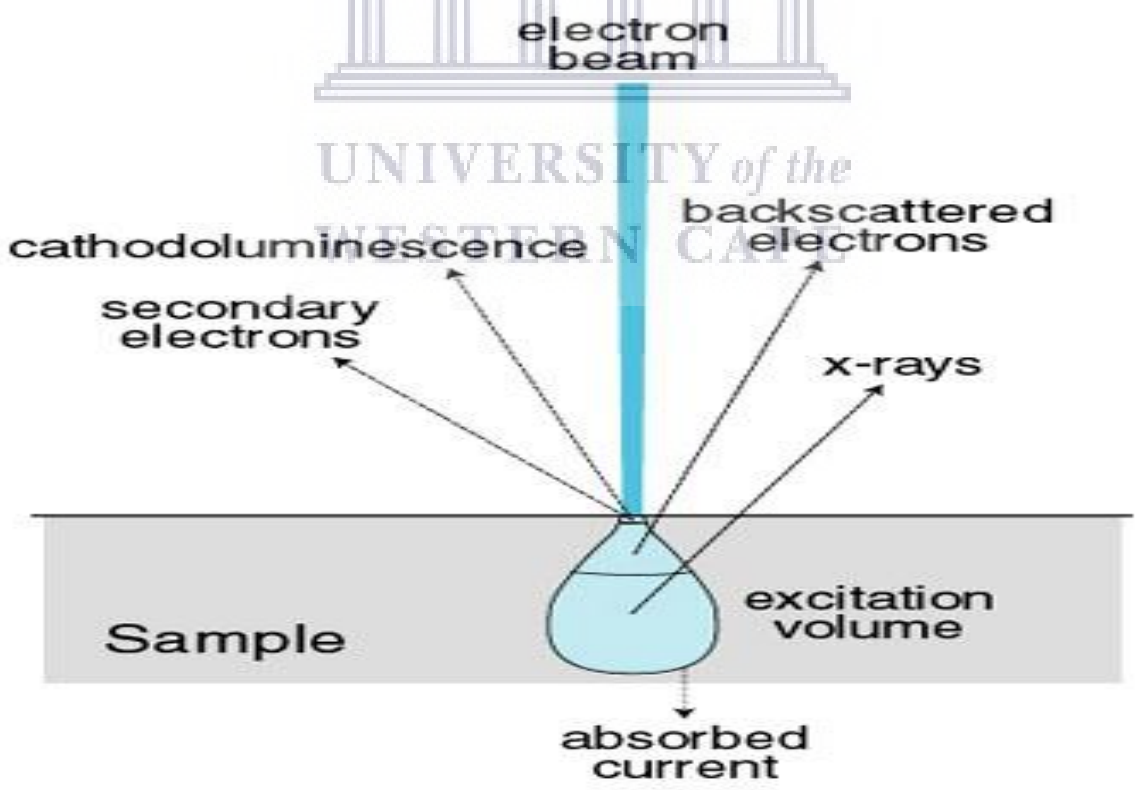

Figure 3.3: Schematic diagram of emission signals and their distribution following electron beam-sample interaction adapted from (S. R. Bacon, 2012)

a) Backscattered-Electron Images

A **backscattered electron** (BSE) is a primary electron expelled from material by scattering at an angle over 90°. Such electrons are classified as backscattered electrons, which have experienced large-angle elastic dispersion events in the material, causing the substrate to be reached with enough energy to escape. BSE is often used in analytical SEM along with the spectra made from the characteristic X-rays. Because the intensity of the BSE signal is strongly related to the atomic number (Z) of the specimen, BSE images can provide information about the distribution of different elements in the sample especially about the composition and surface topography of the specimen(L. REIMER, 1998).

b) Secondary electrons

Secondary electrons emission (SE), are the most common signals used and produced from interaction between the primary electron beam and the sample. Inelastic scattering of an energetic electron with outer valence electrons leads to the emission of secondary electrons that are characterized by having kinetic energy less than 50eV.

When the primary beam strikes the sample surface causing the ionization of specimen atoms, loosely bound electrons may be emitted and these are referred to as secondary electrons. Such electrons may be exposed to external dispersal activities through which energy is lost and therefore only electrons that have enough power to pass the surface barrier radiation and exit the material and lead to the observed signal; these are electrons on the surface of the sample. An SEM with secondary electron imaging or SEI can produce very high-resolution images of a sample surface, revealing details less than 1 nm in size(Anglani *et al.*, 1998).

c) Elemental analysis using x-ray

X-rays produced in the specimen can be used for elemental analysis of the specimen. The x-ray energy is specific for different elements.

A dedicated x-ray detector detects the x-rays deriving from every spot of the sample and assigns them according to element.

Elemental mapping is possible for any area of interest. In particular, the interpretation of x-ray spectra is very challenging and needs a lot of experience. A highly corrugated surface of a specimen – a typical biological specimen - can lead to misinterpretation.

Quantitative analysis with biological specimens is usually not possible (Blakey and Micklethwaite, 1978).

3.4 Transmission Electron Microscopy (TEM)

3.4.1 Sample Preparation

Sample for Transmission Electron Microscopy (TEM) analysis was prepared by depositing a small drop of diluted silver nanowires ultrasonicated in ethanol TEM grids. The TEM grids were coated with thin amorphous carbon support (~20nm); as it has a relatively low electron density, it provides a uniform substrate for imaging samples. The sample was left 10 minutes approximately under the lamplight to dry. The ultra-sonication procedure of the solution of silver nanowires in ethanol created colloidal dispersions without affecting the native chemical structure or composition of the material. No post-processing was conducted on the images presented by TEM. It should also be noticed that the ethanol ultra-sonication process did not appear to alter the structural or chemical properties of the synthetic. The dispersions so-produced settled upon standing for several minutes before being dropped onto lays amorphous carbon support

3.4.2 Transmission Electron Microscopy (TEM)

Transmission Electron Microscope (TEM) is a type of microscope that uses a beam of electrons to visualize and analyze specimens from the micro-scale. These electrons are transferred into an ultra-thin sample, interacting with the sample while passing through. Interactions between samples and electrons generate an image that is magnified and focused by the lenses and is detected by the CCD camera [Pavel Zinin]. Inaccessible details from light microscopy are studied using TEM as it utilizes a concentrated beam of high energy electrons. It also requires comprehensive microstructural analysis by way of high resolution and high magnification imaging. Cristal structures, sample orientation, and chemical composition are also studied from the diffraction pattern, x-ray, and electron analysis (Zhiping Luo, 2016).

3.4.3 **Overview of the principle technique**

In TEM, a highly focused electron beam emerges on a small (less than 200 nm thick) specimen. The signal in TEM is derived from both undeflected and deflected electrons, which enter the thickness of the specimen. The electron beam is of sufficient energy to propagate through the specimen, a series of electromagnetic lenses then magnifies this transmitted electron signal (Brundle, C. R et al., 1992). Diffracted electrons are observed in the form of a diffraction pattern beneath the specimen. This information is used to determine the atomic structure of the material in the sample. Transmitted electrons form images from small regions of the sample that contain contrast, due to several scattering mechanisms associated with

interactions between electrons and the atomic constituents of the sample. Analysis of transmitted electron images yields information both about atomic structure and about defects present in the material. Transmission electron microscopy is used to produce images from a sample by illuminating the sample with electrons (i.e. the electron beam). A beam of electrons with high kinetic energy is generated by the electron gun, those electrons pass across thin areas of TEM specimens and are emitted in the electron gun by thermionic, Schottky, or field emission. The latter is used when high gun brightness and coherence are needed. The emitted electrons are then accelerated through the applied potential by the anode acquiring the determined kinetic energy. Below the electron gun is two or more condenser aperture and together, they demagnify the beam emitted by the gun and control its diameter as it hits the specimen. Other components in the Transmission Electron Microscopy include objective and intermediate aperture, diffraction lenses, and intermediate and projector lenses. The role of the apertures is to control the convergence angle of the transmitted electrons down the line toward the viewing screen. An objective lens forms the first intermediate image while the diffraction lens is responsible for the diffraction pattern. Intermediate and projector lenses are used to magnify the image produced by the objective lens until it is finally projected onto the fluorescent screen. A charged coupled device (CCD) camera is used to capture the image (Goodhew, Peter. et al., 2001).

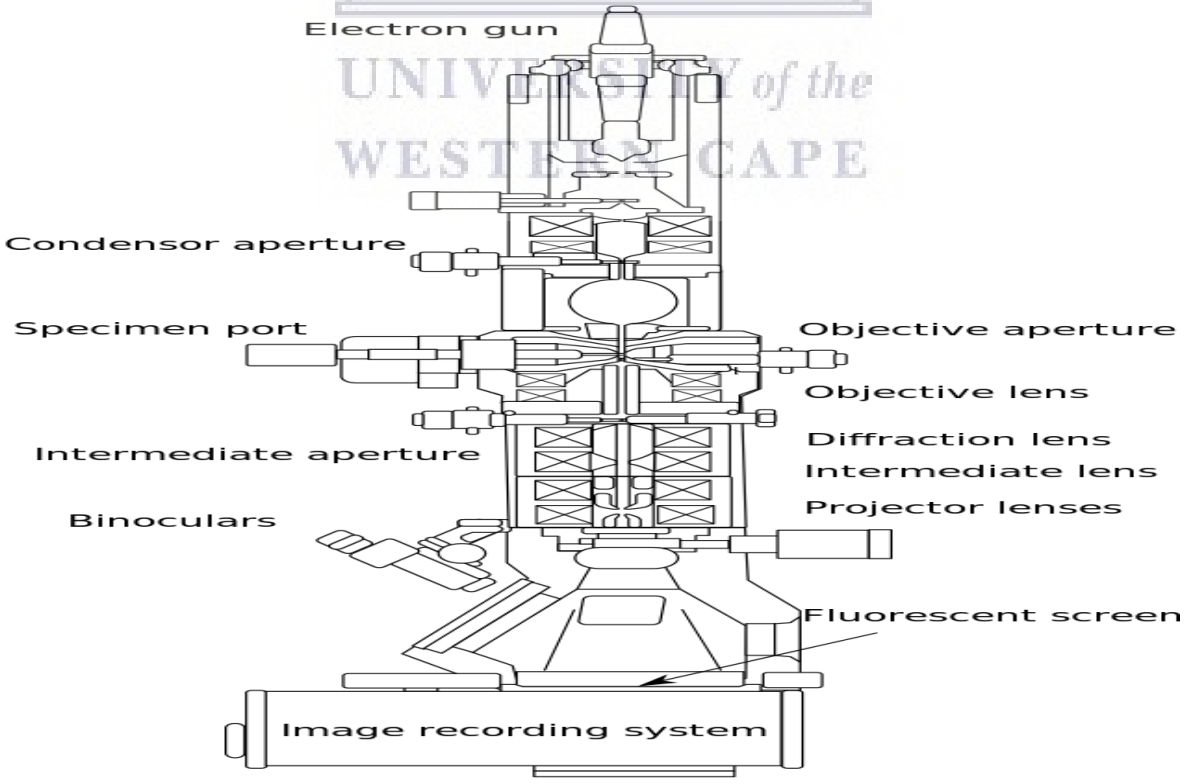

Figure 3.4: Schematic diagram of Transmission Electron Scanning (Abudayyeh, 2012)

3.4.4 Electron diffraction

Information about crystal structure and orientation is provided by the electron diffraction pattern. The possibility of combining electron diffraction and the various imaging modes is the most powerful feature of TEM for the investigation of the crystal lattice and its defects in crystalline material (Bendersky, Leonid, 2001). Similar to X-ray diffraction (XRD), electron diffraction can be defined by Bragg's law. As shown in figure 3.5, at an incident angle θ, an electron beam enters a crystal lattice with parallel planes in a spacing of thickness d. After scattering, the distance difference between two adjacent rays is 2dsinθ so when

$$2d\sin\theta = n\lambda \qquad (3.1)$$

These two rays have the same phase; the intensity along this direction is enhanced (constructive interference). Here, λ is the wavelength and n is an integral number (1, 2, 3 …).

In TEM, it is possible to select a small area for diffraction, so it is common to get selected-area electron diffraction (SAED) pattern of single crystals, while XRD single-crystal pattern requires a large sample compared with the diffracted crystal in TEM (Zhiping Luo, 2016).

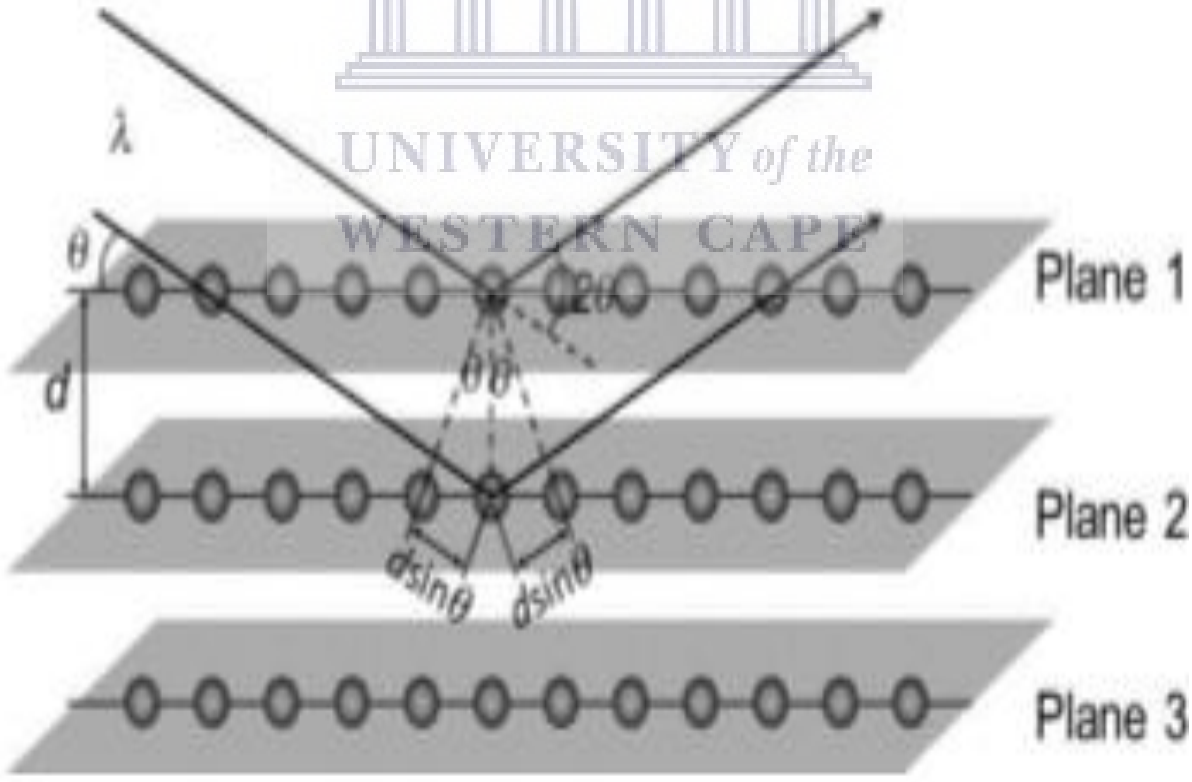

Figure 3.5: Formation of diffraction pattern by Bragg's law in electron diffraction (Zhiping Luo, 2016).

3.5 X-Ray Diffraction (XRD)

3.5.1 Samples preparation

For XRD analysis, a mixture of a final product composed of silver nanowires was dropped on a glace substrate and dried in the oven at 100℃; the glace substrate was taken to the XRD unit for analysis. Concerning nanosalt, the mixture was dried at the same temperature and sent directly for XRD analysis.

3.5.2 Overview of the principle technique

X-ray Diffraction (XRD) is a powerful technique used to uniquely identify the crystalline phases present in materials and to measure the structural properties (strain state, grain size, phase composition, preferred orientation, and defect structure) of these phases. XRD is also used to determine the thickness of thin films and multilayers, and atomic arrangements in amorphous materials (including polymers) and at interfaces.

3.5.3 Fundamental Principles of X-ray Powder Diffraction (XRD)

X-ray diffraction is built entirely upon its constructive interference of monochromatic X-rays and crystalline specimens. Such x-rays are created by a cathode ray tube, processed to create monochromatic radiation, continued to collect, and guided to the specimen. When Bragg's Law conditions of ($n\lambda=2d \sin \theta$) are met, the interaction between the incident rays and the specimen generates constructive interference. In the crystalline specimen, this law refers to the wavelength of electromagnetic radiation to the diffraction angle and the lattice thickness. Such diffract X-rays are further measured, analyzed, and recorded. Upon scanning the sample across a variety of 2θ angles, all feasible diffraction patterns of a lattice should be reached due to the random orientation of the powdered material. The transformation of the diffraction peaks to the d-spaces enables the mineral to be identified as each mineral has a series of distinct d-spacing. Usually, this is done by matching d-spacing against generic reference patterns. An X-ray tube, a sample holder, and an X-ray detector are the three basic components forming an X-ray diffractometer. X-rays are produced in a cathode ray tube by heating a filament to create electrons, speeding electrons to the target by adding a voltage and bombarding the target material with electrons. Once electrons have enough power to dissipate the ground state electrons from the target substance, the characteristic X-ray spectra are formed. Such spectra are made up of many elements, the two famous $K\alpha$ and K_β. K_α comprises, in portion, of $K_{\alpha1}$ and $K_{\alpha2}$. $K_{\alpha1}$ with a significantly shorter range and double the power of $K_{\alpha2}$. The precise wavelength is characteristic of the target material (Cu, Fe, Mo, and

Cr). With CuK_{α} radiation = 1.5418Å, copper is the most common target material used for single-crystal diffraction. Such X-rays are obtained simultaneously and directed to the specimen. The intensity of X-ray reflection is recorded during the spinning of both sample and the detector. Constructive interference and peak intensity occur when the geometry of the incident X-ray coming from the sample satisfies the Bragg Theorem. The detector tracks and measures the X-ray signal and transforms it to the count rate that is then transmitted to a system such as a printer or a computer display. (Bish, DL.et al.,1989; Cullity, B. D. 1978; Klug, H. P.et al.,1974; Moore, D. M.et al.,1997)

3.6 Differential Scanning Calorimetry (DSC)

3.6.1 Sample Preparation

For DSC measurements, nanosalt and molten salts were sampled. To achieve good measurement results the crucible/lid combination's weight on the sample and reference side should not differ more than zero points two milligrams.

3.6.2 Overview of the technique

Differential Scanning Calorimetry, or DSC, is a thermal analysis technique that looks at how a material's heat capacity (Cp) is changed by temperature. A sample of known mass is heated or cooled and the changes in its heat capacity are tracked as changes in the heat flow. This allows the detection of transitions such as melts, glass transitions, phase changes, and curing. Because of this flexibility, since most materials exhibit some sort of transitions, DSC is used in many industries, including pharmaceuticals, polymers, food, paper, printing, manufacturing, agriculture, semiconductors, and electronics. The biggest advantage of DSC is the ease and speed with which it can be used to see transitions in materials. Most of these transitions will either be exothermic or endothermic.

Exothermic: Heat is released from the sample. Endothermic: Heat is taken into the sample.

Figure 3.6: Type of Dynamic Scanning Calorimetry (DSC) used in this project

In operation, an empty pair of aluminum or copper pan and lid is usually used as the reference and the sample is placed in another pair of pan and lid with the same material and weight as the reference, so that the heat flow to the reference is canceled in software, and information of heat flow to the sample is collected. The result of a DSC experiment is a curve of heat flux versus temperature or time, and the integration of phase transition peak area on the curve indicates the latent heat of the sample.

- **Heat Flow**

DSC has the main function to measure the heat flow, that flow of energy coming in or out of the sample as a function of temperature or time, which is expressed in mW units on the y-axis. The factual value of heat flow is not complete because the measured value relies on the

impact of the reference. What counts is to generate a consistent instrumental response or baseline to assess any improvements. The initial point of the y-axis curve may be picked as one of the initial parameters and set to or near zero. There are two different heat flow curve conventions: one indicates endotherms in the bottom region and another in the upwards direction. Many program packages are available to the user. Traditionally, with heat flux systems endotherms are shown as going down since endothermic transitions result in a negative temperature differential, whilst with power compensation systems they are shown as going up since with this principle endothermic transitions result in an increase in power supplied to the sample (G. Paul, 2008)

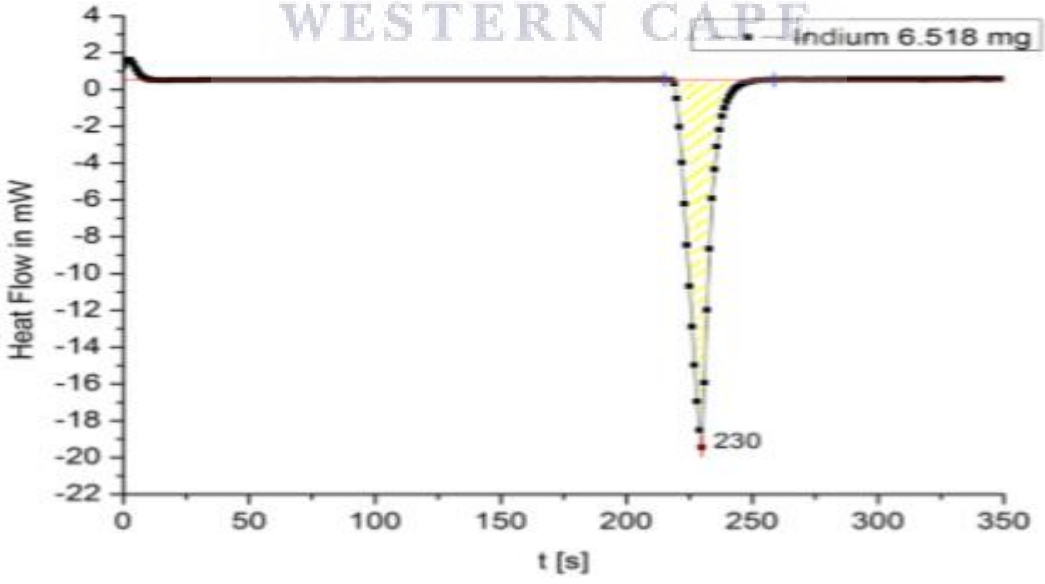

Figure 3.7: Graph displaying Heat Flow (mW) against Time (s) for the melting of Indium adapted from (Lasfargues, 2014)

- **Specific heat (Cp)**

Heat capacity (Cp) is the amount of energy a unit of matter can hold. The specific heat (heat capacity, Cp) of a material can be determined quantitatively using DSC and is designated Cp since values are obtained at constant pressure. Traditionally, this is done by subtracting a baseline from the heat flow curve in the manner described below, but values may also be obtained using modulated temperature techniques.

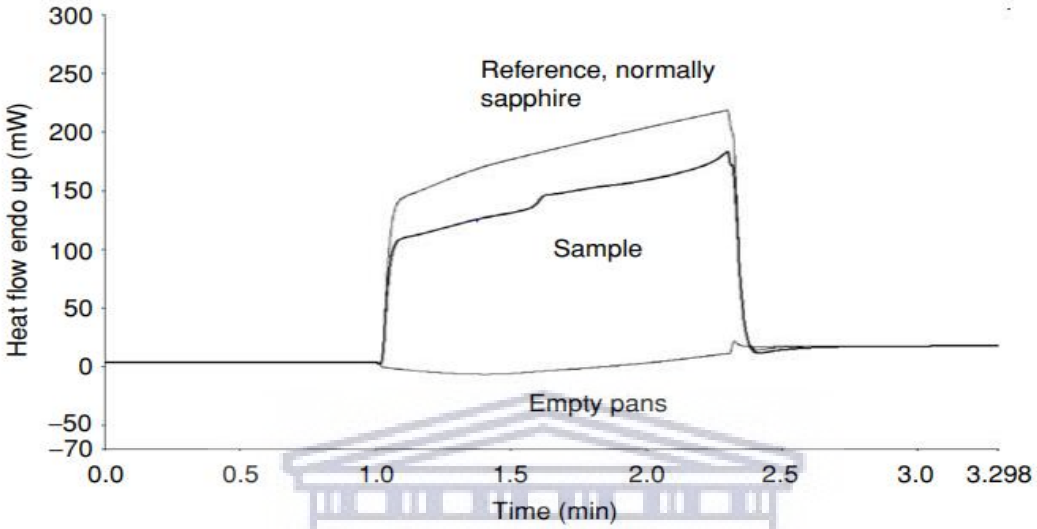

Figure 3.8: Heat capacity of PET obtained using fast scanning techniques showing the three traces required for subtraction (Gabbott. Paul, 2008).

For the Cp measurement, for instance, the height of the sample compared to the empty pan is split by the scan rate and the mass of the sample to produce a Cp value. This standard method using sapphire as a reference is used to compare with the obtained Cp values for accuracy. When, for example, small heating measures of 1◦C are utilized, the region below the curve may be used to measure Cp. This measurement is used as an alternative for stepwise heating methods (Gabbott. Paul, 2008)

The deduct curve, compared to the standard, provides the numerical value of Cp, Figure 3.9. The precision that can be achieved depends on the device and the process used. In reality, the conventional model evaluation system offers a relatively fast process for the calculation of Cp, and several manufacturers have programs precisely developed to conform to Cp. Three runs are expected, each consisting of an isothermal cycle, a temperature ramp, and a final isotherm. This approach is extended to the following sequences of runs: 1. first, run a baseline with empty pans placed in the furnace. 2. Second run: as above but adding a reference (typically sapphire) to the sample pan. 3. Third run: replace the reference with your sample. The three curves are brought up on the screen, isothermals matched, data subtracted and referenced against the standard. This can be done automatically by many software

programs, and if the variation in weight and heat capacity of the sample pans are considered, the baseline and reference runs can be utilized for subsequent tests, assuming that the DSC is reliable. As the method relies on a subtraction methodology between measurements taken at various periods, any shift can create a mistake. The DSC must remain very consistent so, in practice, it is important not to use a device at the limits of its temperature spectrum because performance can be affected. Sapphire is considered the most standard used material, so the mass used should be identical to the sample; in any case, the sample cannot be greater or the errors will be elevated. This approach depends on the calculation of the heat flow of the sample against the calculation of the empty plate. Although there can be a variety of elements that control the scanning pace of preference, it should be noticed that faster scanning speeds result in higher heat flow values allowing improved precision of calculation and this also lowers run time and possible drift of the analyzer. Studies stated that high scanning speeds used by quick scanning DSC will provide highly reliable results. This common concept is used in stepwise heating methods in which the temperature can be increased by just a fraction of a degree through a sequence of isotherms transitions.

It is stated to provide a very reliable value to Cp due to the sequence of the small temperature range. Specific heat details may be of benefit in its own right, as this knowledge is used by chemists and chemical engineers while ramping up reactions or manufacturing processes, gives guidance for mathematical simulations, and is essential for precise kinetic as well as other sophisticated measurements. This may also assist in curve analysis as the slope curve is set and complete, so minimal exothermic or endothermic effects are defined. Generally, it offers better details than heat flow traces, since the measurements are complete, and it also requires more time, sometimes in limited supply throughout the industry (Gabbott. Paul, 2008).

- **Enthalpy**

The enthalpy of a specimen refers to the amount of energy needed for the substance to be heated to a specified temperature. This is achieved by incorporating the curve of the heat capacity curve. Also, several programs are available and can be used to integrate the Cp curve to generate an enthalpy curve. Measurements can be done by using the enthalpy curves, e.g. when measuring fictive temperature; it can be useful to explain why the transitions appeared with a given configuration. In the situations when crystalline polymer materials and amorphous show substantially different enthalpies, the calculation of enthalpy may enable an

approximation of Crystallinity across a temperature range when the polymer gets heated (Gabbott. Paul, 2008).

3.7 Thermogravimetric Analysis (TGA)

3.7.1 Sample Preparation

10 mg of nanosalt and molten salts ($NaNO_3$ and KNO_3) in a covered sample were heated up from room temperature to 105℃ and kept isothermal for 10 minutes to remove the moisture. Consecutively were heated up to 900℃ with a heating rate of 20℃/min.

3.7.2 Overview of the technique

The Thermogravimetric Analysis (TGA) is an essential laboratory tool used for material characterization. TGA is used as a technique to characterize samples used in various environmental, food, pharmaceutical, and petrochemical applications.

A TGA consists of a sample pan that is supported by a precision balance. That pan resides in a furnace and is heated or cooled during the experiment. The mass of the sample is monitored during the experiment. A sample of purge gas controls the sample environment. This gas may be inert or a reactive gas that flows over the sample and exits through an exhaust A constant heating rate (so-called dynamic measurements) is applied to heat the sample and kept at a steady temperature (isothermal measurement) but can also be subject to non-linear temperature systems such as those utilized in the specimen regulated TGA (so-called SCTA) analyses. The selection of a temperature system would depend on the nature of information needed for the sample. Furthermore, the environment used in the TGA procedure plays a significant role and maybe reactive, oxidizing, or inert. Atmospheric adjustments during calculation may also be rendered. Measurements of a TGA calculation are generally shown as a TGA curve where the mass or Percent mass is plotted against temperature and/or time. Alternative and equivalent explanations are the utilization of the first derivative of the TGA curve for temperature or time. This indicates the frequency over which the mass varies and is defined as the Thermogravimetric or DTG differential graph. Mass shifts arise as a sample sheds substance in one or many separate directions or responds to the ambient environment. This induces moves in the TGA curve or the DTG curve. Thermogravimetric analysis (TGA) enables the continuous calculation of sample weight as a function of the temperature/time system both in specific atmospheres. To find the decomposition onset temperature or the loss of low molecular weight elements like a residual solvent, plasticizer, etc, only a few milligrams of a polymer specimen is heated with 10 or 20 K min^{-1} in N_2 or O_2. The TGA

coupled mass spectrometry facilitates the direct study of the specimen-driven organisms in the context of the TGA system. Specific effects can cause a sample to lose, or even gain, mass, and thus produce steps in the TGA curve. It shall contain the following (Gabbott. Paul, 2008):

- ✓ Evaporation of volatile constituents
- ✓ drying
- ✓ desorption and adsorption of gases
- ✓ moisture and other volatile substances
- ✓ Loss of water of crystallization.

Figure 3.9: Type of Thermogravimetric Analysis (TGA) used in this project

3.7.3 Interpreting TGA curves

In addition to the TGA curve, several other curves can be used for interpretation purposes:

a. The first derivative (DTG curve, rate of change of mass).
b. The DTA curve (shows exothermic or endothermic events similar to DSC); DTA curves can be interpreted in much the same way as DSC curves.
c. EGA, evolved gas analysis, online FTIR, or MS measurements of evolved gases.
d. The visual inspection of the sample after the measurement if possible using a reflected light microscope can yield qualitative information about the residue (ash-like glassy, or white or colored powder, soot particles)

e. The Effects described in the following sections show the typical shape of TGA curves, the curves are blank curve corrected.

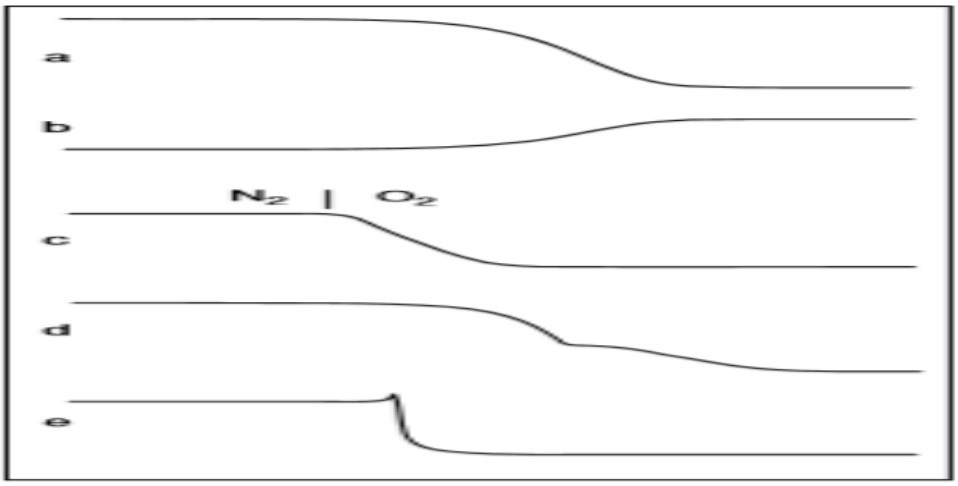

Figure 3.10: Schematic diagram of interpretation TGA curves

3.8 UV-Vis absorption spectroscopy

3.8.1 Sample preparation

The final product of silver nanowires was kept in ethanol. For UV-Vis analysis, the solution containing silver nanowires was diluted using deionized water and ethanol was used as a reference solution.

3.8.2 Description of technique

UV-visible (UV-Vis) Spectrometry is a method used to measure light absorption through ultraviolet and visible spectrum ranges. When the incident light hits the matter, it can be absorbed, reflected, or transmitted. The absorption of UV-radiation induces atomic excitation, which implies the change of state from the low energy ground to an excited state of the molecules (Gorog.S,1995). Important ultra-violet (UV) and visible (Vis) absorption spectra are produced by the absorption of electromagnetic radiation with wavelengths in the 200-400 nm (UV) and 400 to 800 nm (Vis) regions of the electromagnetic radiation. Measurements are difficult to make in the UV region with high energies and short wavelengths (100-200 nm). The UV-Vis spectra have broad features that are of limited use for sample identification but are very useful for quantitative measurements (**Agnes, 2014**).

UV-Vis spectroscopy is used to characterize the absorption, transmission, and reflectivity of different materials, such as pigments, coatings, windows, and filters. To record a UV-Vis

spectrum and, to characterize the optical or electronic properties of the material, UV-Vis spectrometry is necessarily utilized.

3.8.3 Overview of the principle technique

Considering a material with a high degree of conjugations, when light strikes on that material, it absorbs radiations in the UV-Vis region of the electromagnetic wave spectrum. Photons are transmitted when their energy is less than the band gap in contrast to those with the same or larger band gap is absorbed. Inside the polymer, molecules undertake an electronic change of levels (transitions) from lower levels to an exciting upper level. The absorption of a photon is responsible for this transaction as it makes an electron to jump from the band at lower energy to the one above with higher energy. The transaction is only possible if there is an electron in the ground state in the lower band (Agnes, 2014). The ratio of the radiation intensity transmitted by the film of thickness x (I_x) to that transmitted by a known reference (I_o) is known as the transmittance (T) of the film and is given by:

$$T=\frac{Ix}{Io} \tag{3.2}$$

The transmittance is often measured in percent (%T) because many instruments are calibrated with its very convenient scale of 0 to 100. In this case, the more useful quantity is the amount of radiation absorbed which consists of absorbance (A). This quantity is given by:

$$A=\ln\frac{Io}{Ix}=\ln\frac{1}{T} \tag{3.3}$$

$$A=-\ln T \tag{3.4}$$

The possible energy absorptions vary depending upon the nature of the bonds within a molecule. For organic molecules, one can find electrons in strong σ bonds, in weak π bonds or non-bonding, n. While absorption of energy, all of these types of electrons can jump to excited anti-bonding states which are free.

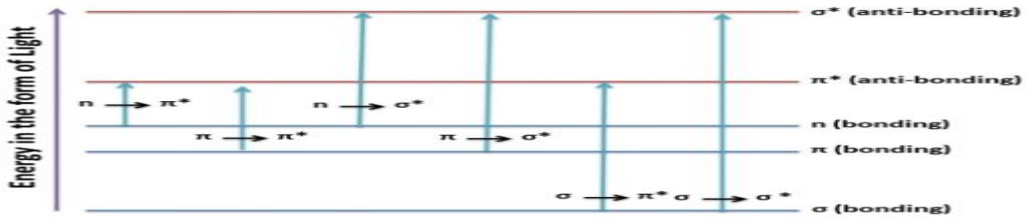

Figure 3.11: Various possible Electronic transitions in a molecule adapted from (Agnes.2014)

The diagram in figure 3.11 presents the situation where the anti-bonding states are noted with an asterisk as σ^* and π^*s.

Most $\sigma \rightarrow \sigma^*$ absorption transitions for individual bonds occur below 200 nm in the vacuum/ultraviolet region. The $\pi \rightarrow \pi^*$ and $n \rightarrow \pi^*$ absorptions occur in the near-ultraviolet/visible region. Various wavelengths of radiation are absorbed by different molecules that are present in the solution. Therefore, there are various light-absorbing, and these groups are known as chromospheres (**Agnes, 2014**).

3.9 References

Anglani, A. *et al.* (1998) *Representation and use of uncertainty in discrete event simulation models, Proceeding of the European Simulation Symposium*. DOI: 10.1007/978-1-4939-6676-9.

Associates, R. J. (1996) 'ENVIRONMENTAL SCANNING An Introduction to ESEM ®'.

Blakey, P. R., and Micklethwaite, B. (1978) *Scanning electron microscopy and X-ray microanalysis*. DOI: 10.2307/3225926.

Cheney, B. B. (no date) 'Introduction to Scanning Electron Microscopy'.

Clarke, A. R., and Eberhardt, C. N. (2002) *Microscopy techniques for materials science, Microscopy techniques for materials science*. DOI: 10.1533/9781855737501.

Egerton, R. F. (2016) *Physical Principles of Electron Microscopy, Physical Principles of Electron Microscopy*. DOI: 10.1007/978-3-319-39877-8.

L. REIMER (1998) *Scanning Electron Microscopy*.

MAGUBANE, S. S. (2018) *Metal Assisted Chemically Etched Silicon Nanowires for Application in a Hybrid Solar Cell By*.

Marturi, N. (2015) 'Vision and visual servoing for nanomanipulation and nano-characterization in scanning electron microscope. Naresh Marturi To cite this version ':, (November 2013).

Muscariello, L. *et al.* (2005) 'A critical overview of ESEM applications in the biological field', *Journal of Cellular Physiology*, 205(3), pp. 328–334. DOI: 10.1002/jcp.20444.

Stokes, D. J. (2008) *Principles and Practice of Variable Pressure/Environmental Scanning Electron Microscopy (VP-ESEM), Principles and Practice of Variable Pressure/Environmental Scanning Electron Microscopy (VP-ESEM)*. DOI: 10.1002/9780470758731.

TIEDT, L.R., W. E. P. (2002) 'An Introduction to Electron Microscopy - TEM', *Thermo Fisher Scientific*. Available at: https://www.fei.com/introduction-to-electron-microscopy/tem/.

Goldstein, Joseph. (1981) Scanning Electron Microscopy and X-Ray Microanalysis A text for

Biologist, Materials, and geologist. Doi: 10.1007/978-1-4613-3273-2

Abudayyeh, Hamza. (2012) Synthesis and Analysis of ZnO Nanowires

Zhiping Luo. (2016) A Practical Guide to Transmission Electron Microscopy. DOI: 10.5643/9781606507049

Brundle, C. R. et al. (1992) Encyclopaedia of materials characterization: surfaces, interfaces, thin films

Goodhew, Peter. et al. (2001). Electron microscopy and analysis-3rd ed.

Bendersky, Leonid. (2001) Electron diffraction using transmission electron Microscopy. Doi:10.6028/jres.106.051

Bish, DL, and Post, JE, editors. 1989. Modern Powder Diffraction. Reviews in Mineralogy, v. 20. Mineralogical Society of America.

Cullity, B. D. 1978. Elements of X-ray diffraction. 2nd ed. Addison-Wesley, Reading, Mass.

Klug, H. P, and L. E. Alexander. 1974. X-ray diffraction procedures for polycrystalline and amorphous materials. 2nd ed. Wiley, New York

Moore, D. M., and R. C. Reynolds, Jr. 1997. X-ray diffraction and the identification and analysis of clay minerals. 2nd Ed. Oxford University Press, New York.

Gabbott, P. (2008) Principles and Applications of Thermal Analysis.__DOI: 10.1002/9780470697702

Lasfargues, M. (2014) Nitrate based High-Temperature Nano-Heat-Transfer-Fluids: Formulation & Characterisation

Bacon, S. R. (2012). Interactions between latent finger marks, deposition surfaces, and development agents

Agnes Mbonyiryivuze. (2014) INDIGENOUS NATURAL DYES FOR GRÄTZEL SOLAR CELLS: SEPIA MELANIN

Görög, S.(1995) Ultraviolet-visible spectrophotometry in pharmaceutical analysis

CHAPTER FOUR

RESULTS AND DISCUSSION

In this chapter, the synthesis of silver nanowires using a polyol technique is discussed. The XRD, SEM, TEM, and UV-VIS results are analyzed. Finally, XRD, TGA, SEM, and DSC results of the mixture of molten salt ($NaNO_3$ + KNO_3) and silver nanowires (AgNWs) called nanosalt are analyzed and discussed.

4.1 SYNTHESIS OF SILVER NANOWIRES

$AgNO_3$ (≥99.8%), ethylene glycol (EG), anhydrous ethanol (EtOH, 98 %), PVP powder (mass weight of 360000,) were purchased from Sigma Aldrich Pty. Ltd. All reagents were of analytical grade and used without further purification.

For the synthesis process of Ag nanowires, the improved PVP-mediated polyol process(Zhu *et al.*, 2011) was adapted. The process is explained below in Figure 4.1: A mass of 0.6g $AgNO_3$ was dissolved in 17.0mL EG solvent, the solution is labeled S1. A mass of 1.2g of PVP is dissolved in 17.0mL EG solvent, the second solution is labeled S2. It's worth noting that each resultant solution (S1 and S2), remains colorless. The two solutions (S1 and S2) are simultaneously injected dropwise into 60.0mL of EG under magnetic stirring (120 rpm) at 160 ℃.

It was observed that the reactant mixture (S3) changed color quickly from colorless to yellow after the addition of a few drops of S1 and S2. Subsequently, S3 changed color from yellow to slightly opaque after 30 minutes which was the duration time of injection. The solution S3 was allowed to stir.

Green colloids were formed after 70 minutes of continuous stirring. However, after 75 minutes, colloids changed color to grey white colloids.

The final product was then centrifuged repeatedly to remove possible contamination (EG and excess PVP). The obtained precipitates were diluted with anhydrous ethanol (5mL), centrifuged at 3000 rpm for 30 minutes, and afterward characterized.

It should be noted that the synthesis process was repeated at 180℃ and for different aging times of 1, 3, and 6 hours. For SEM and XRD, The condensed products were dispersed on the glass substrates and dried using the oven at 80℃.

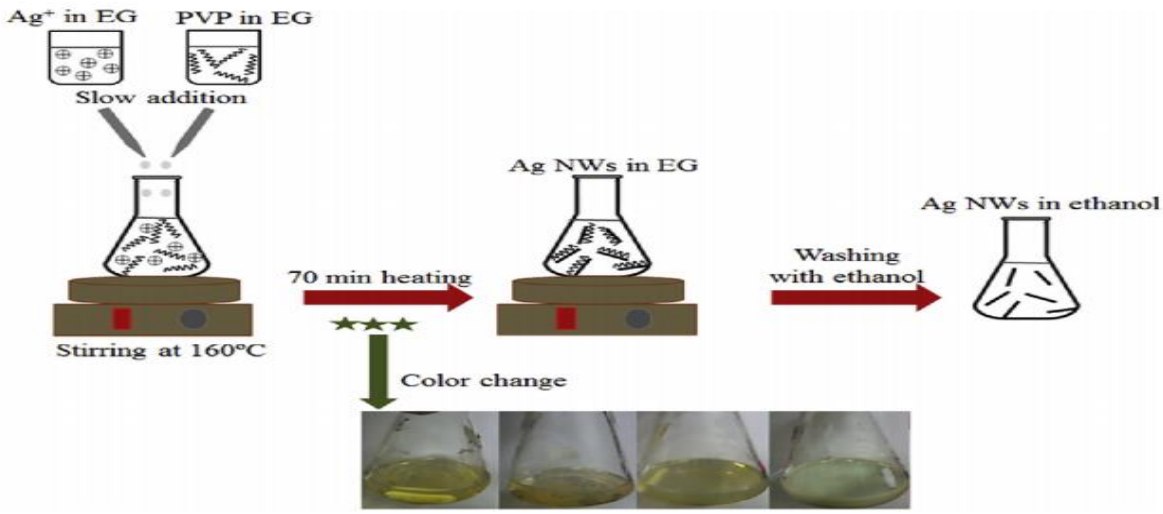

Figure 4.1: Schematic representation of the polyol synthesis of Ag nanowires (Nekahi, Marashi and Fatmesari, 2016)

4.2 Characterization techniques:

To investigate the morphology of samples, the **Scanning Electron Microscopy (SEM)** technique was performed using Carl Zeiss Auriga Field Emission Scanning Electron Microscopy (FEG SEM) imaging at 5 keV, and High-Resolution Transmission Electron Microscope (HRTEM). Before SEM/HRTEM imaging, samples were coated in carbon coater to prevent charging.

Energy Dispersive X-ray spectroscopy (EDS) of oxford instrument with X-max Solid state silicon drift detector at 20 keV was used to determine the chemical compositions.

The phase identification of samples was investigated by **X-ray Diffraction (XRD)** carried out using a Bruker Advanced D8 diffractometer with monochromatic Cu Ka radiation of 1.5406 Å.

Absorbance UV–Vis measurements were conducted on a Cary 5000 UV–Vis–NIR spectrophotometer (Varian, Inc. model DRA- 2500) between (0.3 and 2.5 μm) equipped with an integrating sphere.

Using 2.8 mg as the initial weight of samples, **Thermogravimetric analysis (TGA)** was performed on a PerkinElmer 400 over-temperature ranging from 30 ℃ to 900 ℃ at 10 ℃/min, under nitrogen atmosphere (20 mL/min).

Differential scanning Calorimetry (DSC8000, University of the Western Cape) was used for the differential scanning calorimeter analysis. The calibration procedure was performed

by using the melting temperatures and latent heat of standard certified reference materials (CRMs) (In, Zn), at a heating rate of 10K· min-1 resulting within the limits specified by the equipment manufacturer. Samples of 15-23 mg were introduced in 40µl aluminum holed crucibles using nitrogen as an inert gas in the thermal program. The samples were kept isothermally for 10 minutes at 80ºC. Then they were heated up from 80ºC to 350ºC at 10K/min, keeping this temperature for 10 min. and cooling down to the initial temperature maintaining the heating rate and isothermal times. A low scanning rate was applied to record the heat flow curve as a function of temperature. Specific heat capacity tests were also performed

4.2.1 Morphology and chemical composition: FE-SEM and EDS

a. Morphology: FE-SEM

Figure 4.2-4.4 shows field-emission scanning electron microscope (FE-SEM) images of nano-silver particles (nAgPs) synthesized at different times (i.e. 1h, 3h, and, 6h) and temperatures of 160 ℃ and 180 ℃. Specifically, **Fig. 4.2(a)** is the FE-SEM image of samples synthesized for 1 hour at 160℃. As can be seen, there is a mixture of nanoparticles and nanowires (designated by white arrows). The nanowires are composed of cubic and tetrahedral shapes. At such time of injection, the formations of nanowires are not fully complete. This is evidenced by the predominant distribution of nanoparticles in the sample. The histogram of particle size distribution is shown in **Fig.4.2 (b)**. The average particle size is estimated for the predominant nanoparticles is 406 nm.

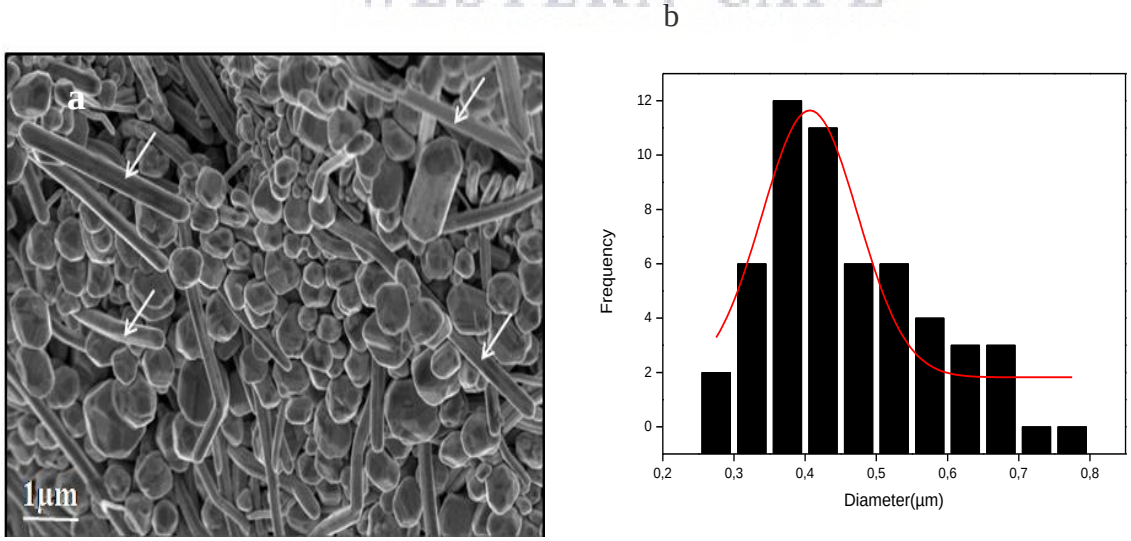

Figure 4.2: (a) SEM micrographs of silver nanowires synthesized for 1 hour at 160 ℃, the histogram of the particle size distribution of **(b) nanoparticles**

Figure 4.3(a) is **an** FE-SEM image for samples synthesized for 3 hours at 160 ℃. Nanowires of different dimensions are observed dominating in this sample. It implies that the formation of nanowires is almost near completion giving a higher yield with an average particle size of 132 nm. The histogram of the particle size distribution is shown in **Fig. 4.3(b)**.

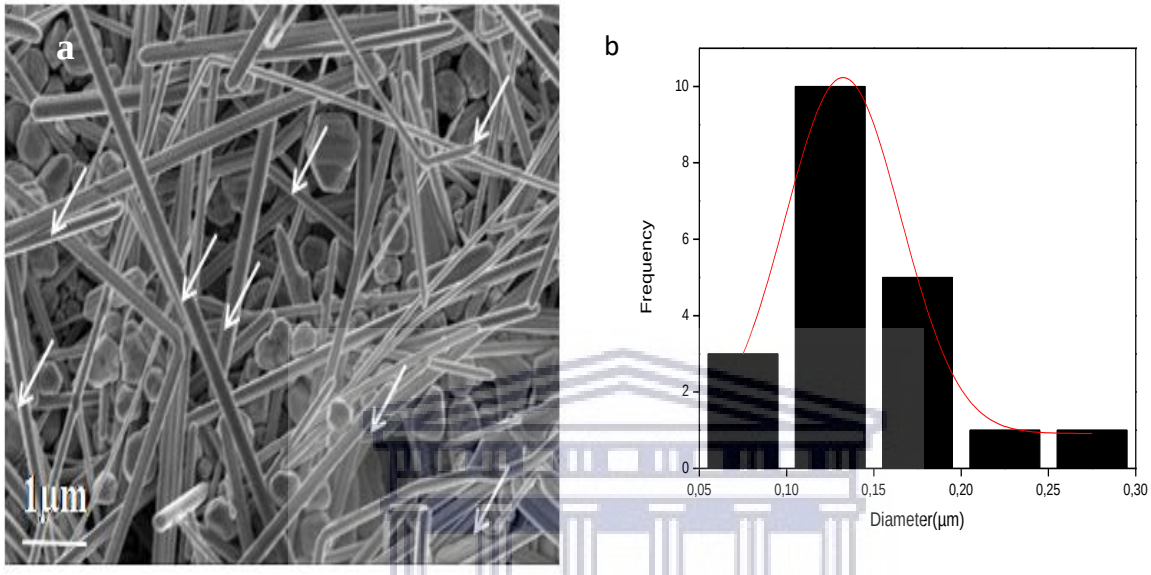

Figure 4.3: (a) FE-SEM image of silver nanowires synthesized for 3 hours at 160 ◦C, the histogram of the particle size distribution of **(b)**

Figure 4.4 shows the FE-SEM image of samples synthesized for 6 hours at 180 ℃. As can be seen, the sample is composed mainly of nanowires. The aspect of the final product could be justified by the effect of PVP, which played an important role in the polyol process by its function as a stabilizer agent and, by controlling the growth and form of the nAgPs (Mao, Feng, and Ma, 2012) PVP with a long macromolecule chain can be used to achieve a strong aspect ratio AgNWs (e.g. MW= 360 000) (Khamliche *et al.*, 2018). Also, long hours of synthesis and temperature could have an impact on the aspect and size of the nanowires. (Coskun, Aksoy and Unalan, 2011) investigated an extensive parametric study on the polyol synthesis of silver nanowires. Their studies showed that, below a critical temperature, high aspect ratio Ag nanowires synthesis is not possible. High temperatures are also crucial for the conversion of ethylene glycol to glycolaldehyde, which reduces Ag+ ions to Ag atoms. The average size of the diameter was found to be 158 nm. The histogram of particle size distribution is shown in **Fig.4.4 (b).**

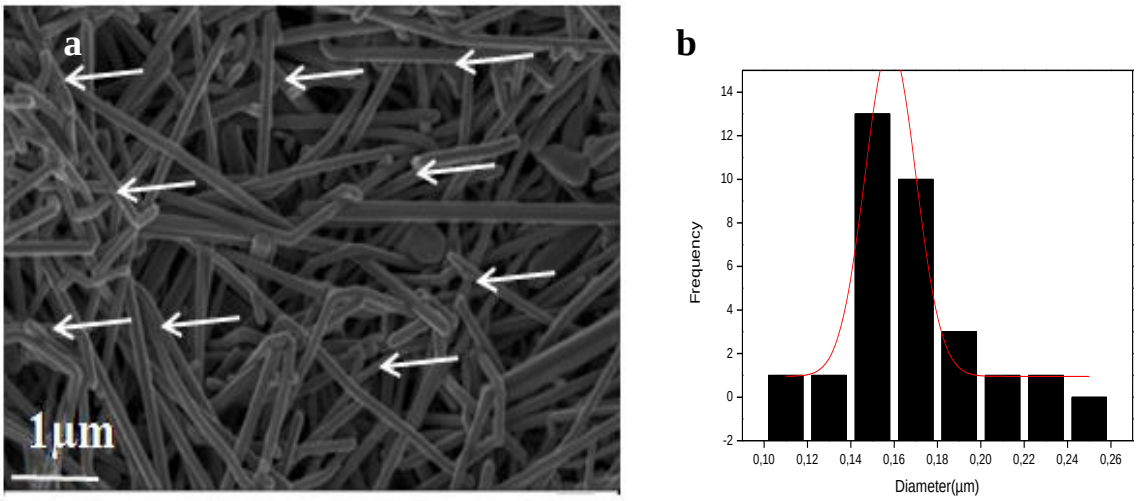

Figure 4.4: (a) FE-SEM image of silver nanowires synthesized for 6 hours at 180 ◦C, the histogram of the particle size distribution of **(b)**

b. Energy Dispersive X-ray spectroscopy

Figure 4.5, 4.6, 4.7 is the EDS spectra showing the elemental chemical compositions in the samples synthesized for 1 hour, 3 hours at 160 ℃, and 6 hours at 180 ℃ respectively. The spectra reveal Ag as the main element on all samples. The appearance of Si and C signal is due respectively to contamination during preparation or drying process and carbon coating the sample before SEM analysis.

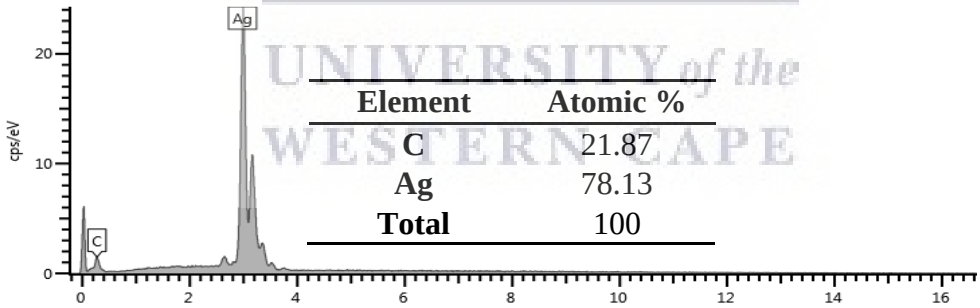

Element	Atomic %
C	21.87
Ag	78.13
Total	100

Figure 4.5: EDS Spectrum of silver nanoparticles synthesized for 1 hour at 160 ℃, inset shows the chemical element with a respective weight percentage

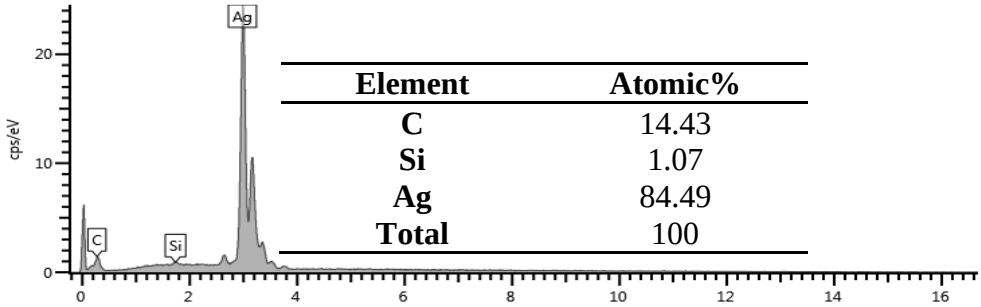

Element	Atomic%
C	14.43
Si	1.07
Ag	84.49
Total	100

Figure 4.6: EDS Spectrum of silver nanowires synthesized for 3 hours at 160 ◦C, inset shows the chemical element with a respective weight percentage

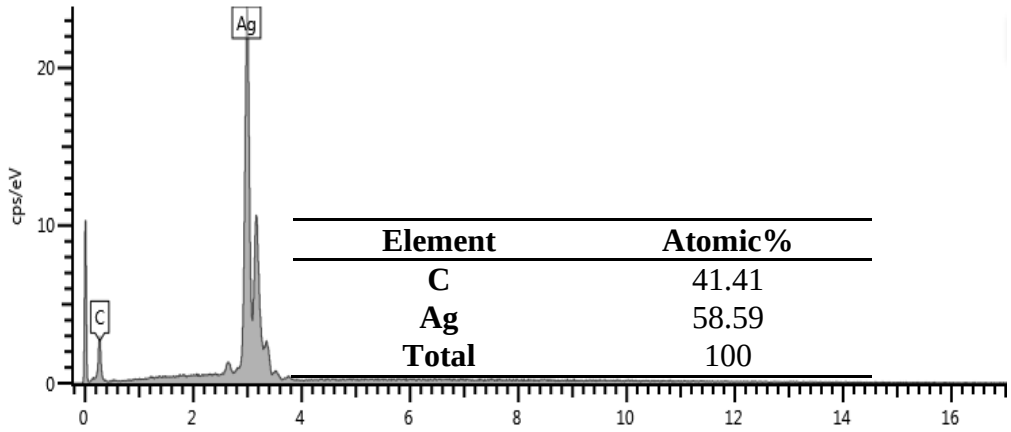

Element	Atomic%
C	41.41
Ag	58.59
Total	100

Figure 4.7: EDS Spectrum of silver nanowires synthesized for 6 hours at 180 ◦C, inset shows the chemical element with a respective weight percentage

4.2.2 Transmission Electron Microscope (TEM) of nAgPs

High-Resolution Transmission Electron Microscope (HRTEM) images of samples synthesized for 1 hour at 160 ℃**,** 3 hours at 160 ℃, and 6 hours at 180 ℃ respectively are shown in **Figure 4.8-4.10**. The HRTEM image for samples synthesized for 1 hour **(See Fig4. 8(a))** shows the presence of both nanoparticles and nanowires. These observations confirmed SEM images previously discussed. The SAED image shown in **Fig.4.8 (b)** corresponds to samples synthesized for 1 hour at 160 ℃ showing scattered diffraction spots with each spot making up a ring.

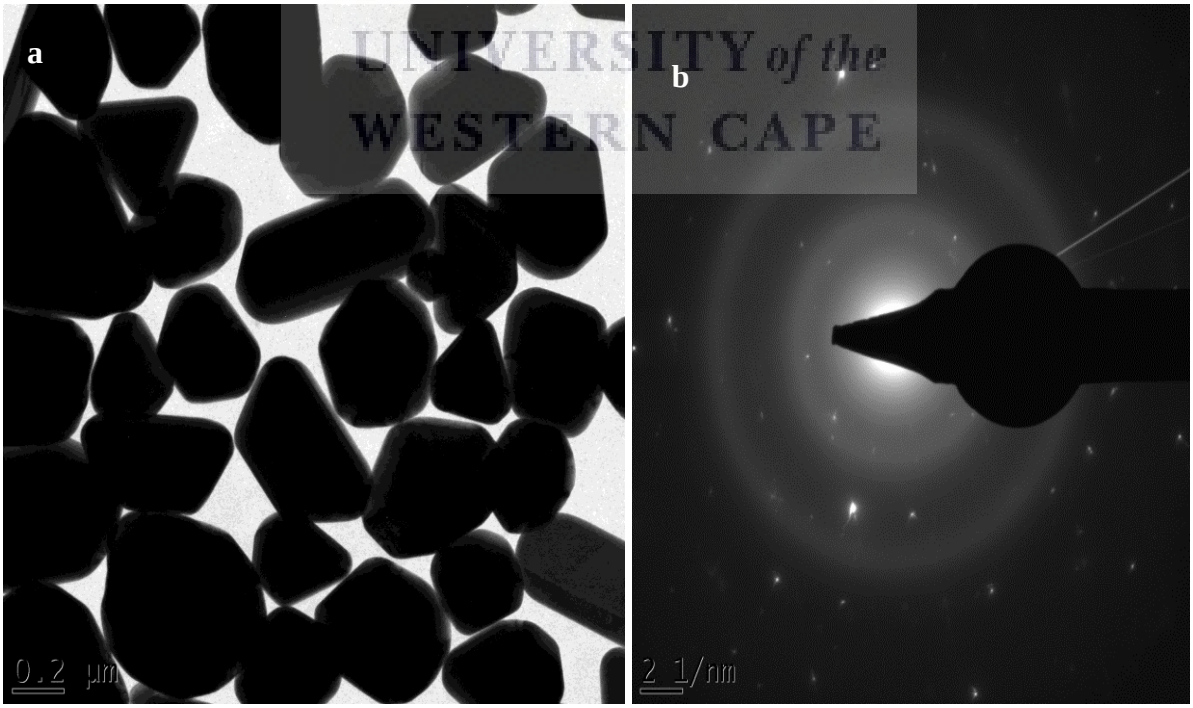

Figure 4.8: (a) HRTEM image of silver nanowires synthesized for 1 hour at 160 ℃**,** (b) SAED image

For samples synthesized for 3 hours at 160 ℃ **(see Fig.4.9 (a))**, HRTEM images reveal nanoparticles and nanowires of different dimensions.

The singular nanograin is seen in **Fig.4.9 (b)** is composed of distinguishable planes with appropriate d_{hkl} distances of 0.28, 0.24, 0.25 nm. It's corresponding SAED image shown in **Fig.4.9(c)** reveal bright diffraction spots with each spot arising from Bragg reflection of an individual crystallite.

Figure 4.9: (a) HRTEM results of silver nanowires synthesized for 3 hours at 160 ℃, (b) singular nanograin showing the planes, (c) corresponding SADE image.

Figure 4.10 (a) shows the HRTEM images of samples synthesized for 6 hours at 180℃ revealing the presence of nanowires. The average diameter of the nanowires synthesized after 6 h was approximately 129 nm with a length of 16μm. The histogram of particle distribution is illustrated in **Fig. 4.10(b)**.

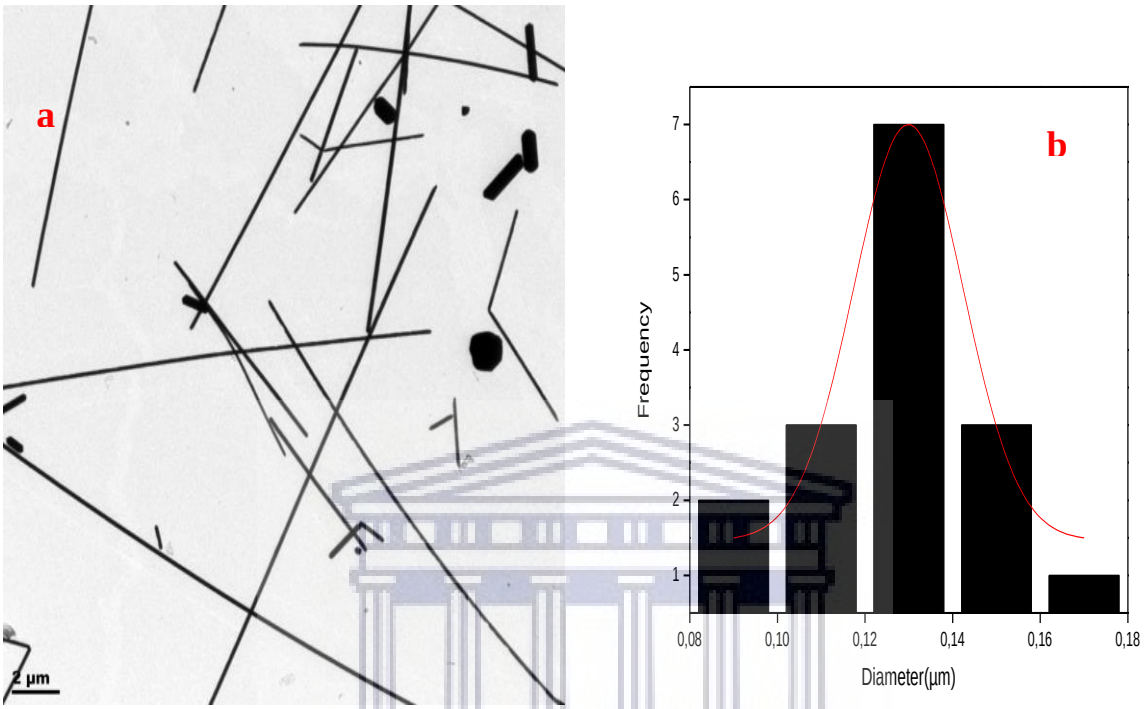

Figure 4.10: HRTEM results of silver nanowires synthesized for 6 hours at 180℃, (b) histogram of the particle size distribution for samples synthesized for 6 hours at 180℃

4.2.3 X-Ray Diffraction (XRD)

Figure 4.11 shows the XRD pattern of images of samples synthesized for 1 hour, 3 hours at 160℃, and 6 hours at 180℃. The XRD pattern shows that silver nanowires synthesized using the polyol process method are entirely in the face-centred cube (FCC) phase. The lattice constant calculated from this XRD pattern was 4.088Å, which is perfectly in agreement with the literature value of 4.086Å (Tang, He and Wang, 2014). It is important noting that the calculated ratio of diffraction intensity between the (111) and (200) planes of the 3 samples (1h, 3h, and 6h) changed from 2.29, 3.33 to 4 respectively, showing an increasing degree of preferential growth and/or orientation along (111) of a different time and, possibly because of the higher yields of the nanowires in the final products (Xia *et al.*, 2009; Khamliche *et al.*, 2018). The XRD pattern shows no other peaks due to crystallographic impurities in the three samples. The intensity of the peak at 38.28°(111) is much dominant than of the other peaks at 44.32°,64.44°,77.4°and 81.56° revealing that the

synthesized of nAgPs have preferred (111) orientation for all the samples (Khamliche *et al.*, 2018).

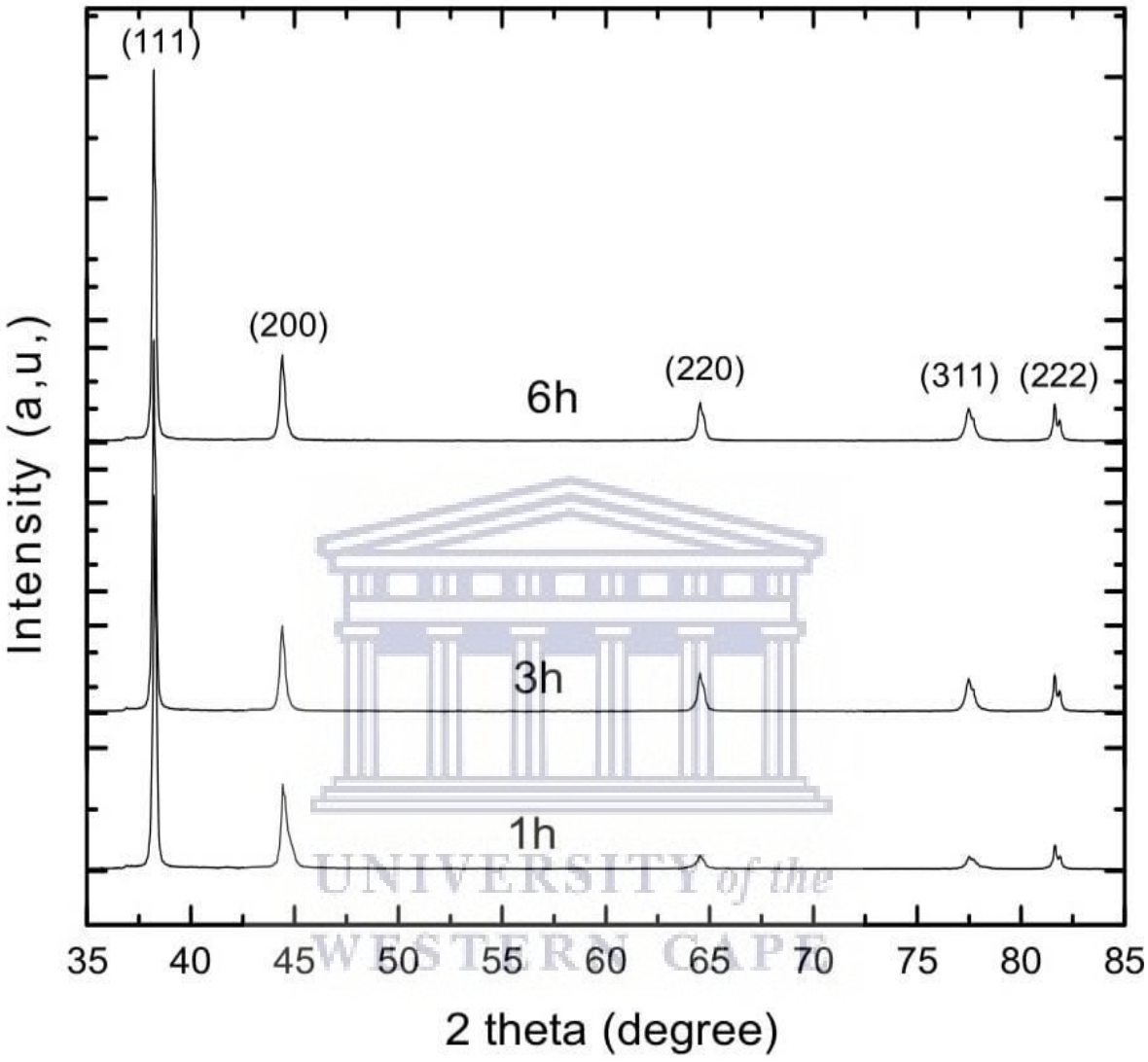

Figure 4.11: X-ray diffraction of the synthesized silver nanowires at different times and temperatures.

4.2.4 Optical analysis: UV–Vis spectroscopy

The UV-Vis absorption spectra of the product in the aqueous solution were also obtained to see the effect of the temperatures and time on the final product. The UV-Vis absorbance spectra for samples synthesized for 1 hour (what is the temperature), 3 hours at 160 ℃, and 6 hours at 180 ℃ are shown in **Fig.4.12.** The spectra show broad and shape absorption peaks at a different wavelength. Precisely, samples synthesized for 1 hour reveal a broad absorbance peak at 445 nm, while samples for 3 hours at 160 ℃ show absorption at 405 nm. The

appearance of peaks confirms the surface Plasmon resonance of Ag nanoparticles (Kottmann *et al.*, 2001; Mao, Feng, and Ma, 2012). As can be seen, samples synthesized for 6 hours at 180 ℃ exhibit two distinct absorbance peaks at 350 and 400 nm which should be attributed to the out-of-plane quadrupole resonance and out-of-plane dipole resonance of the Ag nanowires(Chen and Carroll, 2002). After 6h, the absorption peak could be observed around 400 nm, indicating that there are almost only Ag nanowires in the final product.

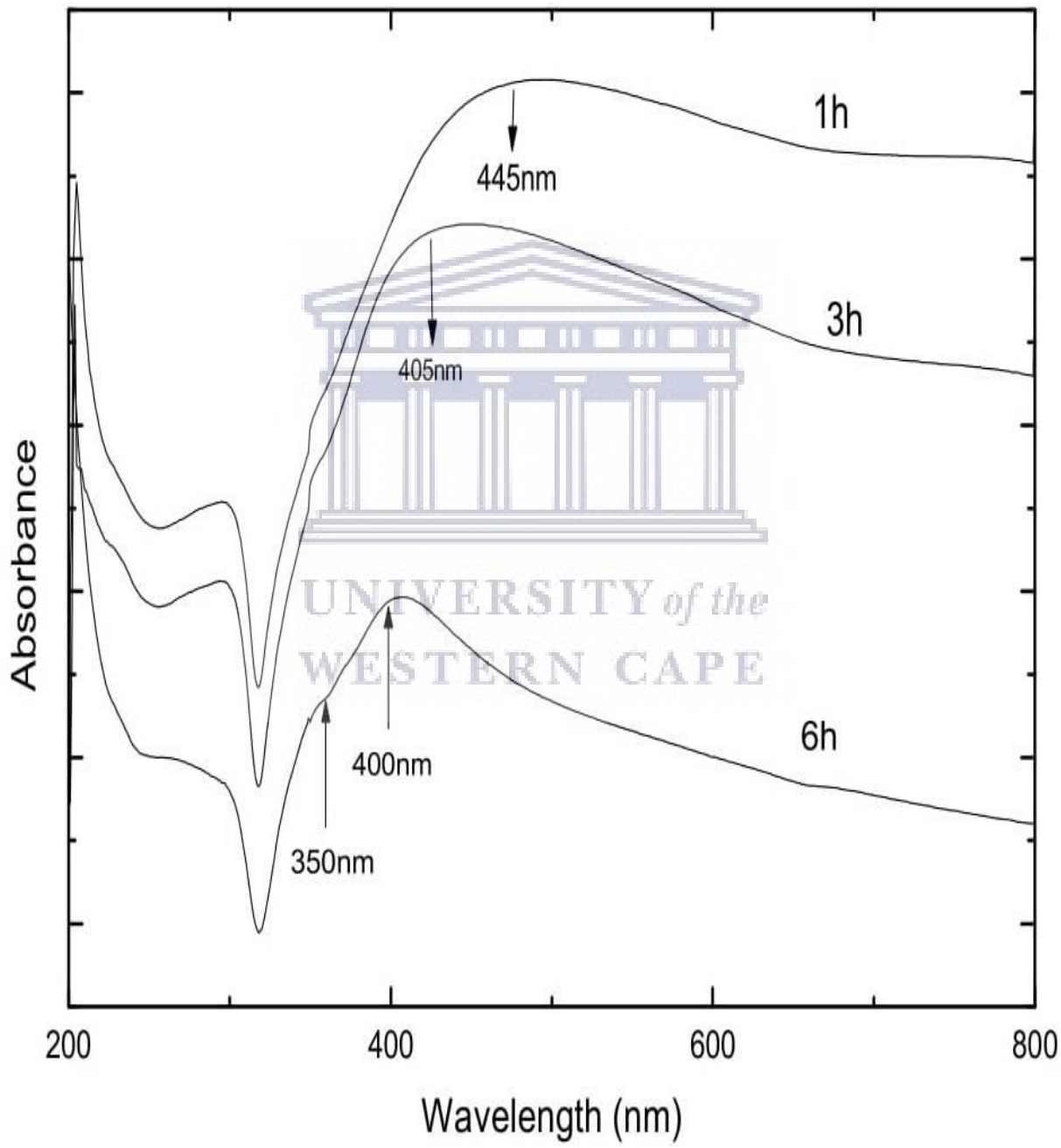

Figure 4.12: UV-Vis absorption Spectra of silver nanoparticles and nanowires synthesized for 1 hour 160 ℃, 3 hours at 160℃, and 6 hours at 180 ℃.

4.2.5 Summary

Silver nanowires with high yields have been synthesized by using a simple and improved PVP-mediated polyol process through adjusting the temperature. It could be observed that time and temperatures play an important role in the aspect and growth of the silver nanoparticles or nanowires. Under a given temperature, a high aspect ratio of Ag nanowires formation is not possible. As the temperature and time increase, anisotropic growth becomes favorable. Good silver nanowires growth temperature and time for the polyol synthesis was found to be 180℃ after 6h. For further analysis in the project, silver nanowires synthesized after 6h will be used because they displayed better results compared to 1 hour and 3 hours.

4.3 Thermophysical properties of the mixture molten salt ($NaNO_3$ +KNO_3) and silver nanowires (AgNWs).

Sodium nitrate ($NaNO_3$, 99.8%), and potassium nitrate (KNO_3, 98 %) were purchased from Sigma Aldrich Pty. Ltd. All reagents were of analytical grade and used without further purification.

In this section, the mixture of molten salt ($NaNO_3$ +KNO_3) and silver nanowires (AgNWs) will be called nanosalt. Thermophysical properties of the nanosalt, including melting point, specific heat, and thermal conductivity will be investigated. The nanosalt were prepared based on a liquid solution method (Kenisarin, 2010), and the main procedure is shown in **Figure. 4.13**.

Initially, binary nitrate solar salt ($NaNO_3$ + KNO_3 with 60:40 molar ratios, respectively) was used as the base material. Ethanol was evaporated from silver nanowires (AgNWs); only the condensed precipitate was weighted. The liquid solution method was used to prepare the nanosalt samples by firstly mixing deionized water, binary solar salt, and AgNWs (at different percentages 1 wt%, 2 wt%, 3 wt %).

Secondly, the sample was sonicated for 120 min in an ultra sonicator; to ensure good dispersion of AgNWs and proper mixing of the sample. Finally, water was evaporated from the sample by a hot plate at 100°C for 5 hours to obtain the nanosalt without moisture. To avoid the effect of moisture, the samples were heated again before the DSC measurements.

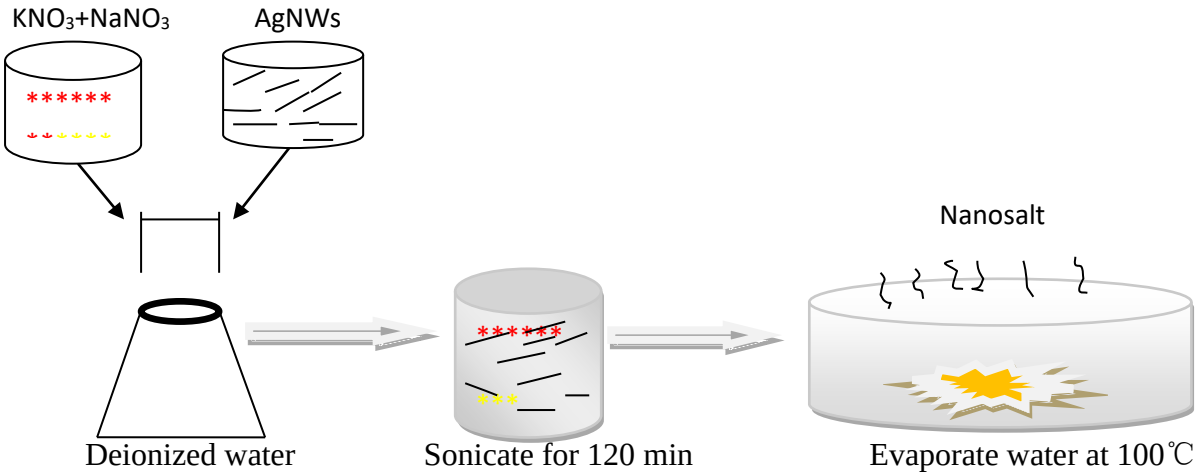

Figure 4.13: Schematic procedure to prepare nanosalt samples

4.3.1 Differential Scanning Calorimetry (DSC)

DSC plots of binary salt and, nanosalt (with different concentrations of AgNWs, e.g.1 wt%, 2 wt% and, 3 wt%), as well as the latent heat of fusion, melting point, were recorded. **Figure 4.14** shows the heat flow of the binary salt and nanosalt. The melting point of the binary and nanosalt were found to be 221℃, which is also similar to the literature result of 222 °C (Nazir *et al.*, 2019). It could be noticed that AgNWs have an impact on the latent heat of fusion. **Table 4.1** shows the result of the latent heat of fusion of the binary salt with nanosalt.

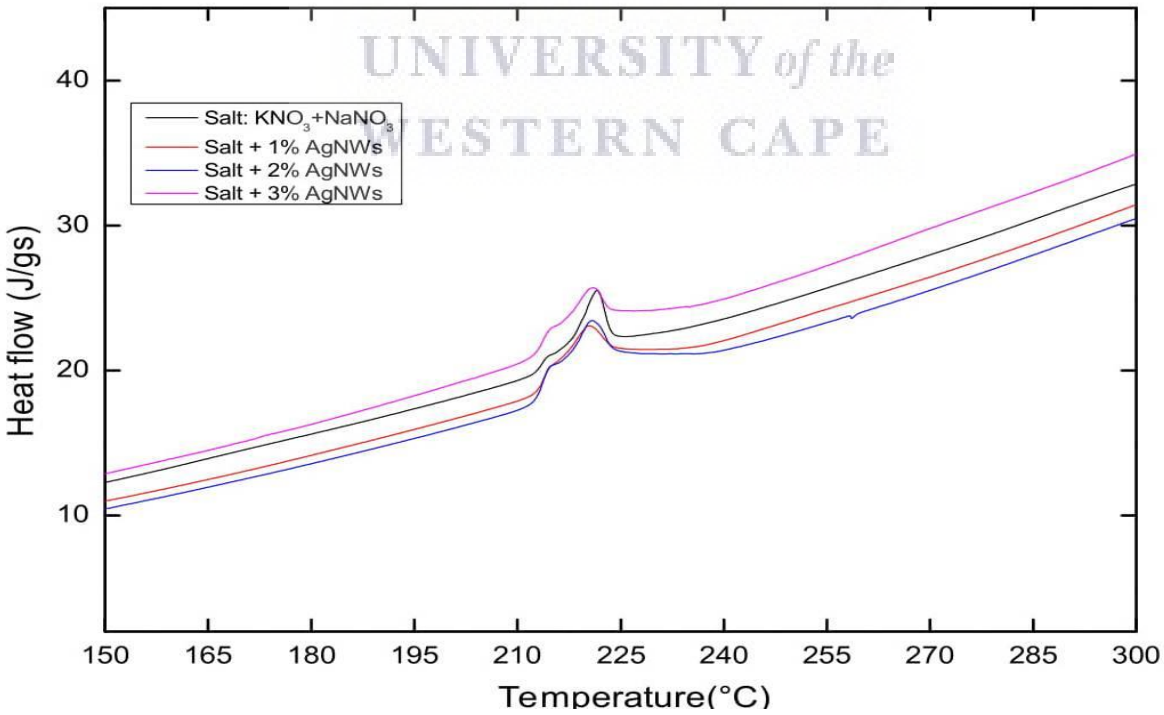

Figure 4.14: Heat flow Vs Temperature of binary salt and nanosalt

Table 4.1 Latent heat of fusion, melting temperature, and onset temperature of $NaNO_3$-KNO_3 (60:40) mixture and nanosalt obtained with different percentages of AgNWs

Material	AgNWs concentration (w%)	Latent heat of fusion(J/g)	Onset temperature (℃)	Melting temperature (℃)
Binary salt	—	109.8895	217.19	221.52
Nanosalt	1	130.4681	212.72	220.27
Nanosalt	2	121.0671	212.53	220.72
Nanosalt	3	118.8557	212.49	220.63

The latent heat of fusion of the binary salt without any additives was found to be 109℃ the value is approximately similar to the literature result which is 100℃ (Mohamed *et al.*, 2017). It could also be observed that the presence of AgNWs in the binary salt helps the material to absorb more heat because; a high value for the latent heat of fusion corresponds to high thermal storage capacity. Binary salt with 1% of AgNWs showed an improvement of latent heat of fusion about 19%, where, nanosalt having 2 wt% and 3 wt% showed also an improvement of 11% and 8% respectively. The effect for all the three concentrations investigated revealed that the increase in latent heat with 1 wt% was more evident. Therefore, nanosalt with 2 wt% and 3 wt% showed a decrease in latent heat of fusion compared to nanosalt with 1% of AgNWs. Furthermore, the increase in latent heat of nanosalt sample could be explained by the fact that AgNWs agglomerated on the sample and this required less onset temperature to melt the sample compared to the binary salt without any additive.

4.3.2 Thermo-Gravimetric Analysis (TGA)

As can be observed in the figure, solar salt and nanosalt present a similar decomposition curve. All measured samples have a maximum mass loss below 0.1% for 560°C (maximum working temperature of solar salt) and below 6% for 600 °C, showing the stability of the salt-based nanosalt at high-temperature conditions.

The decomposition of this nitrate salt mixture and the nanosalt showed that between 600 ℃ and 650 °C, the degradation was around (6.5% mass loss, **Fig. 4.15**).

After 650 ℃, rapid degradation of the mixture salt, and the nanosalt could be observed where the total loss was found around 70% for all the samples.

Gradual settling of the weight occurred above 750 °C suggesting that a solid stable compound was produced. With a nitrogen atmosphere used to prevent oxidation, most of the mass loss will have been through the release of nitrogen and oxygen gas, the solid mass left in the crucible will probably be a blend of potassium and sodium oxide (Lasfargues, 2014).

The chemical transitions occurring during the decomposition of this salt will be the following (Lasfargues, 2014):

* **$NaNO_3$ (l) ↔ $NaNO_2$ (l) + $_{1/2}O_2$ (g)** this pseudo-equilibrium occurred

Above 550°C

* **$2NaNO_2$ (l) → Na_2O(s) + N_2 (g) + 3/2O2 (g)**

As temperature rose, the nitrite further decomposed producing nitrogen gas and sodium oxide.

* In a similar manner to **$NaNO_3$, KNO_3 (l) ↔ KNO_2 (l) + $1/2O_2$ (g)** goes into a pseudo-equilibrium above 550 °C

$2KNO_2$ (l) → K_2O + N_2 + $3/2O_2$ (g) Decomposition led to the production of oxides which explained why the mass settled at 25%, as a blend of both potassium and sodium oxides were produced. The flow of nitrogen through the furnace would have pushed the equilibrium toward the production of nitrite by removing any gas created.

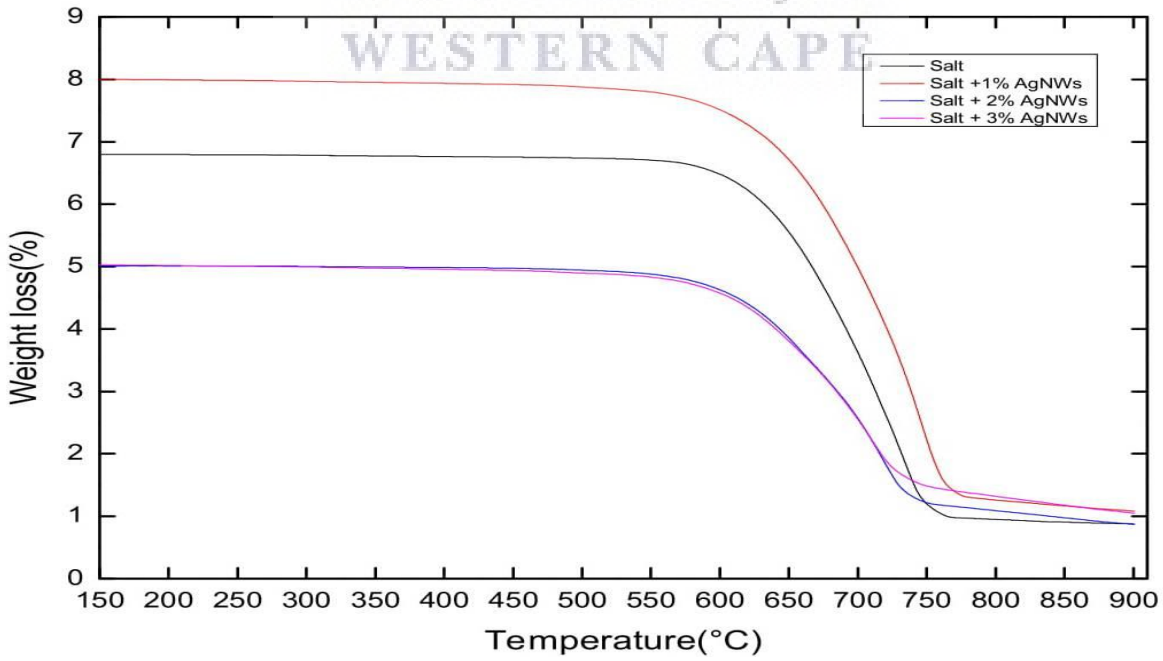

Figure 4.15: Thermal gravimetric Analysis (TGA) curves of weight loss Vs Temperature.

4.3.3 X-Ray Diffraction (XRD)

The XRD pattern in **figure 4.16** shows that after 3 thermal cycles, the sample containing salt and silver nanowires was stable this was to confirm the stability of the nanosalt compare to the TGA results. The XRD pattern also confirms the presence of sodium nitrate, potassium nitrate, and silver showing an increasing degree of preferential orientation along (104) due to the high concentration of sodium nitrate in the mixture. The XRD pattern shows no other peaks due to crystallographic impurities in the sample. The intensity of the peak at 29.38°(104) is much dominant than of the other peaks at 23.51°,29.42°,38.11° of potassium nitrate and silver nanowires revealing respectively the high amount of sodium nitrate, potassium nitrate, and silver nanowires in the sample.

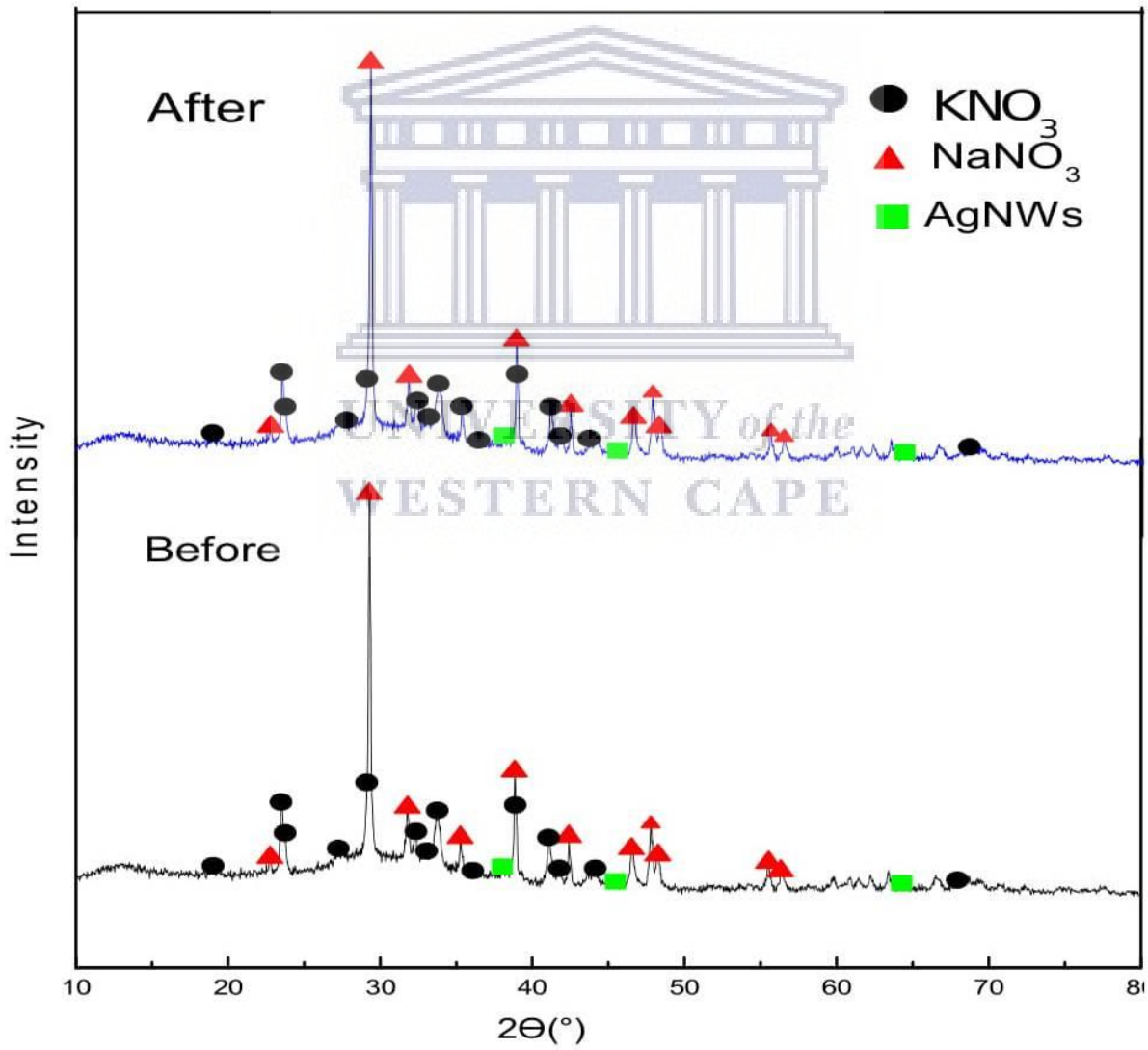

Figure 4.16: XRD patterns of molten salt and silver nanowires before and after thermal cycles.

4.3.4 Specific heat capacity of molten salt $NaNO_3$- KNO_3 (60:40) mixture and nanosalt obtained with different concentrations of AgNWs

Differential Scanning Calorimetry (DSC) was used to measure the Cp of the molten salt and nanosalt. The tracking heat flow of the sample against the heat flow of the reference is used in the DSC device to calculate the Cp. Sapphire was used as a standard material with known specific heat capacity values in the range of temperatures of the experiments which needed to run a blank crucible, and the mixture sample (salt and nanosalt) to find the Cp of the sample. According to eq. (4.1), STARe software is used for the Cp calculation of the sample (Awad *et al.*, 2018).

$$Cp_{sample}=Cp_{sapphire} \times \frac{Weight_{sapphire}}{Heat\ flow_{sapphire}} \times \frac{Heat\ flow_{sample}}{Weight_{sample}} \quad (4.1)$$

Each sample runs three times in an aluminum crucible to verify the repeatability of the measurement.

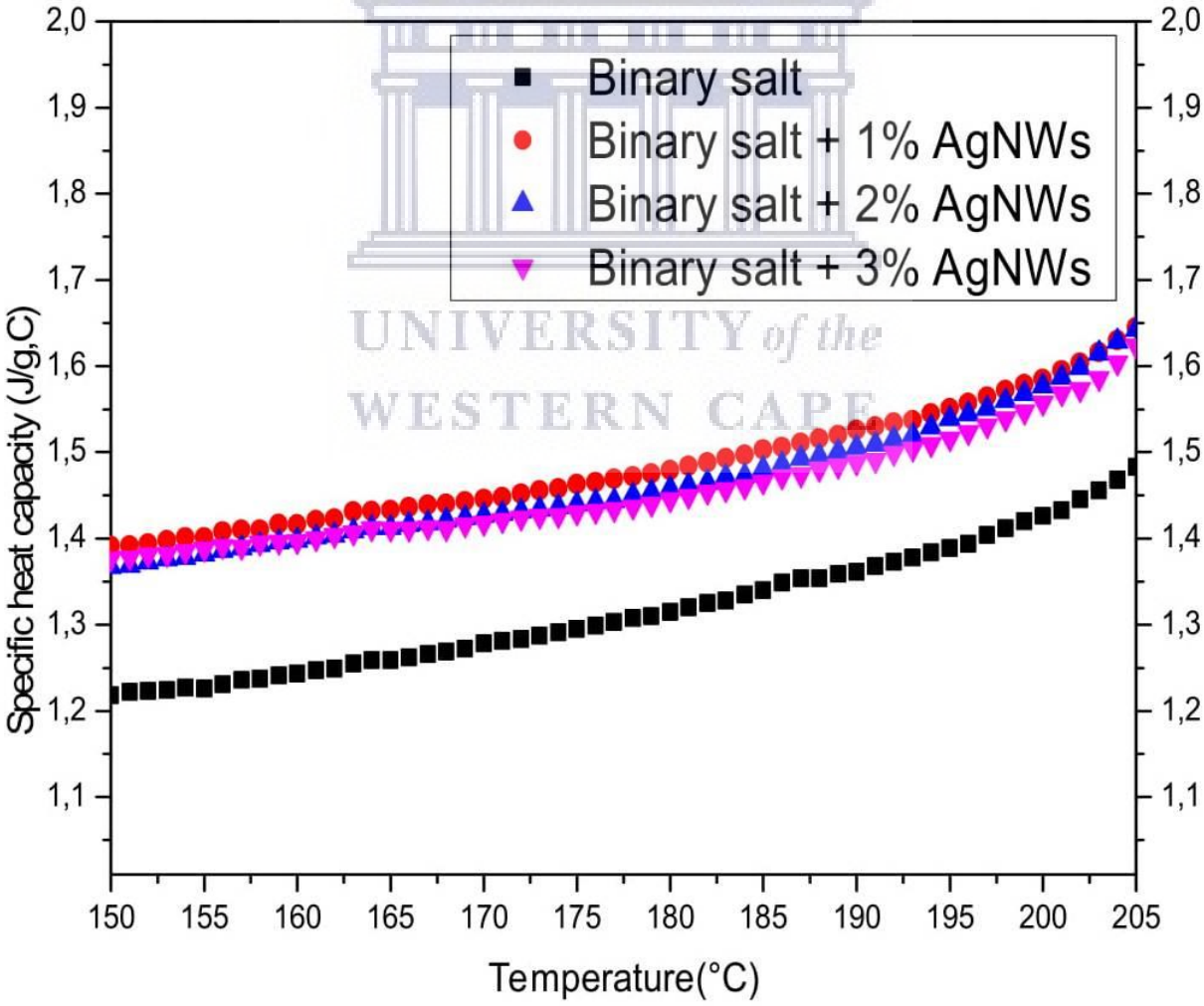

Figure 4.17: Specific heat capacity of the solid phase of binary salt and nanosalt with different concentrations of silver nanowires.

It has been reported that additives particles on the solar salt play an important role in the specific heat which either increases or decreases. Extensive work has been done in that regard, for that, nanoparticles have been reported to produce an effect on the specific heat. The addition of different concentrations of silver nanowires also produced an effect on the heat capacity of solar salt and nanosalt both in solid and liquid phases. The graphs related to the specific heat capacity of solar salt and nanosalt versus temperature are plotted in **Fig. 4.17** (in the solid phase) and in **Fig. 4.18** (in the liquid phase).

The specific heats were calculated by recording the average of 3 different values in the temperature range of 150 °C to 205 °C in the solid phase and from 245 °C to 255 °C (255 °C where the reaction ends) in the liquid phase. **Table 4.2** shows the specific heat capacity (Cp) of the solid phase of binary salt and nanosalt with different concentrations of silver nanowires after 3 runs measurements. It could be observed that the average specific heat of the binary salt in the solid phase is 1.49J/g·°C which is in perfect agreement with the literature value reported from different researchers with an average value of 1.45 to 1.55 J /g. °C (Andreu-Cabedo *et al.*, 2014; Chieruzzi *et al.*, 2017)**.** It could be seen that in **table 4.2** the addition of silver nanowires to the base salt has increased the Cp both in the solid and liquid phase.

The higher increase of Cp was obtained in the solid phase; revealing that a high C_P value was observed with 1 wt% AgNWs corresponding to the value of 1.66J/g.°C. The specific heat capacity of the salt with AgNWs at low concentrations (up to 1 wt %) was higher compared to that of the base salt. Increasing the concentration of AgNWs (i.e., 2.0wt% and above), however, leads to a slight decrease in specific heat capacity.

Fig.4.18 shows the specific heat capacity of the liquid phase of binary salt and nanosalt with different concentrations of silver nanowires. The specific heats, in this case, were calculated by recording the average of 3 different values.

Table 4.3 shows different values after 3 runs of binary salt and nanosalt. It could be noticed that the average specific heat of the binary salt in the liquid phase is 1.47J/g.°C. However, nanosalt showed a relative increase in the Cp value at low concentrations (up to 1.0wt %) like in the solid phase but with a lower increase compared to Cp in the solid phase.

The results are in perfect agreement with one suggesting that specific heat capacity is enhanced at low nanoparticles concentrations and reduced at high concentrations(Hu *et al.*, 2019). This result is also verified in the case of nanowires that the high concentration of AgNWs in the base salt reduced the specific heat capacity compared to the 1 wt%. Specific

heat capacity improvement could be explained by the related high surface area of nanoparticles by unit volume.

The nanoparticles diameter could also play an important role as smaller nanoparticles provide a larger solid/liquid interface area which increases interfacial impacts in their corresponding suspensions (Chieruzzi *et al.*, 2015).

The theory could also be adapted in the case of nanowires suggesting that the increase in the specific heat capacity could be attributed to related high surface area of nanowires which could lead to a larger solid/liquid area increasing the interfacial impact in their suspensions.

Table 4.2: Specific heat capacity of the solid phase of binary salt and nanosalt

Run	Binary salt	AgNWs		
	–	1 wt%	2 wt%	3 wt%
Run1	1.50	1.65	1.64	1.61
Run2	1.49	1.66	1.67	1.64
Run3	1.48	1.67	1.63	1.65
Average	**1.49**	**1.66**	**1.65**	**1.63**
% increase	—	**11.41%**	**10.74 %**	**9.39%**

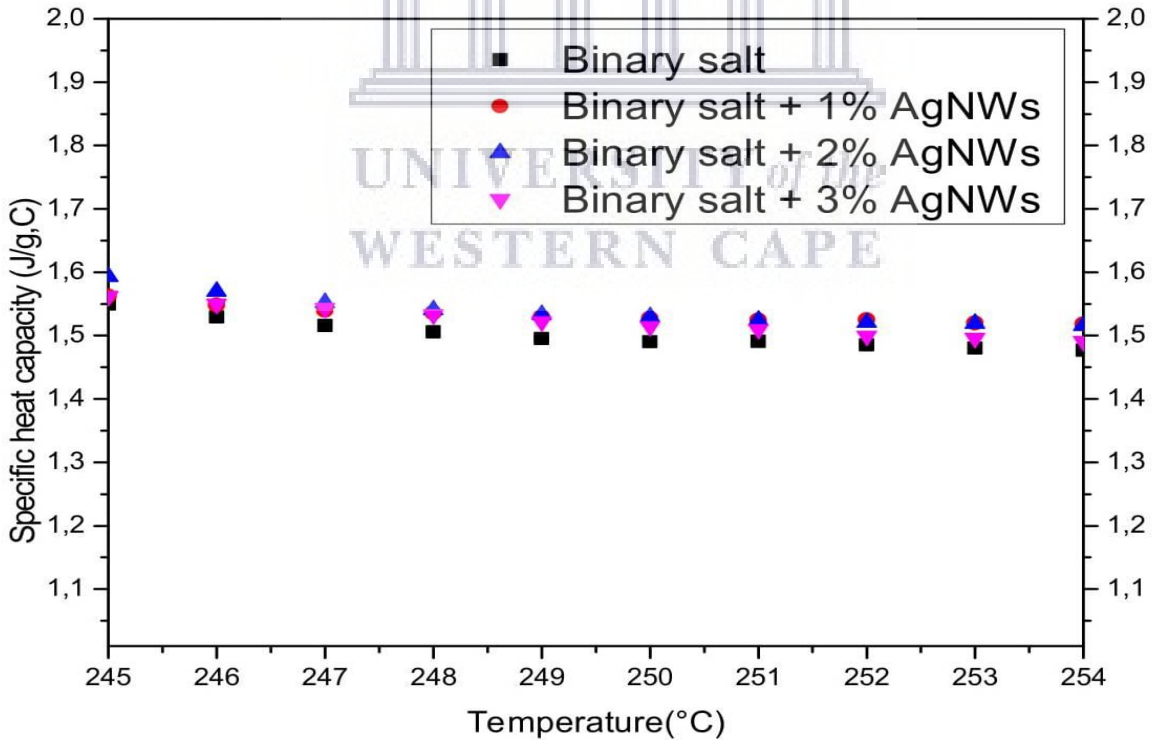

Figure 4.18: Specific heat capacity of the liquid phase of binary salt and nanosalt with different concentration of silver nanowires

Table 4.3: Specific heat capacity of the liquid phase of binary salt and nanosalt with different concentration of silver nanowires after 3 runs

Run	Binary salt	AgNWs		
	—	1 wt%	2 wt%	3 wt%
Run 1	1.46	1.52	1.51	1.49
Run 2	1.48	1.53	1.49	1.48
Run 3	1.48	1.51	1.52	1.50
Average	**1.47**	**1.52**	**1.51**	**1.49**
% Increase	**—**	**3.40%**	**2.72%**	**1.36%**

4.3.5 Morphology and chemical composition: FE-SEM and EDS

a. Morphology: FE-SEM

Fig.4.19 shows SEM micrographs of binary salt and nanosalt with different concentrations of AgNWs. The addition of silver nanowires (AgNWs) into the binary salt ($NaNO_3$-KNO_3) showed a positive effect on the latent heat energy and specific heat.

To further investigate the improvement in specific heat capacity, SEM was employed to examine the morphology of pure and nanosalt samples. It could be observed that the addition of 1 wt% of, 2 wt%, and 3 wt% of AgNWs in the binary salt **figure 4.19 (a), b, and c** respectively increased the specific heat capacity; nanowires could be identified on the binary salt by the red arrows.

The presence of nanoparticles is also observed in the samples explaining that, those particles played an important role in the Cp enhancement. Upon further addition of nanowires, the amount of these small nanostructures is reduced, while some agglomeration appears this could explain in **(Fig.4.19(c) and (b)** possibly as a result of the reduced homogeneity then reduces the Cp. (Chieruzzi *et al.*, 2017) concluded that the specific heat capacity improvement of nanofluids is associated with the high specific surface area of nanoparticles (i.e. the total surface area of a material per unit of mass). Good nanoparticles dispersion or nanowires could explain the high surface area. In these cases, the interactions between the salts ion and the nanoparticles or nanowires surface are responsible for the specific heat enhancement (Dudda and Shin, 2013; Chieruzzi *et al.*, 2017).

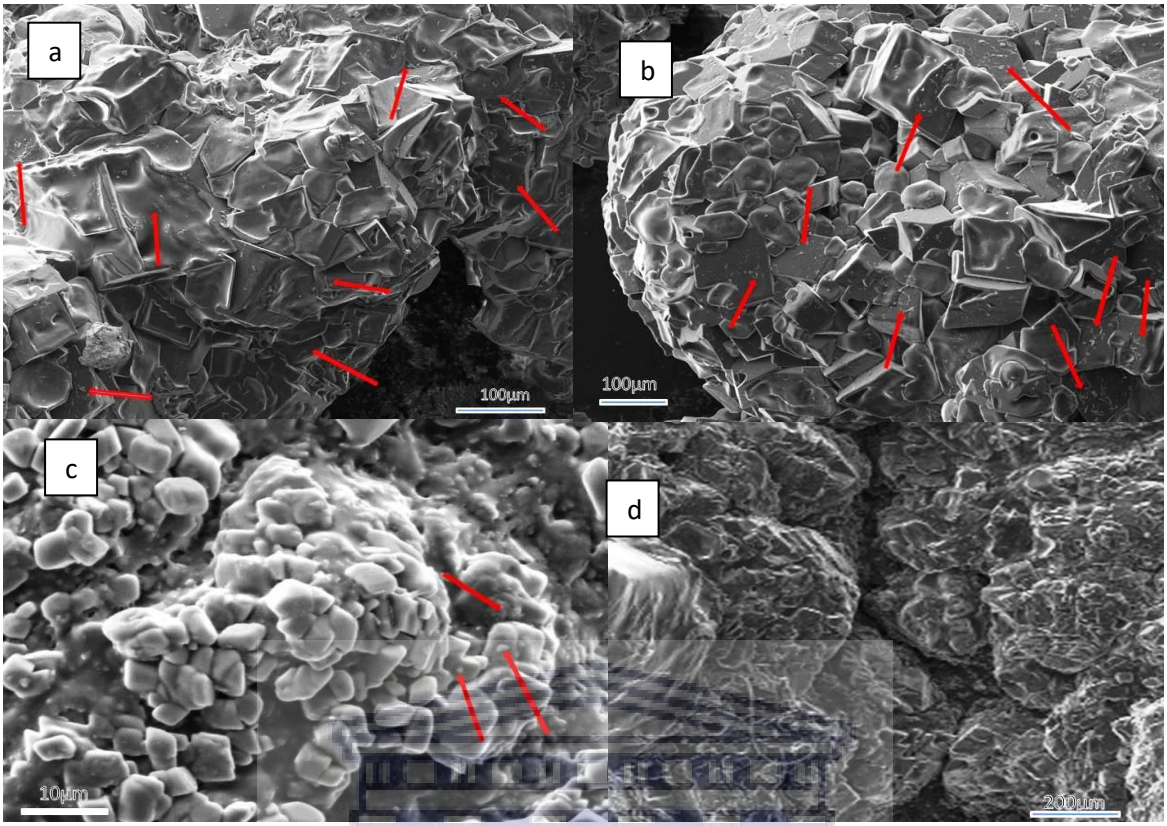

Figure 4.19: SEM images of binary salt (d), and nanosalt with different concentrations of AgNWs (i.e., binary salt + 1 wt% AgNWs (a), binary salt + 2 wt% AgNWs (b) and, binary salt + 3 wt% AgNWs(c))

b. Energy Dispersive X-ray spectroscopy

The chemical composition was determined by the energy-dispersive X-ray spectroscopy (EDS) instrument attached to the SEM.

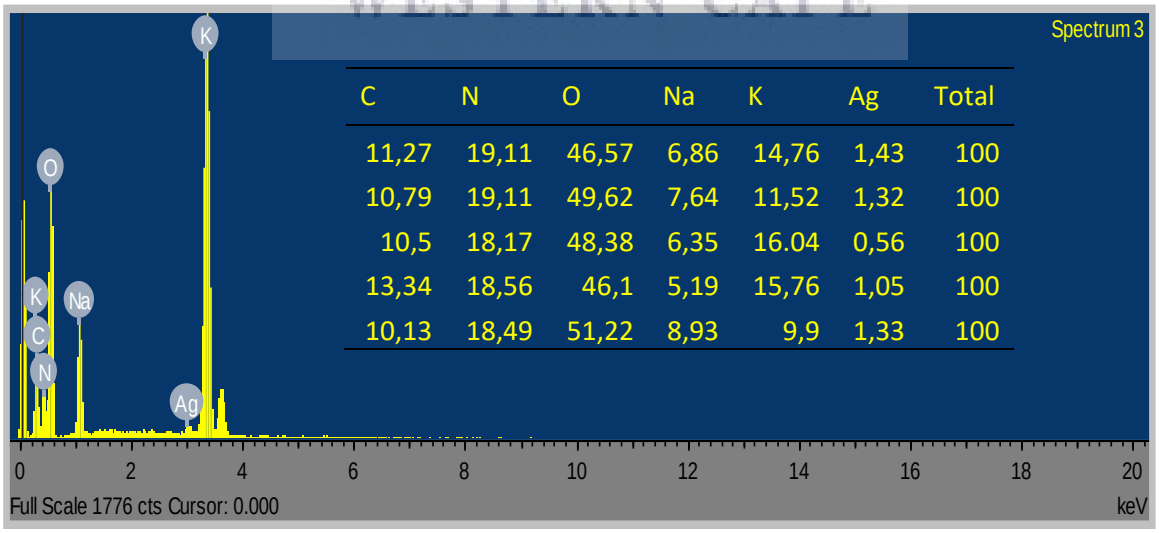

C	N	O	Na	K	Ag	Total
11,27	19,11	46,57	6,86	14,76	1,43	100
10,79	19,11	49,62	7,64	11,52	1,32	100
10,5	18,17	48,38	6,35	16.04	0,56	100
13,34	18,56	46,1	5,19	15,76	1,05	100
10,13	18,49	51,22	8,93	9,9	1,33	100

Figure 4.20: EDS Spectrum of binary salt with 1 wt% AgNWs, inset shows the chemical element with a respective weight percentage

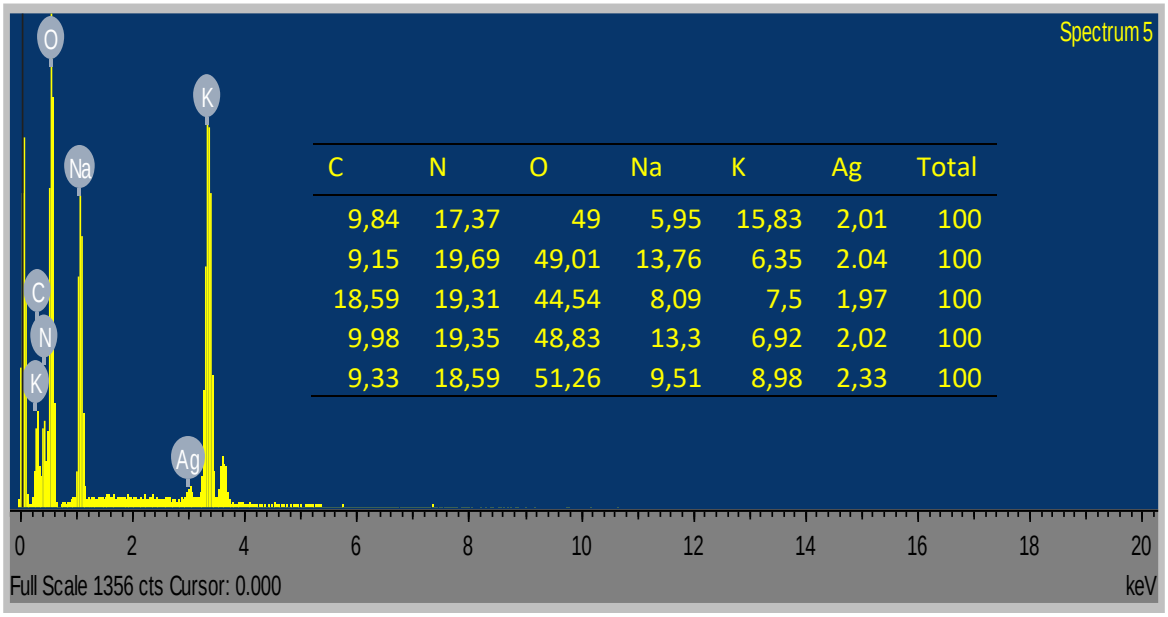

C	N	O	Na	K	Ag	Total
9,84	17,37	49	5,95	15,83	2,01	100
9,15	19,69	49,01	13,76	6,35	2.04	100
18,59	19,31	44,54	8,09	7,5	1,97	100
9,98	19,35	48,83	13,3	6,92	2,02	100
9,33	18,59	51,26	9,51	8,98	2,33	100

Figure 4.21: EDS Spectrum of binary salt with 2 wt% AgNWs, inset shows the chemical element with a respective weight percentage

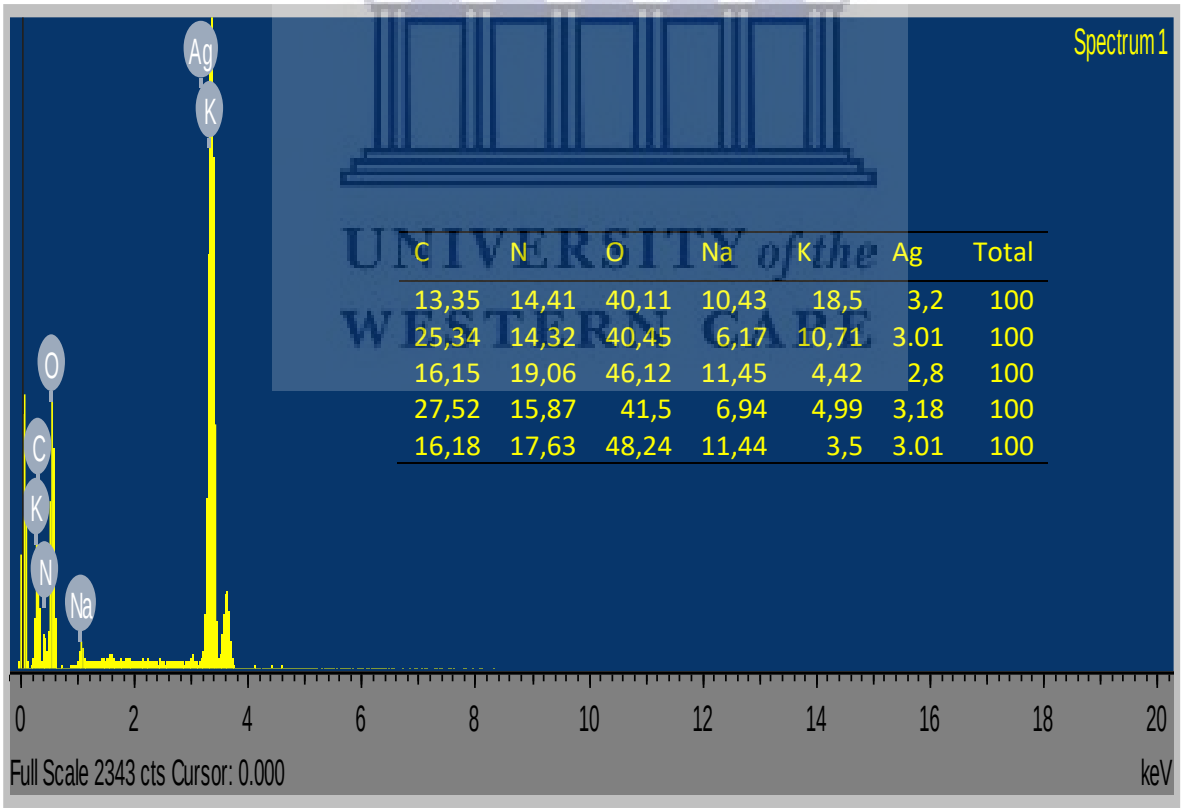

C	N	O	Na	K	Ag	Total
13,35	14,41	40,11	10,43	18,5	3,2	100
25,34	14,32	40,45	6,17	10,71	3.01	100
16,15	19,06	46,12	11,45	4,42	2,8	100
27,52	15,87	41,5	6,94	4,99	3,18	100
16,18	17,63	48,24	11,44	3,5	3.01	100

Figure 4.22: EDS Spectrum of binary salt with 3 wt% AgNWs, inset shows the chemical element with a respective weight percentage

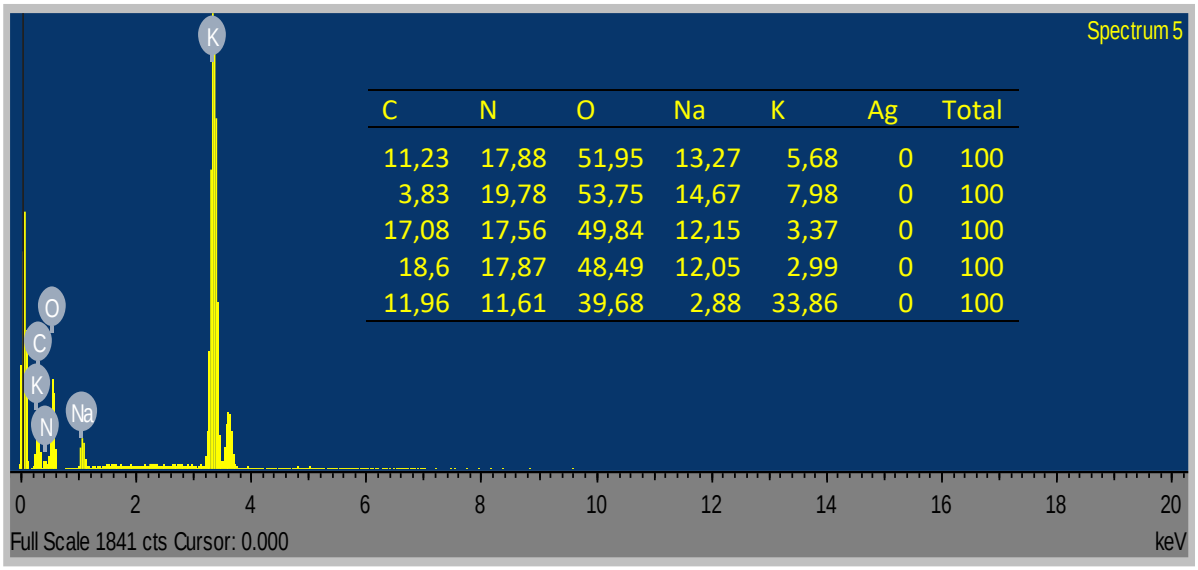

Figure 4.23: EDS Spectrum of binary salt, inset shows the chemical element with a respective weight percentage

It could be observed that no other element due to impurities was detected in the sample. The presence of Carbon came from the coating process. Element potassium has more intensity than sodium where 60% in mass weight of sodium nitrate was used against 40% in mass weight of potassium nitrate. This could explain using the two-step technique the mixture was not consistent or a large amount of sodium nitrate was lost during the evaporation process.

4.3.6 THERMAL CONDUCTIVITY (Temporal evolution of temperature)

Thermal conductivity is the capacity of a given material to transfer heat. Given two surfaces on each side of the material, the thermal conductivity is the conversion of heat energy per unit time per surface region, separated by the temperature difference. It is also, the rate at which heat passes through a specified material, expressed as the amount of heat that flows per unit time through a unit area with a temperature gradient of one degree per unit distance.

In the literature, different methods have been proposed and used for the thermal conductivity measurements this including Steady-state (Absolute technique; Comparative technique; Radial heat flow method; Parallel conductance method), Transient frequency-domain (Pulsed power technique), and Transient time-domain (Hot-wire method (needle-probe method); Laser flash method; Transient plane source (TPS) method) (Yüksel, 2016; Zhao *et al.*, 2016). A similar approach based on absolute technique was used. In the absolute technique, the heat source with known steady-state power input is used to heat the sample. The temperature

difference ΔT through a given distance (separation) of the sample is required by temperature sensors when a steady-state temperature distribution is established. Due to the large applications of thermocouples, they are often used as temperature sensors. The temperature difference should uncertainty should be less than 1%. Using Fourier's law of heat conduction, the thermal conductivity k of the material can be calculated by:

$$k = \frac{QL}{A\nabla T}$$

$$Q = p - Q_{loss}$$

Where Q is the amount of heat flowing through the sample, A is the cross-sectional area of the sample, L and ΔT are the distance and the temperature difference between temperature sensors, p is the applied heating power at the heat source side, and Q_{loss} is the parasitic heat losses due to radiation, conduction, and convection to the ambient. The main challenge in this technique is to control the heat flow, the heat loss, and the temperature difference (Zhao *et al.*, 2016).

In this work, only the temperature vs. time behaviour of the material was studied since using the technique above, the challenge was to determine the amount of heat accurately and the heat loss when the experiment was not conducted under vacuum. The rate of temperature increase was studied, in both samples (Binary salt and nanosalt with different percentages).

A certain amount of m=1.6g of nanosalt was weighted for different percentages, and a pelletizer was used to make different pellets in the cylindrical shape. The same technique was used for binary salt. A Manuel pellet press **(figure 4.24c)** was used and 15 Pa was applied to the nanosalt and binary salt to make pellets after 30 min each. Pellets of 13mm in diameter, 6mm in height were made **(figure 4.24a, b)**. A hot plate was used as a heat source, the thermocouple for the temperature monitoring through the entire experiment, and a chronometer to monitor the time **(figure 4.24d)**.

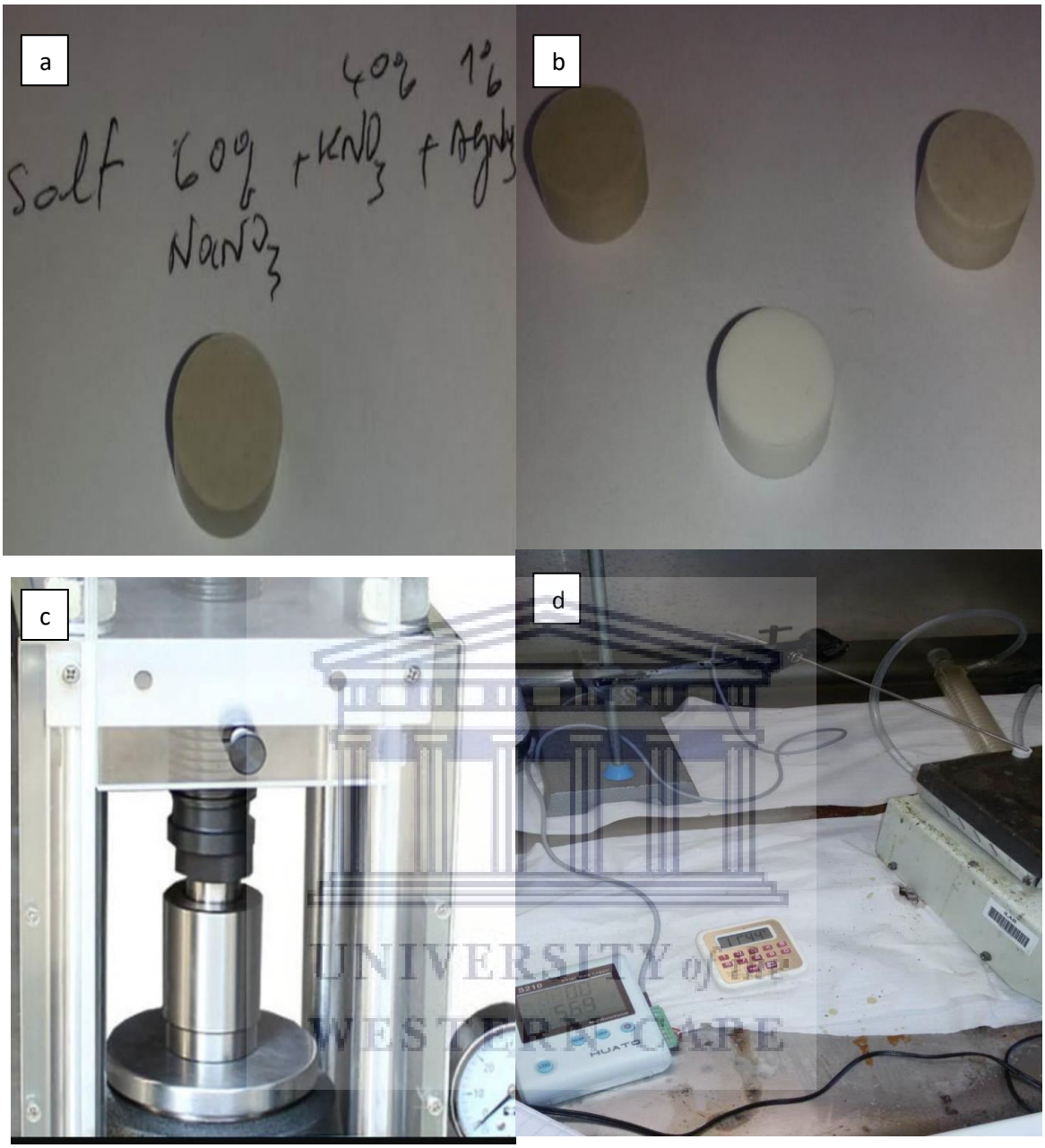

Figure 4.24: Shows pellets images of different nanosalt with different concentrations of AgNWs (i.e., binary salt + 1wt% AgNWs (a), binary salt + 2wt%AgNWs (b left) and, binary salt + 3wt%AgNWs (b right)), binary salt white pellet, A pellet press (c), and the experimental set (d).

In this experiment, the temperature's effect on the sample against time was studied. The sample was placed on a heating plate, which was previously heated at a fixed temperature of 67 ℃. The sample was taken at room temperature, the aim was to study how fast or slow the

sample conduct heat. For that, the temperature on the sample was expected to reach the equilibrium value of the hot plate fixed temperature.

Figure 4.24(d) shows the experiment setup where conditions were made that the temperature of the hot plate didn't influence the readings on the thermocouple

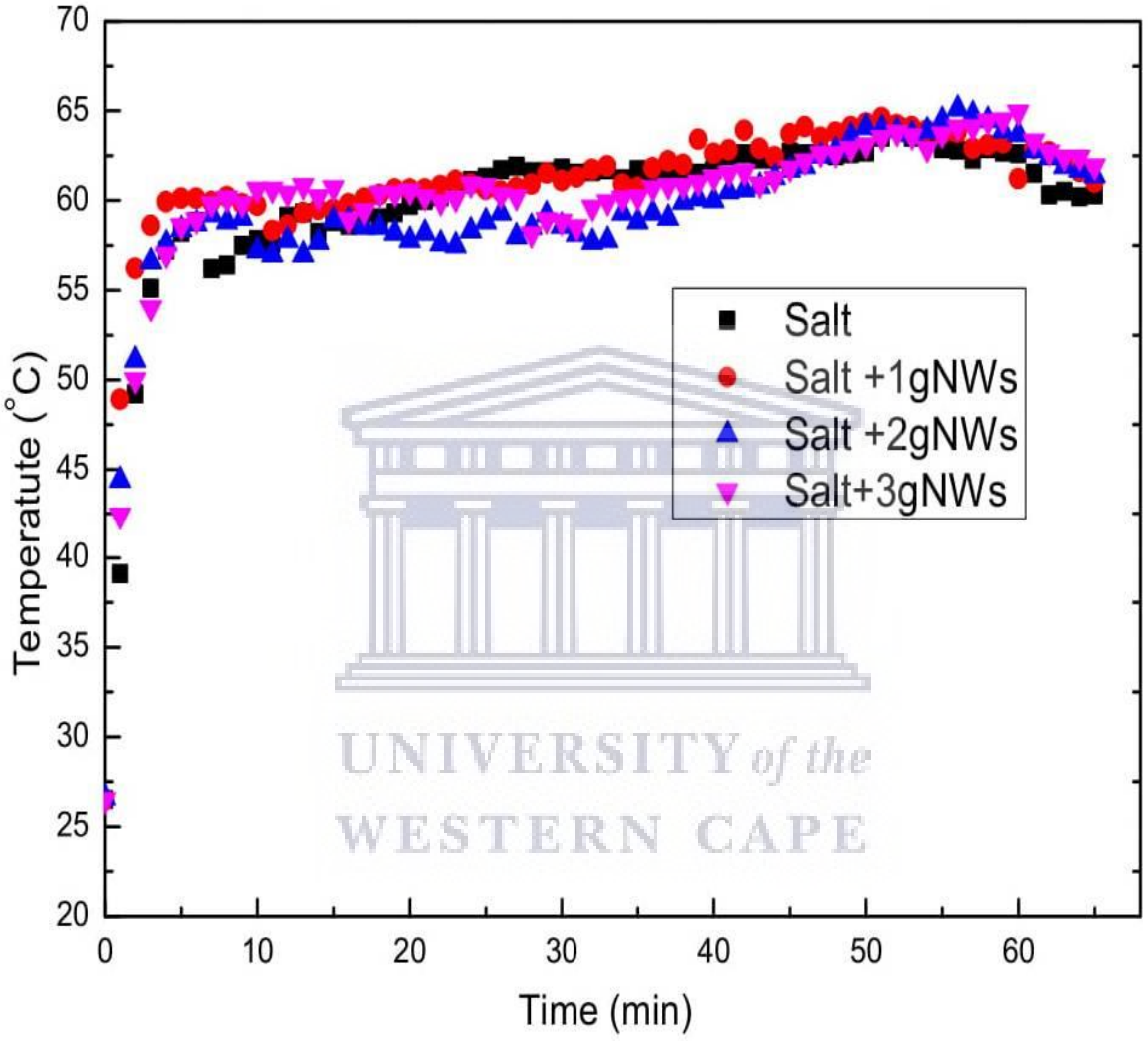

Figure 4.25: Temporal evolution of temperature for binary salt, and nanosalt with different percentages

Figure 4.25 shows the temporal evolution of temperature for solar salt and nanosalt with different percentages. It could be seen how faster or lower the heat was transferred from the hot plate to the samples. The temperature was recorded after every minute and, the experiment lasted about 65min for all the samples. To ensure a good reading of the temperature, the experiment was repeated two times and the average value was considered

and plotted. In the binary salt, the temperature on the sample was 26.5℃ and according to figure 4.25, the temperature was raised from 26.5 ℃ to 39 ℃ after 1 min and kept increasing until it was stable around 64 ℃ for 50min and started dropping after 55min suggesting that the equilibrium was reached. For nanosalt samples, it was observed that the increase from 26.5℃ was faster compared to the binary salt without any additives. Binary salt +1%wt AgNWs showed the increase from room temperature to 50 ℃ after 1 min and the same result could be observed for binary salt with 2%wt AgNWs and 3 %wt AgNWs additives where the temperature was raised respectively from 26.5 ℃ to 44 ℃ and 42 ℃ after 1 min. Figure 4.25 also shows that more time was needed for the binary salt to reach the equilibrium temperature where, binary salt with 1% wt AgNWs reached the equilibrium 45 min and, more the number of additives was increased, more time was required to the sample to reach the equilibrium but was faster compared to the binary salt without any additives suggesting, the use of silver nanowires (AgNWs) could increase the thermal conductivity of the nanosalt and also, binary salt with small amount of AgNWs not greater than 1% could increase effectively the thermal conductivity. The set temperature of 67 ℃ on the hot plate was not reached by the samples before it started dropping, this could be explained by the fact that the experiment was not conducted under vacuum conditions and, the temperature loss should be taken into account.

4.3.7 Conclusion

Binary salt and nanosalt were synthesized using the liquid solution method which showed that the use of a small amount of AgNWs in the binary salt could increase effectively the specific heat in both liquid and solid phase, the degradation time, and the behaviour of the material under certain conditions (i.e. temporal evolution of temperature) which suggested that the thermal conductivity could be increased by binary salt with addictives of silver nanowires. The use of silver nanowires in the binary salt has also explained the increase in the latent heat of fusion

SEM and EDS revealed respectively the morphology and the chemical composition of the samples. It could be observed that silver nanowires and nanoparticles were dispersed in the samples; the network formed by those particles could explain the increase of the specific heat. EDS revealed that the samples were pure and no other elements could be observed in the samples. The highest intensity of potassium which was supposed to be less could be

explained by the limitation of the liquid solution method or during evaporation, some amount of sodium was lost

4.2.8 References

Andreu-Cabedo, P. *et al.* (2014) 'Increment of specific heat capacity of solar salt with SiO 2 nanoparticles', *Nanoscale Research Letters*, 9(1), pp. 1–11. DOI: 10.1186/1556-276X-9-582.

Awad, A. *et al.* (2018) 'Latent and sensible energy storage enhancement of nano-nitrate molten salt', *Solar Energy*. Elsevier, 172(November 2017), pp. 191–197. DOI: 10.1016/j.solener.2018.04.012.

Chen, S. and Carroll, D. L. (2002) 'For Evaluation Only. Synthesis and Characterization of Truncated Triangular Silver Nanoplates', *Nano LETTERS*, 2(C), pp. 1003–1007.

Chieruzzi, M. *et al.* (2015) 'A New Phase Change Material Based on Potassium Nitrate with Silica and Alumina Nanoparticles for Thermal Energy Storage', *Nanoscale Research Letters*. Nanoscale Research Letters, 10(1). DOI: 10.1186/s11671-015-0984-2.

Chieruzzi, M. *et al.* (2017) 'Heat capacity of nanofluids for solar energy storage produced by dispersing oxide nanoparticles in nitrate salt mixture directly at a high temperature', *Solar Energy Materials and Solar Cells*. Elsevier B.V., 167(March), pp. 60–69. DOI: 10.1016/j.solmat.2017.04.011.

Coskun, S., Aksoy, B. and Unalan, H. E. (2011) 'Polyol Synthesis of Silver Nanowires : An Extensive Parametric Study', pp. 4963–4969.

Dudda, B. and Shin, D. (2013) 'Effect of nanoparticle dispersion on the specific heat capacity of a binary nitrate salt eutectic for concentrated solar power applications', *International Journal of Thermal Sciences*. Elsevier Masson SAS, 69, pp. 37–42. DOI: 10.1016/j.ijthermalsci.2013.02.003.

Hu, Y. *et al.* (2019) 'Enhanced heat capacity of binary nitrate eutectic salt-silica nanofluid for solar energy storage', *Solar Energy Materials, and Solar Cells*. Elsevier B.V., 192(December 2018), pp. 94–102. DOI: 10.1016/j.solmat.2018.12.019.

Kenisarin, M. M. (2010) 'High-temperature phase change materials for thermal energy storage', *Renewable and Sustainable Energy Reviews*, 14(3), pp. 955–970. DOI: 10.1016/j.rser.2009.11.011.

Khamliche, T. *et al.* (2018) 'Thermal conductivity enhancement of nano-silver particles dispersed ethylene glycol-based nanofluids', *Materials Research Express*. IOP Publishing,

5(3), p. 35020. DOI: 10.1088/2053-1591/aab27a.

Kottmann, J. *et al.* (2001) 'Plasmon resonances of silver nanowires with a nonregular cross-section', *Physical Review B - Condensed Matter and Materials Physics*, 64(23), pp. 2354021–23540210. DOI: 10.1103/physrevb.64.235402.

Lasfargues, M. (2014) 'Nitrate based High-Temperature Nano Heat Transfer Fluids: Formulation and Characterisation', p. 184.

Mao, H., Feng, J. and Ma, X. (2012) 'One-dimensional silver nanowires synthesized by self-seeding polyol process'. DOI: 10.1007/s11051-012-0887-4.

Mohamed, S. A. *et al.* (2017) 'A review on the current status and challenges of inorganic phase change materials for thermal energy storage systems', *Renewable and Sustainable Energy Reviews*, 70(December 2016), pp. 1072–1089. DOI: 10.1016/j.rser.2016.12.012.

Nazir, H. *et al.* (2019) 'Recent developments in phase change materials for energy storage applications: A review', *International Journal of Heat and Mass Transfer*. Elsevier Ltd, pp. 491–523. DOI: 10.1016/j.ijheatmasstransfer.2018.09.126.

Nekahi, A., Marashi, S. P. H. and Fatmesari, D. H. (2016) 'High yield polyol synthesis of round- and sharp-end silver nanowires with high aspect ratio', *Materials Chemistry and Physics*. Elsevier B.V, pp. 1–8. DOI: 10.1016/j.matchemphys.2016.09.033.

Tang, Y., He, W. and Wang, S. (2014) 'One-step synthesis of silver nanowires used in the preparation of conductive silver paste', (4), pp. 2929–2933. DOI: 10.1007/s10854-014-1961-8.

Xia, Y. *et al.* (2009) 'Shape-Controlled Synthesis of Metal Nanocrystals : Simple Chemistry Meets Complex Physics ? Angewandte', pp. 60–103. DOI: 10.1002/anie.200802248.

Yüksel, N. (2016) 'Methods and Techniques for Measuring the Thermal Conductivity of Insulation Materials', *Intech open science*, pp. 115–123.

Zhao, D. *et al.* (2016) 'Measurement techniques for thermal conductivity and interfacial thermal conductance of bulk and thin-film materials', *Journal of Electronic Packaging, Transactions of the ASME*, 138(4), pp. 1–64. DOI: 10.1115/1.4034605.

Zhu, J. *et al.* (2011) 'High-Yield Synthesis of Uniform Ag Nanowires with High Aspect Ratios by Introducing the Long-Chain PVP in an Improved Polyol Process', 2011. DOI:

10.1155/2011/982547.

CHAPTER FIVE

CONCLUSION AND FUTURE WORK

5.1. Conclusion

This master dissertation has aimed to investigate the physical properties enhancement of nanosalt including the melting point, the specific heat, the latent heat of fusion, and the thermal conductivity for concentrated solar power applications. The objective was firstly to synthesize silver nanowires (AgNWs), secondly to synthesize nanosalt (a mixture of binary salt and AgNWs at different weight percentages). The complementary analysis was finally conducted to investigate the morphology, chemical composition, crystalline structure, thermal properties, and as well as optical properties.

Silver nanowires were successfully synthesized using the polyol technique in which an inorganic salt (AgNo3) used as a precursor is reduced by a polyol (ethylene glycol) at an elevated temperature. SEM and TEM were used to investigate the morphology confirming that silver nanowires with different shapes and sizes have been synthesized. It could also be observed that time and temperatures played an important role in the aspect and growth of the silver nanoparticles or nanowires. Below a certain temperature, the high aspect ratio of Ag nanowires could not be possible. It was also noted that the temperature of 180℃ and time around 6hours were suitable parameters for silver nanowires growth using the polyol technique. Deficient and excess amounts of PVP over AgNO3 result in the formation of undesired Ag structures in addition to nanowires.

Nanosalt (a mixture of binary salt and AgNWs) were synthesized and, silver nanowires synthesized at 180℃ were used. The liquid solution method was used and sodium nitrate (NaNO3) and potassium nitrate (KNO3) were respectively mixed following a certain weight percentage of 60:40. The binary salt (molten salt) and nanosalt obtained were characterized and results were discussed. Binary salt and nanosalt were successfully characterized by SEM to investigate the morphology. It was found that AgNWs and nanoparticles were dispersed in the salt. The network or the surface area could explain the increase in thermal properties.

The discussed EDS, investigations reveal that no other peaks were detected and the binary salt and the nanosalt samples were a significant chemical purity and the samples were not contaminated during manipulations. Complementary analyses were conducted to investigate the thermal behaviour of the material. For that, dynamic scanning Calorimetry (DSC) was

conducted, the investigations revealed that the melting point of the binary salt and nanosalt was in perfect agreement with the literature, and also the latent heat of fusion agreed to the literature value. It was also noted the enhancement of latent heat of fusion for nanosalt. Further investigations revealed that the specific heat capacity of nanosalt was also enhanced both in solid and liquid phases suggesting that the surface area of the nanoparticles or nanowires could explain the increase. The degradation of the material was also investigated by using thermal gravimetric analysis (TGA) revealed that the dispersion of AgNWs in the binary salt didn't affect the sample and that degradation occurred after a suitable temperature.

The crystalline structure characterization binary salt and nanosalt by XRD found it to be stable after 3 thermal cycles, and this contributes to its high capacity of the material to be used at high-temperature many times without any degradation. The temporal evolution of temperature was finally investigated to predict the thermal conductivity outcome of the sample. It was observed that the increase of temperature in the nanosalt was faster than the binary salt suggesting that heat could be transferred rapidly explaining the thermal conductivity enhancement though this result was not conclusive but could give an insight into the thermal conductivity behaviour.

The obtained results represent an important step forward in defining the behaviour of nanosalt based silver nanowires and may prove of great interest in thermal energy storage. These results clearly show that s nanosalt based silver nanowires could be used to store a large amount of heat through the latent heat of fusion.

5.2 Future work

The focus of this master's dissertation was about the thermophysical properties enhancement of sodium nitrate and potassium nitrate for concentrated solar power applications. To prove the obtained finding during this project, solar salt-based silver nanowires should be implemented in the CSP. Though limitations were observed with the liquid solution method for the synthesis of nanosalt and binary salt because it could explain the high presence of potassium nitrate compared to sodium suggesting that the two materials were not mixed efficiently, the future work is to prepare the mixture of binary and the nanosalt using the step two method where the two salt and the additive particles will be melt simultaneously then solidified and grounded to ensure a good mixture of the final compound